CRITICAL REVIEW

The construction of dual-emissive ratiometric fluorescent probes based on fluorescent nanoparticles for the detection of metal ions and small molecules

Yaxin Li,[a,b] Hongzhi Lu[b] and Shoufang Xu ![ORCID] *[b]

With the rapid development of fluorescent nanoparticles (FNPs), such as CDs, QDs, and MOFs, the construction of FNP-based probes has played a key role in improving chemical sensors. Ratiometric fluorescent probes exhibit distinct advantages, such as resistance to environmental interference and achieving visualization. Thus, FNP-based dual-emission ratiometric fluorescent probes (DRFPs) have rapidly developed in the field of metal ion and small molecule detection in the past few years. In this review, firstly we introduce the fluorescence sensing mechanisms; then, we focus on the strategies for the fabrication of DRFPs, including hybrid FNPs, single FNPs with intrinsic dual emission and target-induced new emission, and DRFPs based on auxiliary nanoparticles. In the section on hybrid FNPs, methods to assemble two types of FNPs, such as chemical bonding, electrostatic interaction, core satellite or core−shell structures, coordination, and encapsulation, are introduced. In the section on single FNPs with intrinsic dual emission, methods for the design of dual-emission CDs, QDs, and MOFs are discussed. Regarding target-induced new emission, sensitization, coordination, hydrogen bonding, and chemical reaction induced new emissions are discussed. Furthermore, in the section on DRFPs based on auxiliary nanoparticles, auxiliary nanomaterials with the inner filter effect and enzyme mimicking activity are discussed. Finally, the existing challenges and an outlook on the future of DRFP are presented. We sincerely hope that this review will contribute to the quick understanding and exploration of DRFPs by researchers.

Introduction

Fluorescent probes have gained increasing attention for applications in chemical sensors owing to their high sensitivity, flexibility, and diversity; simplicity; and fast response times. Accordingly, fluorescent probes based on fluorescent organic dyes,[1,2] carbon dots (CDs),[3,4] quantum dots (QDs),[5,6] metal–organic frameworks (MOFs),[7,8] nanoscale graphitic carbon nitride (g-C_3N_4), and other materials,[9] have been widely applied for the detection of metal ions, organic pollutants, explosives, biomarkers, and others. In the early stage of their development, fluorescent probes were mainly designed based on the signal change in a single fluorescence channel, resulting in inaccurate sensing because several analyte independent factors, such as ambient microenvironment factors, including temperature, pH, and coexisting ions; photobleaching; and instrumental parameters, interfered with precise analysis.

Thus, to overcome these challenges, various ratiometric fluorescent probes (RFPs) have been developed.[10–15] Two or more emission bands are employed in the construction of RFPs and the ratiometric fluorescence intensities at different wavelengths are used for the quantification of a target. RFPs are more accurate than single-emission fluorescent probes owing to their self-calibration feature and high signal-to-background ratio. More importantly, rapid, simple, convenient, and cost-effective visual detection with a high precision can be realized based on RFPs with an obvious fluorescence color change under UV light. Depending on the number of emission peaks, RFPs can be classified into dual-emission RFPs (DRFPs) and multi-emission RFP (MRFPs). However, although MRFPs (mainly ternary-emission[16–22]) provide a wider color variation for accurate naked-eye determination, the development of MRFP lags behind that of other types of RFPs. This is because more factors need to be optimized, such as the interaction of three fluorescence signals and target sensitivity, and thus the construction of MRFPs is more complicated and time consuming. As a result, to date, DRFPs dominate the field of RFPs.

Generally, DRFPs can be classified into three types according to their target-responsive signal changing tendency, as

[a]School of Chemistry and Chemical Engineering, Linyi University, Linyi 276005, China

[b]Laboratory of Functional Polymers, School of Materials Science and Engineering, Linyi University, Linyi 276005, China. E-mail: shfxu1981@163.com
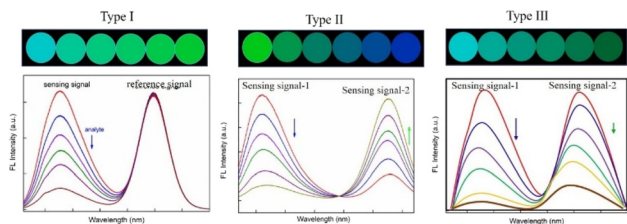
Fig. 1 The three types of DRFPs based on the signal change. Type I is reference DRFPs. Type II is DRFPs with two reversible signal changes and type III is DRFPs quenched with different sensitivities. Herein, it is assumed that the left and right emission bands correspond to blue and green fluorophores, respectively.

shown in Fig. 1. Type I is reference DRFPs. In this type, only one emission channel changes with the addition of the target, while the other remains stable as the reference. The reference is not only target insensitive, but also does not interact with the other fluorescence signal. Type II is DRFPs with two reversible signal changes, in which opposite signal variation tendencies in response to the target can be observed. FERT pairs and chemical-induced new emission can be used to construction this type of DRFP. Compared with the reference DRFP, this strategy displays a more vivid color change and possesses higher sensitivity. In type III DRFPs, the target quenches the two emissions simultaneously with different sensitivity. Considering the method sensitivity, reference DRFPs and DRFPs with two reversible signals changes are widely applied.

Fluorescence sensors can be constructed based on organic small molecules,[1,2] conjugated polymers[23] and fluorescence nanoparticles (FNPs).[3–9] Small fluorophores were the focus in the early development of fluorescence sensors due to their diverse chemical structures, facile molecular modification and varying detection mechanism and targets. However, they also exhibit some limitations such as complicated synthesis steps, easy photobleaching, and weak chemical stability. With the rapid development of FNPs, the construction of FNP-based fluorescence probes has played a key role in improving chemical sensors. Compared with conventional fluorescent dyes, FNPs exhibit many advantages when applied for fluorescence detection, as follows: (i) the optical property of FNPs can be easily adjusted by regulating their chemical composition or structure, size and shape, while traditional fluorescent dyes require complex synthesis process. (ii) FNPs can also be used as multivalent scaffolds for supramolecular assembly because of their high surface-area-to-volume ratio, providing a multifunctional platform for different sensing schemes. (iii) Many FNPs such as CDs display good biocompatibility and easier to achieve water dispersion, while fluorescence dyes self-aggregate in water, and generally lack biocompatibility. (iv) FNPs have the characteristics of wide absorption and narrow emission, and thus different signals can be detected simultaneously without mutual interference at the same excitation wavelength. (v) Many FNPs such as CDs, MOFs, and NCs display catalytic properties and fluorescence dual function, enabling the development of detection strategies through mul-

tiple mechanisms. Thus, FNPs have gained increasing popularity in the construction of fluorescence sensors. In the past decade, we witnessed significant progress in DRFPs based on FNPs for the accurate detection of metal ions, pesticides, antibiotics, pH, temperature or biomolecules in complex samples.

Meanwhile, numerous excellent reviews about DRFPs have been published, which focus on a specific group of target analytes or a particular class of fluorophores. For example, the progress made in organic small molecule-,[24,25] QD-,[26] CD-,[27] and MOF-[28,29] based DRFPs were summarized. Furthermore, some reviews were organized using the target as main line, and the construction methods for detecting ions,[24] small molecules, biomolecules, *etc.* were summarized separately.[13] However, the strategies for the construction of DRFPs have rarely been summarized. In 2018, Huang and co-workers summarized FNP-based DRFPs for targeting biomolecules.[30] In this work, five categories of FNP-based DRFPs were classified, including two-dye-embedded nanoparticles, nanoparticle–dye nanoconjugates, hybrid nanoparticles, single nanoparticles with intrinsic dual emission, and DNA nanostructures. However, some strategies for the construction DRFPs, such as DRFPs based on target-responsive FNPs and DRFPs based on auxiliary nanomaterials were not discussed, and DRFPs based on single nanoparticles with intrinsic dual emission were not comprehensively summarized. Considering the above-mentioned excellent review on DRFPs for biological macromolecules, this review mainly focuses on small molecules and metal ions. We systematically summarize the progress achieved in FNP-based DRFPs mainly in the past 5 years. Initially, this review introduces the commonly used fluorescence detection mechanism. Then, we focus on the design strategies of FNP-based DRFPs, which are classified into four categories, as follows: (A) hybrid FNPs, (B) single FNPs with intrinsic dual emission, (C) target-induced new emission and (D) DRFPs based on auxiliary nanomaterials, as displayed in Fig. 2. In the section on hybrid FNPs, the methods to assemble two types of FNPs, such as chemical bonds, electrostatic interaction, core satellite or core–shell structure, coordination, and encapsulation are introduced. In the section on single FNPs with intrinsic dual emission, the methods to design dual-emission CDs, QDs and MOFs are discussed. Subsequently, target-induced new emission, sensitization-, coordination-, hydrogen bonding-, and chemical reaction-induced new emission are highlighted. Also, in the section on DRFPs based on auxiliary nanoparticles, auxiliary nanomaterials with the inner filter effect and enzyme mimicking activity are discussed. In the last section, the existing challenges and future prospect of DRFP are discussed. We hope that this review can help researchers who are newcomers to the field of DRFPs quickly understand the current development status.

2. Fluorescence sensing mechanism

Regarding fluorescence sensors, their target responsive mechanisms mainly include fluorescence resonance energy transfer
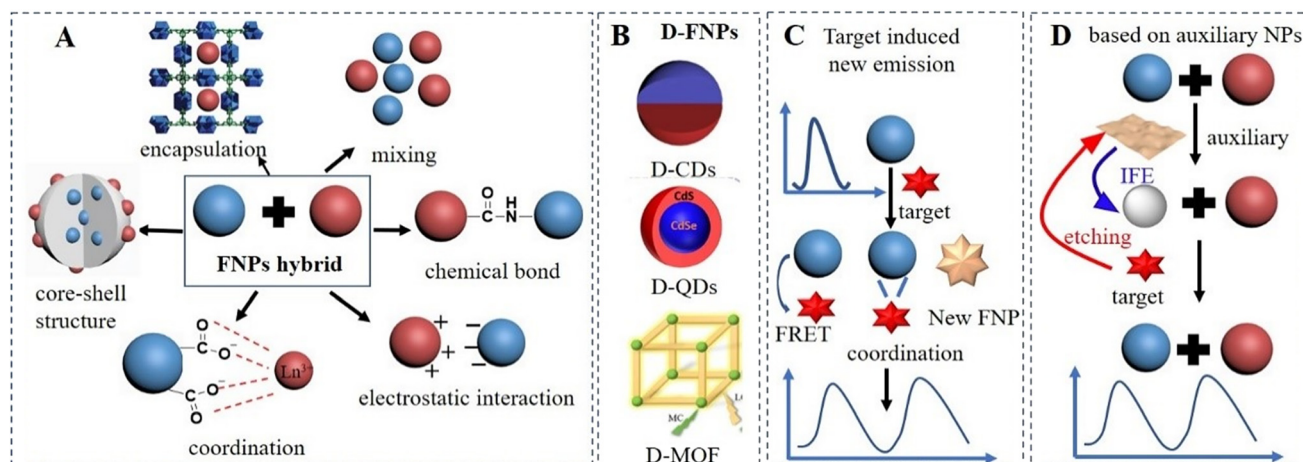
Fig. 2 Design strategies for DRFP. (A) Hybrid nanoparticles. (B) Single nanoparticles with intrinsic dual emission. (C) Single FNPs for target-induced new emission and (D) DRFPs based on non-fluorescence auxiliary nanomaterials.

(FRET), inner filter effect (IFE), photo-induced electron transfer (PET), intramolecular charge transfer (ICT), aggregation-caused quenching (ACQ), aggregation-induced emission (AIE), antenna effect (AE), excited-state intramolecular proton-transfer (ESIPT), twisted intramolecular charge transfer (TICT), and C=N isomerization, as displayed in Fig. 3. Given that these mechanisms have been introduced in some excellent reviews,[13,31,32] herein, we will

explain how to apply the above-mentioned principles to design DRFP based on specific literature.

2.1 FRET

FRET is a nonradiative process, whereby an excited-state donor (D) transfers energy to a proximal ground-state acceptor (A). The efficiency of FRET is highly dependent on the extent of
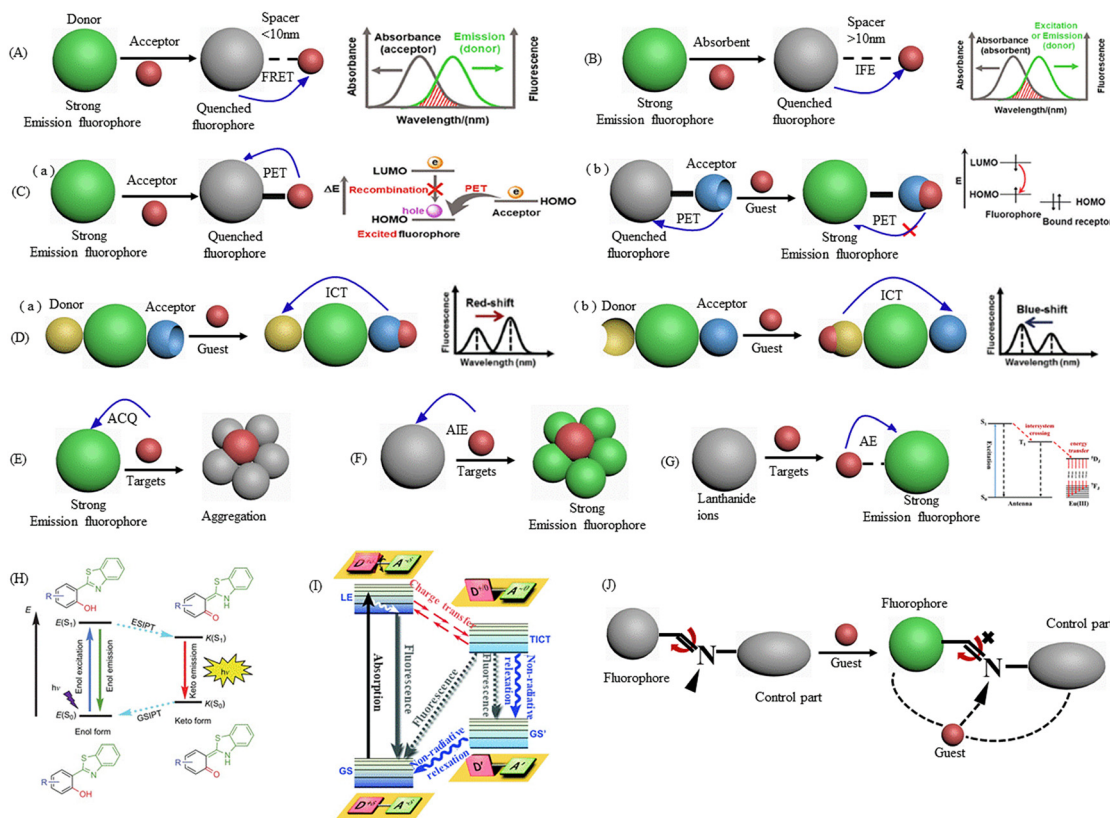

Fig. 3 A schematic diagram of different sensing mechanisms in the design of DRFPs. (A) FRET, (B) IFE, (C) PET, (D) ICT, (E) ACQ, (F) AIE, (G) AE, (H) ESIPT, (I) TICT, and (J) C=N isomerization.

spectral overlap and the distance between the D–A pair.[33,34] In FRET based DRFPs, the target can be the acceptor of the FRET pair. With the addition of the target, the original fluorescence intensity decreases, while a new emission appears. A good example of this was presented by Wang and co-workers, where they synthesized blue emission N,P and Cl-co-doped CDs (NPCl-CDs) for the detection of riboflavin, whose absorbance band well overlapped with the emission band of NPCl-CDs.[35] When riboflavin was added, the distance between NPCl-CDs and riboflavin of 1.01 nm satisfied the required distance (<10 nm) for the constructing of FRET systems, and thus a new emission peak at 530 nm originating from riboflavin appeared, while the emission of NPCl-CDs decreased.

Another strategy for the development of FRET-based DRFPs is using two types of FNPs that are FRET pairs. The target induces a change in the fluorescence intensity of one FNP separately. However, because of the FRET interactions between the two FNPs, the addition of the target induces a reversible variation in fluorescence intensity. For example, Liang's group constructed a CD-Au NC FRET pair for the detection of dopamine (DA), where CDs and Au NCs serve as the energy donor and acceptor, respectively.[36] With the addition of DA, the DA molecules adsorbed on the surface of Au NCs through electrostatic interaction. Then, the adsorbed DA was oxidized to o-quinone, which could accept electrons from the Au NCs, resulting in the quenching of the fluorescence of the Au NCs and the recovery of the blue fluorescence.

2.2 IFE

As a nonradiative energy conversion process, IFE also relies on the effective overlapping of the absorption spectrum with the fluorescence excitation or emission spectrum of FNPs. However, IFE does not require the distance between the quencher and FNPs to be within 10 nm. The process of FRET and IFE can be distinguished by measuring the lifetime of the FNPs. In the FRET process, the lifetime of the FNPs decreases, while it will not change in the process of IFE. In the construction of IFE-based DRFPs, the target can be metal ions or organic molecules with strong absorption band overlap with the excitation or emission band of FNPs. For example, Yue and co-workers mixed a blue emissive fluorescence Al-MOF with the fluorescence dye RhB for the detection of malachite green based on IFE. With the addition of malachite green, the fluorescence intensity of RhB at 575 nm was significantly quenched based on IFE, while the fluorescence of Al-MOF at 425 nm served as the reference signal.[37] Fe^{3+}, Cr^{6+}, VB1, picric acid, etc. with an absorption band in the visible light region can also be detected based on IFE by choosing the appropriate FNPs.

Another commonly used strategy for the construction of IFE-based DRFPs is the use of auxiliary nanoparticles, which can quench FNPs based on IFE. Ag NPs, Au NPs, and MnO_2 nanosheets are commonly employed as the quencher based on IFE. For example, Yang's team constructed a b-CD/Ag NP-rQD system for the detection of lactate.[38] Blue emission CDs (b-CDs) were prepared, and Ag NPs were grown on the surface of CDs via a one-pot method. The fluorescence of b-CDs was quenched by Ag NPs based on IFE. Then, b-CDs/Ag NPs was mixed with red emission QDs (rQDs) for the detection of lactate, which can be oxidized to produce H_2O_2. Ag NPs were etched by H_2O_2 to release b-CDs and Ag^+, resulting in the recovery of b-CDs and quenching of rQDs triggered by the free Ag^+.

The third strategy for the construction IFE-based DRFPs is the use of IFE pairs, such as a FRET pair. For example, the yellow fluorescence emission of 2,3-diaminophenazine (DAP) appears at around 450 nm in its excitation spectrum, which overlaps with the blue emission FNPs and can quench blue FNPs by the IFE process. Based on this mechanism, Cen's team constructed a sulfur quantum dot (SQD) and o-phenylenediamine (o-PD) binary system for the detection of uric acid (UA), which could be oxidized by uricase to generate H_2O_2.[39] Without UA, the system displayed bright blue emission from the SQDs. In the presence of UA, H_2O_2 was generated, which oxidized o-PD to produce DAP, and in turn SQDs were quenched by DAP based on the IFE process. By recording the fluorescence intensity ratio of QDs and DAP, UA was detected with high sensitivity.

2.3 PET and ICT

PET is a physical quenching process. In the absence of guest, an excited electron goes back to the highest occupied molecular orbital (HOMO) from the lowest unoccupied molecular orbital (LUMO) with fluorescence emission. However, if an orbital occupied by a lone pair of electrons has energy between the HOMO and LUMO of the fluorophore, one electron from this full orbital will transfer to the HOMO of the fluorophore, filling the vacancy that originally belongs to the excited electron. Thus, the pathway of the excited electron is blocked, and the fluorescence is quenched.[40] The specific orbital can come from the analyte. For example, Shen's group prepared N-acetyl-L-cysteine (NAC)-stabilized green emissive CdTe QDs for the detection of gatifloxacin by the PET process.[41] As shown in Fig. 4A, the HOMO energy of gatifloxacin (−5.838 eV) is between the LUMO (−4.968 eV) and HOMO (−7.098 eV) energy levels of CdTe QDs, an electron in the HOMO of gatifloxacin can transfer to the HOMO of CdTe QDs, and thus the excited electron of QDs in its LUMO cannot go back directly to its HOMO, resulting in the quenching of the green emissive QDs. Consequently, the excited electron of QDs go back to the ground state by transferred to the GFLX HUMO. Thus, with an increase in the concentration of GFLX, the green emission of QDs was quenched and a new blue emission appeared and was enhanced.

In ICT-based fluorescence sensors, the electron donor and electron acceptor are connected in a single fluorophore.[32] The donor can absorb photons and convert them into excited states, while the receptor can accept electrons from the donor and emit fluorescence. By regulating the distance and electron affinity between the receptor and donor, the fluorescence color and intensity can be adjusted. Upon the addition of an analyte, it can bind to the donor or acceptor regions and result
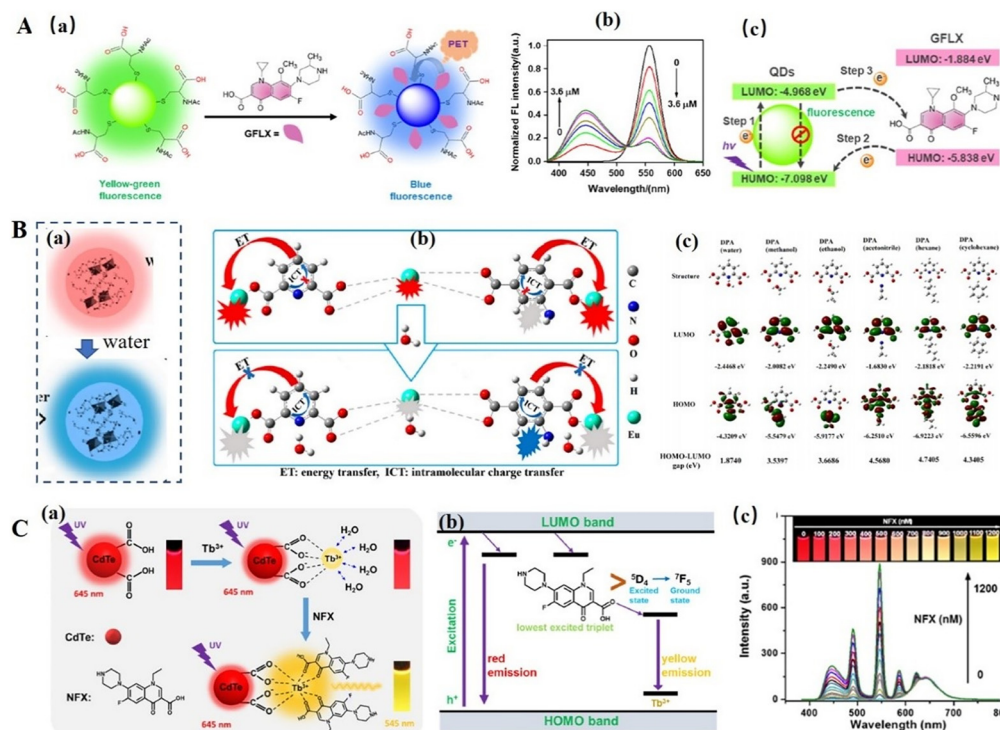
Fig. 4 (A) QD-based DRFPs for the detection of GFLX through the PET process. (a) The principle of the proposed ratiometric fluorescent strategy-based QDs for GFLX sensing. (b) The fluorescence emission spectra of the proposed QDs after incubation with varying concentrations of GFLX in PBS buffer at pH 7.4 for 5.0 min and (c) the PET mechanism of the DRFPs for GFLX sensing and imaging. (a–c) Reproduced with permission from ref. 41. Copyright 2020, the American Chemical Society. (B) The principle (a) and response mechanism of Eu-DPA/PTA-NH$_2$ detection of water based on ICT and (c) HOMO and LUMO images and HOMO−LUMO gaps of DPA in different solvents obtained using the Gaussian 09 program package. (a–c) Reproduced with permission from ref. 42. Copyright 2020, the American Chemical Society. (C) (a) An illustration of the synthesis of the Tb/CdTe QDs and the mechanism for the ratiometric fluorescence detection of NFX based on AE. (b) Schematic representation of the emission levels of Tb/CdTe QDs and the energy transfer from NFX to Tb^{3+}. (c) The fluorescence spectra of the ratiometric probe solution upon exposure to different concentrations of NFX. The inset shows the corresponding fluorescence color photos under 365 nm UV irradiation. (a–c) Reproduced with permission from ref. 49. Copyright 2020, the American Chemical Society.

in an alteration in the dipole strength of the donor–acceptor species, resulting in intensity changes and spectral shifts. The interaction between the analyte with the acceptor end resulted in a red-shift, while the interaction of the analyte with the donor resulted in a blue-shift. Compared with the PET mechanism, the ICT process induces clear fluorescence band shifts, while PET quenching does not result in spectral shifts. For example, Xiao's team prepared Eu-dipicolinic acid/2-aminophthalic acid (Eu-DPA/PTA-NH$_2$) for a water sensor based on the water-induced characteristic ICT.[42] As shown in Fig. 4B, Eu-DPA/PTA-NH$_2$ displayed blue emission at 443 nm from the PTA-NH$_2$ ligand and red emission at 620 nm from Eu^{3+}. An increase in the content of water induced an increase in blue emission and decrease in red emission. The ligand-water HOMO–LUMO gaps were much lower than that of the ligand-organic solvents, which was beneficial for the water-induced ICT between two ligands of DPA and PTA-NH$_2$. Also, the ICT process partly quenched the red fluorescence of Eu^{3+}. Meanwhile, organic solvents cannot induce ICT in the two ligands because of the high band gaps of ligands-organic solvents.

2.4 ACQ and AIE

ACQ is a common fluorescence quenching phenomenon. The bright emission is largely weakened or even quenched by target-induced aggregation. For instance, Jiang's group mixed b-CDs with red Au NCs for the detection of glyphosate, in which the fluorescence of b-CDs was quenched within 2 s after introducing glyphosate *via* ACQ, while the Au NCs served as the reference, leading to an obvious color change from blue to pink to orange.[43]

Fluorides with AIE properties exhibit weak fluorescence in their molecular state but become strongly emissive in the aggregate state, which overturned our traditional understanding of the ACQ effect. In 2001, Tang *et al.* first discovered the phenomenon of AIE[44] and explained the mechanism of AIE.[45] The AIE property displayed the advantages of low background, good photostability, and high quantum yield.[46,47] Some FNPs, such as Au NCs, Cu NCs and CDs display AIE phenomena and are used to construct DRFPs. For example, Jiang's group mixed glutathione-stabilized gold nanoclusters (GSH-Au NCs) with ethylenediamine-functionalized graphene oxide (EDA-GO) for

the detection of Cd^{2+} by the AIE process.[48] Firstly, Cu^{2+} was introduced to quench the weak orange emission of GSH-Au NCs. Then, the addition of Cd^{2+} induced the aggregation of Cu^{2+}-GSH-Au NCs and lit up the yellow fluorescence of GSH-Au NCs. During the detection process, EDA-GO was insensitive to Cd^{2+} as the reference. A change in fluorescence color from blue to red with an increase in the content of Cd^{2+} could be observed.

2.5 AE

AE was mainly used to enhance the luminescence of the lanthanide ion. Lanthanide ions are photo-responsive metal ions with excellent luminescence performance. However, the fluorescence of lanthanide ions is difficult to be directly excited because of their forbidden f–f transitions. In the presence of some organic molecules, such as tetracyclines (TCs), the light absorbed by the organic molecules can be transferred to lanthanide ions and turn on their fluorescence. AE was used to prepare lanthanide ions based on fluorescent MOFs or detection of TCs. For example, Yang' group chelated Tb^{3+} on the surface of CdTe QDs for the detection of norfloxacin.[49] As shown in Fig. 4C, the fluorescence of CdTe QDs at 645 nm remained almost unchanged after doping with Tb^{3+} and the addition of norfloxacin. With the addition of norfloxacin, a Schiff base complex was formed between NFX and Tb^{3+}, and the π–π energy transferred from NFX to Tb^{3+}, lighting up the yellow emission of Tb^{3+}. A remarkable color variation from red to yellow could be observed with an increase in the concentration of norfloxacin.

2.6 ESIPT, TICT, and C=N isomerization

ESIPT represents a photo-cyclic process comprised of four distinct stages (E → E* → K* → K), as shown in Fig. 3H. When light energizes the electron in its enol configuration (E), it transitions to the excited enol state (E*). In close proximity within the molecule, there are proton donors (–OH or –NH$_2$) and proton acceptors (C=N or C=O), leading to the formation of an excited ketone structure (K*). Subsequently, following radiation decay back to the electronic ground state, reverse proton transfer occurs, resulting in the restoration of the initial E structure. The majority of ESIPT chromophores manifest dual emission *via* a four-level optical cycle involving a short-wavelength emission stemming from the excited enol state (E*) and long-wavelength emission arising from the excited ketone configuration (K*).[50] In recent years, numerous AIE probes exhibiting the ESIPT characteristics have also been extensively documented. These probes offer noteworthy benefits, including a considerable Stokes shift exceeding 150 nm, minimized levels of autofluorescence and self-absorption, heightened ketone emission and substantial spectral sensitivity when aggregated.[51]

TICT is an electron transfer process involving molecules composed of an electron donor D and acceptor A. As shown in Fig. 3I, the excited singlet state generated by light absorption is called the local excitation state (LES). The two parts are mutually planar, and the solvent relaxation around the mole-

cule causes the planes of D and A to rotate simultaneously until the distortion is about 90°. The conjugation between the two parts disappears, resulting in the TICT excited state. This emission characteristic may be related to the environment, which makes the TICT-based fluorescent group an ideal sensor for solvents, micro viscosity and chemicals.[52] The performance of dual-emission fluorescent probes has been optimized by combining TICT with AIE mechanisms.[53]

C=N isomerization is a signal transduction mechanism, which is a non-radiative decay process of the excited state in the compound, and thus it is non-fluorescent. This non-radiative process can be suppressed by the response to the target, thus providing a method for designing fluorescent sensing molecules, as shown in Fig. 3J.[54]

ESIPT, TICT and C=N isomerization always involve organic dye molecules, and thus in this work, we will not provide a detailed description.

2.7 Static quenching and dynamic quenching

Fluorescence quenching can be divided into dynamic quenching and static quenching. Dynamic quenching is caused by collisions between quenchers and excited state of fluorescent molecules, while static quenching is caused by the formation of non-luminescent complexes between quenchers and fluorescent molecules in the ground state. The quenching process can be described using the Stern Volmer equation, and dynamic quenching and static quenching can be distinguished by the quenching constant. In the case of dynamic quenching, higher temperatures lead to faster diffusion and more collision chances, and thus the quenching constant increases with an increase in temperature. In the case of static quenching, an increase in temperature may cause a decrease in the stability of the composite, and thus as the temperature increases, the quenching constant continuously decreases.[55]

Table 1 summarizes this detection mechanism, which shows its conditions and the variation of fluorescence. FRET, IFE, PET, ICT, ACQ, AIE and AE are the commonly used FNP-based detection mechanism, and there are many types of FNPs with wide spectra and diverse functional groups. Thus, it is crucial to design FNPs based on the target and detection mechanism. In the design of FNPs, the functional groups on their surface and fluorescence emission spectrum are two important factors. Different detection mechanisms have different requirements for FNPs. In the case of FNPs employing FRET and IFE, their fluorescence spectrum is the primary factor. The fluorescence spectrum of QDs, CDs, MOFs, *etc.*, ranging from the blue, yellow, green, and red to near infrared region can be controlled by adjusting the reaction time, raw materials, and ligands during their preparation. In the case of FNPs employing PET and ICT, their function groups are crucial. Functional groups can achieve specific recognition of the target substance, enable electron and energy transfer, and regulate the energy levels. In the case of FNPs employing AE, the presence of lanthanide ions is crucial. Therefore, in the process of designing MOF materials and FNP composites, lanthanide ions should be introduced. ACQ is a commonly

Table 1 A summary of the different fluorescence detection mechanisms

Mechanism	Conditions	Fluorescence signal change
FRET	1. Spectral overlap of D–A pairs 2. The distance of D–A pairs is <10 nm	Donor decreases, while acceptor increases or appearance of a new peak.
IFE	Effective overlap between spectra	Fluorescence quenching
PET	1. Absorbs photons that match the electron energy 2. The electrons in the target orbit must have an unoccupied hole	Fluorescence quenching
ICT	1. Different polar components 2. Appropriate spacing and conformation 3. Has a certain conjugate structure	Red-shift or blue-shift
ACQ	1. The molecule is in the aggregation state 2. The molecule should have a large π-conjugated structure or stacking space	Fluorescence quenching
AIE	1. The molecule is in the aggregation state 2. The molecule has a π-conjugated structure	Fluorescence intensity enhanced.
AE	1. Fluorescent systems require antenna-shaped metal nanostructures 2. The effective connection and interaction between the fluorescent group and the antenna structure	Fluorescence intensity enhanced
ESIPT	1. There are tautomers of ketones and alcohols in the molecular structure 2. The molecule should have an appropriate electronic structure that can absorb light and excite it to the excited state	1. Fluorescence intensity enhanced 2. Red shift in emission peak
TICT	1. Molecules should have a certain flexibility and undergo structural distortion in the excited state 2. Maintain a certain conformational stability	1. Large Stokes shifts 2. Red shift of emission peak 3. Fluorescence quenching
C=N isomerization	1. There is at least one C=N bond or similar bond in the molecule 2. The structure of a molecule should have a certain variability, enabling its atoms or groups to move, rotate or rearrange	Fluorescence intensity enhanced
Static quenching	1. There is a sufficiently close interaction distance between the fluorescent substance and the quencher 2. There is an interaction between FNPs and the quencher	Fluorescence quenching
Dynamic quenching	1. The quencher molecule must be able to interact effectively with the excited-state energy level of the fluorescent substance 2. Appropriate molecular proximity and sufficient collision strength	Fluorescence quenching

observed fluorescence quenching phenomenon existing in most FNPs. Thus, it is important to design FNPs with specific functional groups, which can specifically recognize the target substance and cause aggregation of FNPs. AIE is a fluorescence enhancement phenomenon mainly occurring in NCs such as Au NCs, Ag NCs and Cu NCs. Thus, it is important to design NCs with specific functional groups, which can specifically recognize the target substance and cause aggregation of FNPs. There is no single FNP with the best performance, which mainly depends on its specific final application. Regarding specific targets, different FNPs should be equally considered.

3. Strategies for construction of DRFPs

The commonly used strategy to construct DRFPs is employing two fluorophores with well-resolved emission. In this strategy, the FNPs can be assembled by physical mixing, chemical bonds, electrostatic interactions, coordination interactions, encapsulation, or formation of core satellite or core–shell structure, as shown in Fig. 2A. With the development of dual-emissive FNPs, an increasing number of sensors have been constructed using FNPs with intrinsic dual emission, including dual-emission CDs (D-CDs), D-MOF, D-QDs, and dual-emission nanohybrid (DNH), as displayed in Fig. 2B. DRFPs

can also be constructed based on a single FNP. The addition of the target induces the appearance of a new fluorescence peak, which may originate from the target-induced FRET or target-induced chemical reaction, as shown in Fig. 2C. In the above-mentioned three construction strategies, the target directly interacts with the FNPs, causing changes in their wavelength or intensity. DRFPs can also be constructed based on non-fluorescence auxiliary nanoparticles, such as Au NPs, Ag NPs, and MnO_2 nanosheets, as displayed in Fig. 2D. The target directly interacts with the non-fluorescent auxiliary nanoparticles, such as etching, reduction and aggregation, causing changes in the absorption spectrum and catalytic performance of auxiliary nanoparticles. This further causes a change in the fluorescence intensity of FNPs. In this review, the strategies for the construction of DRFPs are classified into four categories, as follows: (i) assembly of two FNPs, (ii) single FNPs with intrinsic dual emission, (iii) target-induced active FNP and (iv) FNPs with auxiliary non-fluorescent nanoparticles.

3.1 Assembly of two FNPs

The commonly used strategy to construct FNP-based DRFPs is employing two types of FNPs with well-resolved emission. In this strategy, the FNPs, such as CDs, QDs, MOFs, and Au NCs, can be assembled with another FNP, dyes, or lanthanide ions. In the case of MOF-based DRFPs, dyes and FNPs can also be encapsulated into the pores of MOFs.

3.1.1 Mixing two types of FNPs. The simplest way to construct DRFPs is directly mixing two types of FNPs in solution, avoiding complex chemical modifications. When one FNP acts as the reference and the other as the reporter, reference DRPFs can be constructed. For example, Wang and co-workers constructed a DRFP for the detection of Pb^{2+} by simply mixing b-CDs and r-CDs (Fig. 5A). B-CDs prepared using sodium citrate and polyacrylamide as precursors possessed many carboxyl groups on the surface of b-CDs. With the addition of Pb^{2+}, a new absorption peak appeared due to the carboxyl group chelated with Pb^{2+} to form b-CD/Pb^{2+} complexes, which quenched the b-CDs based on IFE. Meanwhile, the r-CDs prepared with *p*-PDA as the precursor was inert to Pb^{2+} and used as the reference. A paper strip based on this mechanism was prepared for semiquantitative visual detection.[56] A similar reference DRFP was constructed by mixing two types of FNPs, such as green CDs (g-CDs) mixed with r-CDs for the detection of ClO^-, in which g-CDs acted as the reference;[57] b-CDs were mixed with dark-red emission $CuInS_2$/ZnS QDs for the detection of chlortetracycline, while QDs acted as the reference;[58] b-CDs mixed with orange emission $AgInS_2$ QDs for the detection of ibandronic acid, while b-CDs acted as the reference;[59] blue emission Ln-MOFs (Eu-PTA, PTA as terephthalic acid) were mixed with red emission Ln-MOF Eu-DPA(DPA: dipicolinic acid) for the detection of H_2O_2, while Eu-DPA acted as the reference;[60] b-CDs were mixed with red CuNCs for the detection of thiram, in which b-CDs acted as the reference;[61] and

b-CDs were mixed with the red-emitting fluorescent dye 1-aminoanthraquinone for the detection of histamine, in which the dye acted as the reference.[62]

In some cases, the reference FNPs require necessary surface modification before mixing to maintain their stability. For example, Xue and co-workers mixed red-emission Au NCs and green-emission QDs for the detection of Cu^{2+}, in which Au NCs acted as the response signal and QDs as the reference.[63] To eliminate the interference of ions on the QDs, the QDs were coated with SiO_2. Sometimes the response signal was modified before mixing with the reference to protect the response signal or achieve phase transfer. For example, Fan and co-workers mixed orange-emitting $CsPbBr_{1.5}I_{1.5}$@MSNs with water-stable green-emitting $CsPbBr_3$ nanosheets for the detection of the moisture content in oil, as shown in Fig. 5B.[64] After the addition of trace water, the fluorescence intensity of $CsPbBr_{1.5}I_{1.5}$@MSNs at 595 nm decreased rapidly, while the $CsPbBr_3$ nanosheets maintained a good fluorescence intensity. MSNs could protect the oil-soluble $CsPbBr_{1.5}I_{1.5}$ QDs from water damage, while maintaining their fluorescence response property. Liu's research group mixed g-CDs with red-emitting ZnCdSe/ZnS QDs for the detection of Hg^{2+}, in which g-CDs served as the internal standard, while QDs acted as the response signal.[65] To help the hydrophobic QDs to transfer to aqueous solution, amphiphilic polyurethane (PU) was prepared and used to encapsulate the hydrophobic ZnCdSe/ZnS QD *via* the emulsion self-assembly. Thus, this as-prepared
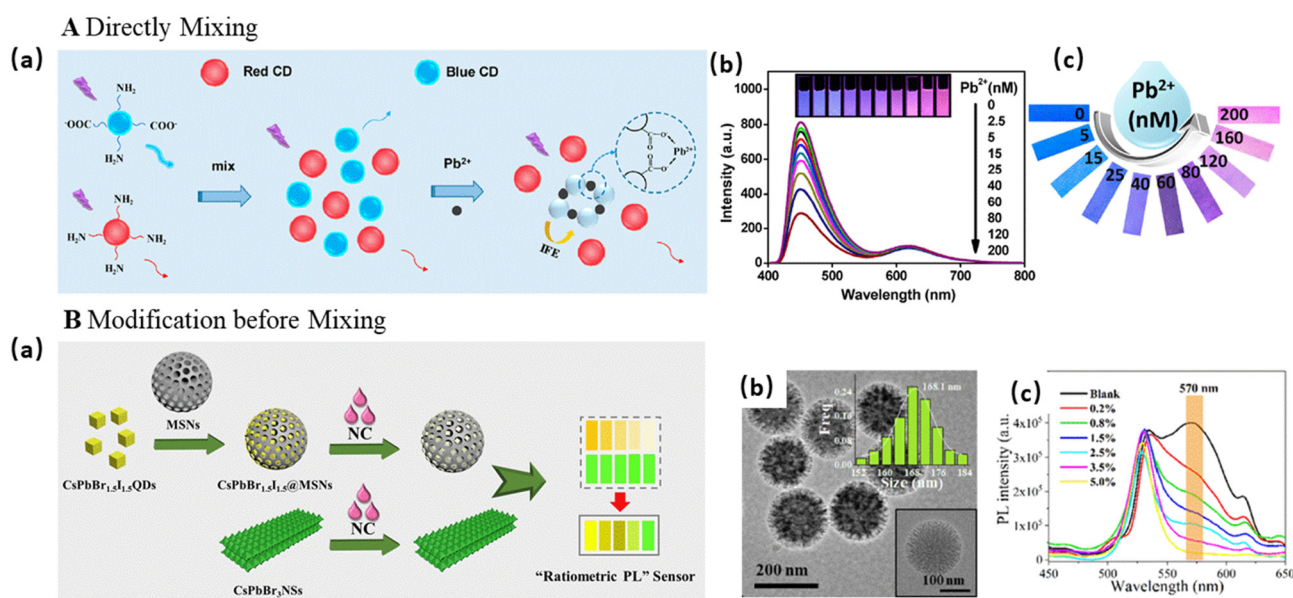

Fig. 5 DRFPs constructed by physical mixing of two types of FNPs. (A) Directly mixing two types of FNPs. (a) A schematic illustration of the design of a DRFP by mixing r-CDs with b-CDs for the detection of Pb^{2+}. (b) The fluorescence spectra of the DRFP with the addition of Pb^{2+}. The inset shows the corresponding fluorescent photos under a 365 nm UV lamp. (c) The visualization detection of Pb^{2+} using colorimetric fluorescent printing paper prepared using printing fluorescent ink on a piece of filter paper. The photos were taken under a 365 nm UV lamp. (a–c) Reproduced with permission from ref. 56. Copyright 2019, the American Chemical Society. (B) The modification of FNPs before mixing. (a) A schematic Illustration of perovskite nanomaterial-engineered multiplex-mode fluorescence sensing of moisture content in edible oil. (b) The TEM image of $CsPbBr_{1.5}I_{1.5}$@MSNs. (c) The fluorescence spectra of $CsPbBr_3$ NSs and $CsPbBr_{1.5}I_{1.5}$@MSNs after reacting with edible oil with different moisture contents. (a–c) Reproduced with permission from ref. 64. Copyright 2021, the American Chemical Society.

hydrophilic QD@PU probe could be selectively quenched by Hg^{2+} in aqueous solution.

By mixing two types of FNPs, DRFP with two reversible signal changes also can be constructed when the two FNPs are also responsive to the target or interactions exist between the two FNPs. For example, Zhao's group mixed yellow-CDs (y-CDs) with blue Cu NCs for the detection of Cu^{2+}. The formation of Cu^{2+}-(y-CDs) complexes could enhance the fluorescence of y-CDs by inhibiting PET, and also quench the Cu NCs by the FRET process. However, the chelation of y-CDs with Cu^{2+} could be inhibited by bioethics, and thus this sensor can be used for the detection of bioethics.[66] Another example is that a red Zr-MOF using tetraphenylporphyrin tetrasulfonic acid hydrate (TPPS) as the ligand was mixed with green fluorescein isothiocyanate (FITC) for the detection of Cu^{2+}. After the addition of Cu^{2+}, Cu^{2+}-TPPS was formed and the charge transfer between Cu^{2+} and TPPS resulted in the quenching of Zr-MOF at 667 nm. Electron transfer occurs from the donor Zr-MOF to the acceptor FITC after the addition of Cu^{2+}, which enhanced the FL of FITC at 515 nm.[67]

The target can also induce the quenching of two mixed FNPs with different sensitivity.[68–70] For instance, Shi's group[69] mixed blue emission MoS_2 QDs with CdTe QDs for the detection of TCs. With the addition of TCs, both the emission of the MoS_2 QDs and CdTe QDs was quenched by PET, while the fluorescence of CdTe QDs was quenched more obvious than MoS_2 QDs. For this type of DRFPs, to make the color change more sensitive, the concentration of the lower sensitive FNP must obviously be higher than the higher sensitive FNP.

Based on the fluorescence on–off-on mode, DRFPs can be designed for the multifunctional detection of two targets successively.[71–73] For example, Fe-MIL-88 with blue emission at 427 nm was mixed with Au NCs with red emission at 643 nm to detect Hg^{2+} and thiram.[70] The binding of Hg^{2+} with thiol groups on the surface of Au NCs caused the quenching of the Au NCs. However, with the further addition of thiram, thiram competed with Au NCs for binding with Hg^{2+} due to the high affinity of "Hg–S", which resulted in an enhancement in the red fluorescence of Au NCs. During the whole detection process, the fluorescence of Fe-MIL-88 remained stable as the reference.

3.1.2 Hybrid two-FNPs by covalent bonds. The construction of DRFPs by physical mixing is simple. However, DRFPs with two independent sensing units may lead to errors because of some analyte-independent interferences, such as nonspecific binding, uneven distribution, and variations in the surrounding microenvironment. Therefore, DRFPs are mostly constructed by hybrid FNP complexes to efficiently eliminate irrelevant factors. Combining two fluorescent materials through chemical bonds is essential for the majority of traditional DRFPs.

Coupling of $–NH_2$ and $–COOH$ with the help of 1-ethyl-3-(3-dimethylaminopropyl) carbodiimide (EDC) and N-hydroxysuccinimide (NHS) are usually used to construct DRFPs. FNPs can be chemically bonded with FNPs,[74–78] dyes,[79–83] and fluorescence proteins[84] to construct DRFPs. For

example, b-CDs and GSH-modified red CdTe QDs were conjugated by covalent bonds between NH_2 and COOH for the detection of NO_2, as shown in Fig. 6A.[74] In the presence of NO_2, the red emission of GSH-QDs was specifically quenched, which is ascribed to surface sulfur oxidation, while b-CDs remained stable as the reference, resulting in a distinguishable color change from orange-red to blue. In addition to directly chemically bonding two FNPs, FNPs can form a hybrid on the surface of SiO_2 NPs for improving their stability, biocompatibility and decreasing the cytotoxicity toward cells tremendously. Han's group constructed a hybrid DRFP by covalently bonding CdTe/CdS QDs with b-CDs using SiO_2 NPs as a support for the detection of Cu^{2+},[78] as shown in Fig. 6B. Firstly, red-emissive CdTe/CdS QDs were capped around SiO_2 NPs by covalent bonds, and then the b-CDs were further covalently attached to the surface of QDs. The Cu^{2+} could quench the QDs effectively based on PET but did not cause a change in the fluorescence strength of the CDs.

EDC and NHS are usually used to prepare protein–FNP bioconjugates by coupling the $–NH_2$ in proteins and $–COOH$ in FNPs. For example, a phycocyanin-CD nanoprobe was constructed via an amination reaction through EDC/NHS for the ratio fluorescence determination of $ONOO^-$. In the presence of $ONOO^-$, the CDs with blue emission were remarkably quenched because the amino groups on the surface of CDs were oxidized by $ONOO^-$, while the fluorescence intensity of phycocyanin at 645 nm changed a little as the reference.[84] However, the bioconjugation of FNPs with protein by coupling the $–NH_2$ in proteins and $–COOH$ in FNPs may result in uncontrollable aggregation and a loss of the QY. Alternatively, click chemistry, as a site-specific combinatorial chemistry method, can be employed to construct chemical-bonded DRFPs. For example, He's group[85] synthesized clickable $N_3–$CdZnTeS QDs using N-acetyl-L-cysteine and mercaptosuccinic acid as the reductant and capping agent, respectively, as shown in Fig. 6C. Then, a 5(6)-carboxyfluorescein@glucose oxidase-QD (FAM@GOx–QD) complex was constructed via 1,3-dipolar cycloaddition between $N_3–$CdZnTeS QDs and dibenzocyclooctynes/5(6)-carboxyfluorescein-glucose oxidase (DBCO/FAM-GOx). When the FAM@GOx–QD complex was incubated with glucose, H_2O_2 was produced by enzymatic oxidation. Then, H_2O_2 oxidized CdZnTeS QDs and quenched the CdZnTeS QDs. In the detection process, the green fluorescence of FAM was invariable as the reference. Click reaction effectively avoided cross-linking and aggregation.

3.1.3 Hybrid two-FNPs by electrostatic interaction. The intrinsic properties of FNPs can be affected during the activation steps and chemical bond process. Thus, to eliminate this effect, the self-assembly of FNPs has attracted significant attention due to its simplicity and speediness. Due to the high density of $–COOH$ groups and their ionization, the surface of these materials is negatively charged in a wide pH range. When they meet positive NH_2-modified FNPs[86–88] and dyes,[89,90] DRFPs can be constructed via facile electrostatic self-assembly. For example, amino-modified Si NPs and GSH-Au NCs could self-assemble into spherical particles due to electro-

A. Covalent bond between NH₂ and COOH
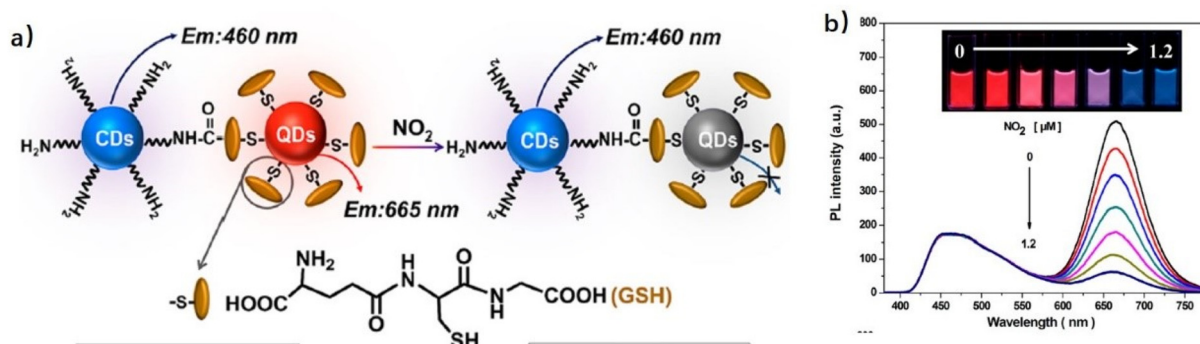
B Covalent bond QDs with CDs on the surface of SiO₂
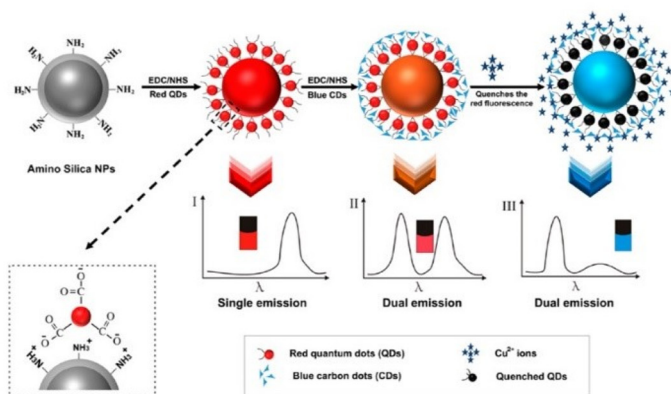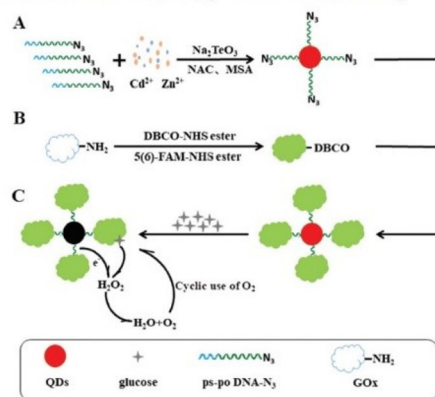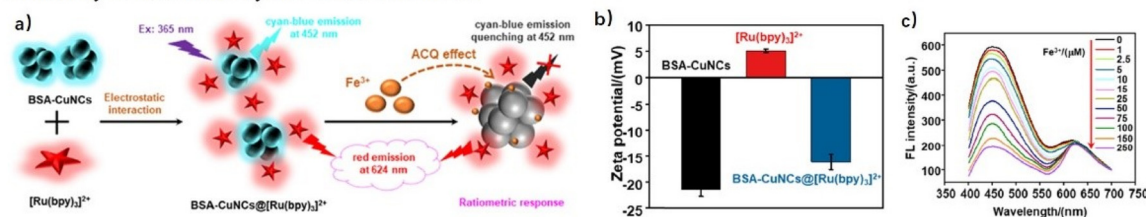
C. Covalent bond by click chemistry

Fig. 6 (A) A schematic illustration of the covalent bonding of b-CDs with r-QDs for the detection of NO₂ (a) and fluorescence spectra of a DRFP upon exposure to NO₂ (b). The concentrations of nitrogen dioxide from top to bottom are 0, 0.2, 0.4, 0.6, 0.8, 1.0, and 1.2 μM. The insets show the corresponding fluorescence photos of the probe solution taken under a 365 nm UV lamp. (a and b) Reproduced with permission from ref. 74. Copyright 2015, the American Chemical Society. (B) A schematic illustration of the covalent bonding of b-CDs and r-QDs on the surface of SiO₂ for the detection of Cu^{2+}. Reproduced with permission from ref. 78. Copyright 2016, the American Chemical Society. (C) A schematic illustration of the fabrication of the FAM@GOx−QD complex by click chemistry and its application for the detection of glucose. Reproduced with permission from ref. 85. Copyright 2022, the Royal Society of Chemistry.

static interaction. Consequently, the fluorescence of GSH-Au NCs at 570 nm was enhanced due to AIE, while the Si NPs retained their own blue fluorescence at 450 nm. In the presence of protamine, the cationic protamine absorbed on the surface of GSH-Au NCs and quenched GSH-Au NCs. Based on the fact that protamine can be hydrolyzed by trypsin, the SiNP@GSH-AuNC system could be employed to detect protamine and trypsin successively based on the on–off-on mode.[88]
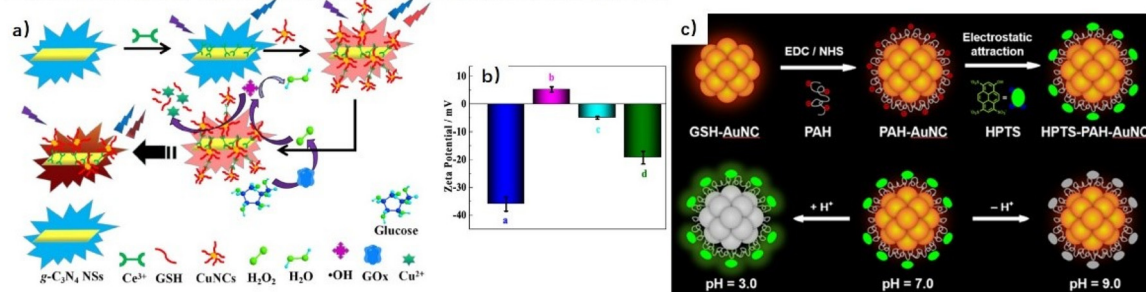
The positively charged fluorophore $[Ru(bpy)_3]^{2+}$ is commonly introduced in DRFP systems as the reference by electrostatic interaction.[91–93] For example, negative cyan-blue fluorescent BSA-Cu NCs bind with the positive $[Ru(bpy)_3]^{2+}$ by electrostatic interaction, resulting in an increase in the zeta potential of BSA-Cu NCs from −21.36 mV to −16.10 mV, yielding a dual-emission assembly of BSA-Cu NCs@$[Ru(bpy)_3]^{2+}$. As shown in Fig. 7A, in the presence of Fe^{3+}, Fe^{3+} chelated on the surface of BSA-Cu NCs and quenched BSA-Cu NCs by the Fe^{3+}-triggered ACQ effect. During the detection process, the emission from $[Ru(bpy)_3]^{2+}$ at 624 nm remained almost unchanged as the reference.[92]

Two FNPs with the same charge can be self-assembled by electrostatic interaction through an intermediate auxiliary. For example, Wang and co-workers conjugated g-C₃N₄ NSs with Cu NCs by electrostatic and coordination interactions with the help of Ce^{3+} for the detection of H_2O_2.[94] As shown in Fig. 7B, g-C₃N₄ NSs, Ce^{3+}, and Cu NCs were mixed to form a g-C₃N₄ NS-Ce^{3+}-Cu NC complex. The zeta potential changed from −35 mV to +5 mV, and then to −5 mV when g-C₃N₄ NSs were combined with Ce^{3+}, and then combined with negatively charged Cu NCs, indicating that the complex of g-C₃N₄ NSs-Ce^{3+}-Cu NCs was formed by strongly electrostatic interactions. Upon the addition of H_2O_2, the emission of Cu NCs at 625 nm was dramatically quenched because of the oxidation of Cu^0 or Cu^+ in Cu NCs to Cu^{2+}, whereas the 460 nm emission of g-C₃N₄ NSs remained stable. Similarly, Wang et al. employed Au^{3+} as a linking bridge to assemble g-C₃N₄ NSs with Ag NCs for the detection of biothiols.[95] After the formation of the g-C₃N₄ NS-Au^{3+}-GSH-Ag NC complex, the fluorescence of g-C₃N₄ NSs was quenched due to electron transfer caused by the grafting of Au^{3+} and the fluorescence of Ag NCs was
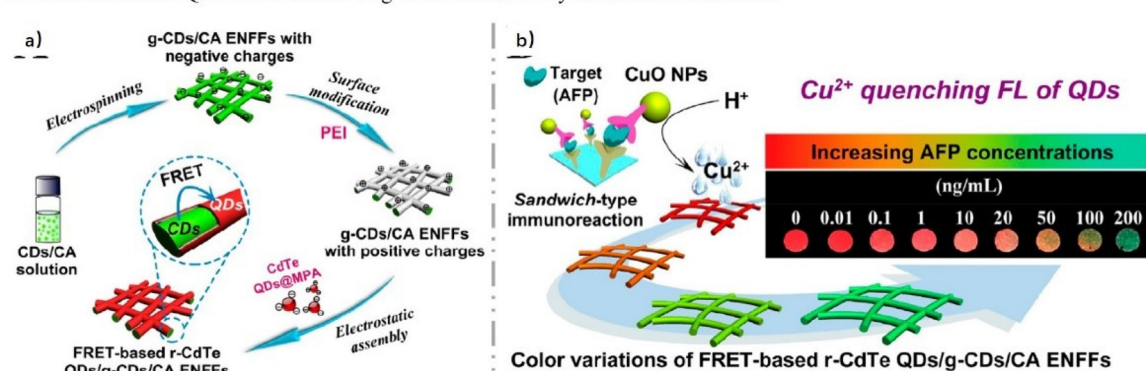
Fig. 7 (A) Construction of DRFP by directly assembling BSA–Cu NCs and [Ru(bpy)$_3$]$^{2+}$ by electrostatic interaction for Fe^{3+} detection. Reproduced with permission from ref. 92. Copyright 2022, Elsevier. (B) The construction of DRFP by the assembly of g-C$_3$N$_4$ NSs and Cu NCs by electrostatic interaction through an intermediate Ce^{3+} auxiliary for the detection of H$_2$O$_2$. Reproduced with permission from ref. 94. Copyright 2022, Elsevier. (C) The construction of DRFP *via* the assembly of QDs on the surface of g-CD/CA ENFFs by electrostatic interaction and application of Cu^{2+}-mediated immunoassay for biomarkers. Reproduced with permission from ref. 97. Copyright 2018, the American Chemical Society.

enhanced due to AIE. In the presence of biothiols, the g-C$_3$N$_4$ NS-Au^{3+}-GSH-Ag NC complex collapsed because of the stronger coordination between Au^{3+} and the sulfhydryl of biothiols, which resulted in the recovery of the fluorescence of g-C$_3$N$_4$ NSs and weakened that of Ag NCs. The change in the emission intensity ratio of g-C$_3$N$_4$ NSs to Ag NCs could be used for the detection of biothiols with high accuracy.

Electrostatic interaction assembly is also an effective way to construct solid-phase-sensing films by modified FNPs on the surface of a solid substrate by facile electrostatic attraction.[96,97] For example, Huang and co-workers prepared dual-emitting r-CdTe QD/g-CD cellulose acetate (CA) solid electrospun nanofibrous films by doping and surface-assembling two-step strategy,[97] as shown in Fig. 7C. Firstly, the g-CDs were directly doped in CA NFs during the electrospinning process. Secondly, g-CDs/CA NFs were modified with the positively charged polymer PEI, and then negatively charged r-CdTe QDs

were decorated on the surface of the g-CDs/CA NFs by electrostatic interaction. Because of the FRET process between g-CDs and r-QDs and the strong quenching response of Cu^{2+} to QDs, the fluorescence of r-QDs was quenched, while that the g-CDs recovered with the addition to Cu^{2+}. Meanwhile, the fluorescence color changed could be clearly distinguished from red, orange, and yellow to green. Furthermore, based on a sandwich-type immunoassay in which CuO NPs were labeled on antibody, this fiber sensor also was used for the detection of a biomarker. Under acidic conditions, numerous Cu^{2+} ions were released from CuO NPs and produced signal amplification. Using this sandwich-type immunoassay, the detection target can be expanded by changing the specific antibody.

3.1.4 Core satellite or core–shell structured nanohybrid. Core-satellite nanostructures can effectively separate target-sensitive and reference fluorophores, making it an effective way to construct reference DRFPs, in which reference FNPs are

embedded in core particles, while the response signal is coated on the surface of the core by covalent bonds or electrostatic interactions. SiO_2 NPs with the advantages of easy preparation, stability, and optical transparency are the commonly used core.[98–103] Core-satellite-structured dye@SiO_2@CDs for the detection of Cu^{2+},[99] CDs@SiO_2@CdTe QDs for the detection of H_2O_2-related chemical reactions,[100] r-CdTe QDs@SiO_2@g-CdTe QDs for the detection of aspirin,[101] CDs@SiO_2/AuNCs for the detection of Cu^{2+},[102] and CDs@SiO_2@AuNCs for the detection of Ag^+ (ref. 103) have been reported. In addition to SiO_2 nanoparticles, polystyrene (PS) also was employed to embed the reference signal. For example, Yi's group encapsulated red-emissive CdSe/ZnS QDs in PS NPs and covalently conjugated b-CDs for the detection of Fe^{3+}, AA, ALP and 2,4-D by successive chemical reactions.[104] Compared with SiO_2 NPs, are PS NPs were less used, which may be because of their relatively higher price and difficult control.

3.1.5 FNPs coordinated with lanthanide ions. Lanthanide ions have received extensive attention in the field of fluorescence sensors because of their advantages of large Stokes shift, sharp emission spectrum, long fluorescence lifetime, chemical stability and low background. Lanthanide ions are easy to coordinate with carboxyl group-functionalized FNPs to form DRFPs for the detection of sensitizers of lanthanides ions, such as tetracycline (TC) and dipicolinic acid (DPA). For example, Pu's group prepared CDs@Eu^{3+} by coordinated carboxyl group-functionalized b-CD with Eu^{3+} ions for the detection of TCs, which could replace water molecules to combine with Eu^{3+}, leading to the luminescence enhancement of the Eu^{3+} ions by AE, as shown in Fig. 8A.[105] Meanwhile, the b-CDs were quenched by TC based on IFE, realizing the accurate detection of TC in complex samples with excellent selectivity and high sensitivity.

Pu's group coordinated Eu^{3+} with fluorescence MOFs of UiO-66-$(COOH)_2$-NH_2 for the detection of DPA.[106] UiO-66-$(COOH)_2$-NH_2 was prepared using Zr^{4+} as the metal node and 1,2,4,5-benzenetetracarboxylic acid (H_4BTC) and 2-aminoterephthalic acid (NH_2-BDC) as ligands, which displayed bright-blue emission originating from the NH_2-BDC ligand. By virtue of their abundant carboxyl groups, UiO-66-$(COOH)_2$-NH_2 coordinated with Eu^{3+} to form UiO-66-$(COOH)_2$-NH_2/Eu^{3+}. Upon the addition of DPA molecules, the red fluorescence from the sensitized Eu^{3+} increased based on AE, while the blue fluorescence at 453 nm was greatly quenched through IFE. Similar complexes such as Ti_3C_2 QDs@Eu^{3+} for the detection of TC,[107] CDs@Eu^{3+} for the detection of TC,[108,109] CuNCs@Eu^{3+} for the detection of TC,[110] MoS_2 QDs@Eu^{3+} for the detection of TC,[111] g-C_3N_4/Eu^{3+} for the detection of DPA[112] and TC,[113] HNT@CDs@Eu^{3+} for the detection of DPA,[114] LML-Eu^{3+}-GMP coordination polymer for the detection of TC,[115] and MOF@COF@Tb^{3+} for the detection of norfloxacin[116] have been reported. However, among the family of TCs, including CTC, TC, OTC and DC, the specific detection of each one is rather challenging due to their highly structural similarity.

In addition to detecting sensitizers based on the fluorescence-on mode, the coordinated lanthanides ions can be pre-sensitized and detected target based on the turn-off mode[117] or as a reference.[118] As shown in Fig. 8B, Xiong's group coordinated Eu^{3+} with 4,6′-dihydroxy-1,3,5′-triazine-2-carboxylic acid (TCA) and N-doped CDs to form a europium complex of Eu-TCA/NCDs for the detection of chloramphenicol (CAP).[117] Eu-TCA/NCDs exhibited bright-blue fluorescence emission from CDs at 445 nm and red fluorescence emission from sensitized Eu^{3+} at 617 nm. The addition of CAP resulted in significant fluorescence quenching of the blue and red emission peaks. The quenching of NCD by CAP was based on IFE. The fluorescence quenching of Eu^{3+} was from the inhibition of AE. The hydrogen bond between CAP and Eu-TCA/NCDs caused the excited electron to transfer from Eu-TCA-NCDs to CAP and reduce the structural compactness for AE. Saha's group coordinated Tb^{3+} with b-CDs for the detection of Hg^{2+} using Tb^{3+} as the reference.[118] b-CDs were prepared using citric acid and phenylenediamine as the carbon precursor, and then Tb^{3+} was coordinated on the surface of b-CDs. In the detection of Hg^{2+}, the b-CDs were quenched due to the coordination of Hg^{2+} with $-NH_2$, $-CONH_2$ and pyridinic nitrogen on the surface of CDs with high affinity, while the green emission of Tb^{3+} remained stable as the reference.

In addition to coordinating lanthanides ions with FNPs to construct DRFPs, DRFPs can also be formed by target-induced coordination of two types of FNPs. For example, Zhang's group assembled b-CDs with r-CDs by target Cu^{2+}-induced coordination.[119] As shown in Fig. 8C, the residual p-phenylenediamine at the surface of r-CDs efficiently bind Cu^{2+} ions, which could further bind b-CDs with abundant carboxyl group through coordination interactions. Meanwhile, the coordination of r-CDs with Cu^{2+} produce a strong visible absorption at around 480 nm that overlaps well with the emission spectrum of b-CDs, resulting in the quenching of b-CDs, whereas the fluorescence intensity of r-CDs was unaffected.

3.1.6 Fluorescence guest encapsulated in MOFs. Generally, MOFs are constructed from bridging organic linkers and metal ions or clusters by coordination bonds. Diverse organic linkers and various metal ions endow MOFs with diverse properties.[120] The luminescence of luminescent MOFs (LMOFs) originates from their metal ions, organic ligands, or guest molecules in the MOF framework, as shown in Fig. 9A. The luminescence of metal ions is mainly centred on the lanthanide ions, and the commonly used fluorescence ligands are displayed in Fig. 9C. DRFPs based on LMOFs can be constructed using LMOFs with intrinsic dual emission encapsulating a fluorescence guest in LMOFs, encapsulating two types of fluorescence guests in non-fluorescence MOFs, or modifying fluorescence dyes or FNPs on the surface of LMOFs, as shown in Fig. 9B. In this part, we mainly discuss the fluorescence guest encapsulated in MOFs.

Fluorescence guests such as dyes, CDs, and QDs can be encapsulated in the MOF framework via "in situ growth" or "in situ encapsulation" method, as displayed as Fig. 10. In the "in situ growth" method, the MOF is first prepared, and then the FNPs are grown in the pores of the MOF. In the "in situ encapsulation" method, FNPs or dyes are initially prepared

A. CDs coordinated with Eu³⁺ for detection of TC
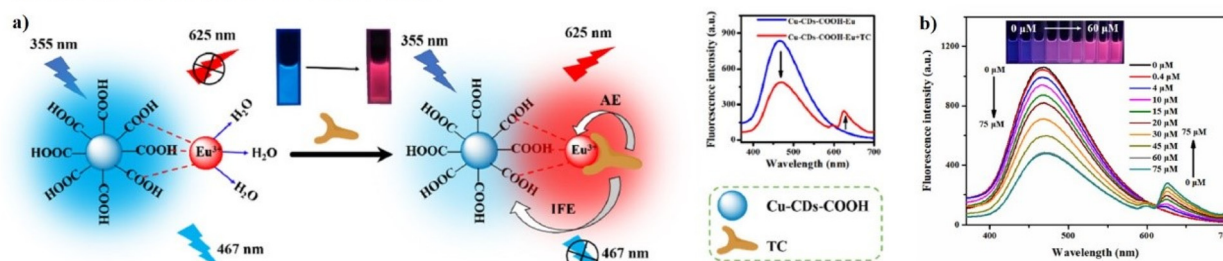
B. Eu-TCA/NCDs complex for detection of CAP based on turn off mode
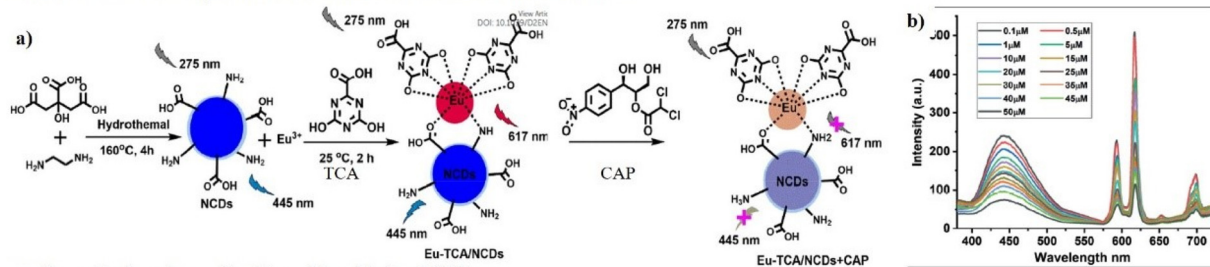
C. Target induced coordination of two kinds of FNPs
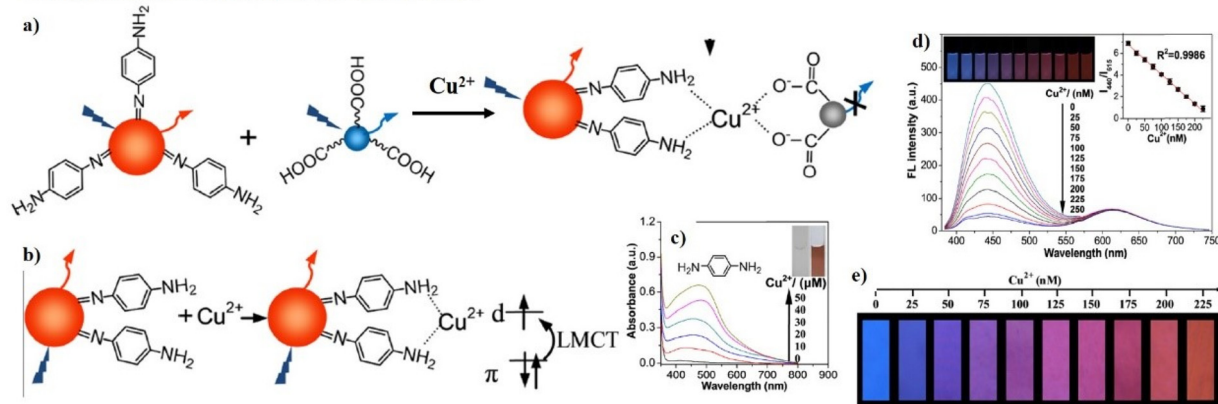
Fig. 8 (A) CDs coordinated with Eu³⁺ for the detection of TC. (a) An illustration of the mechanism for the detection of TC based on AE and (b) the fluorescence spectra of CDs@Eu³⁺ with different concentrations of TCs. (a and b) Reproduced with permission from ref. 105. Copyright 2016, Elsevier. (B) The Eu-TCA/NCDs complex for the detection of CAP based on the turn-off mode. (a) An illustration of the preparation and mechanism for the detection of CAP and (b) the fluorescence spectra of Eu-TCA/NCDs with different concentrations of CAP. (a and b) Reproduced with permission from ref. 117. Copyright 2022, the Royal Society of Chemistry. (C) The target-induced coordination of two types of FNPs. (a) A schematic illustration of the conjugation of b-CDs and r-CDs through a Cu²⁺-ion bridge, (b) interaction between r-CDs and Cu²⁺ ions by LMCT, (c) the UV–vis spectra of pure p-PDA after the addition of Cu²⁺ ions, (d) the fluorescence spectra of a mixture of b-CDs and r-CDs with the addition of Cu²⁺ ions, and (e) the visualization of Cu²⁺ ions using fluorescent test papers prepared by printing dual-colored CDs ink on a piece of filter paper. (a)–(e) Reproduced with permission from ref. 119. Copyright 2017, the American Chemical Society.

and exist in solution. During the formation of the MOFs, the FNPs or dyes are encapsulated in the pores of MOFs.

The encapsulation of dyes in LMOFs is a commonly employed method to construct DRFPs. The small size of organic dyes allows them to easily encapsulated in the pores of MOFs and dispersed uniformly, thus avoiding ACQ. Many dye@MOF composites have been explored for the detection of metal ions,[121–129] antibiotics,[130–132] food additives,[133,134] explosives,[135–137] pesticides,[138–140] medicine,[141] and water in organic solvents.[142] In addition to dyes, CDs, QDs, and Ru (bpy)₃²⁺ can also be encapsulated in LMOFs to avoid their agglomeration and improve their stability. Many excellent works on FNPs encapsulated in MOFs have been reported, such as

CDs encapsulated in Eu-MOFs for the detection of the water content in organic solvents[143] or detection of antibiotics,[144] CDs encapsulated in the Zr-MOF PCN-222 for the detection of pesticides,[145] CDs encapsulated in Eu-DPA-MOF for the detection of Cu²⁺,[146] CDs encapsulated in Eu-MOF for the detection of Cr⁶⁺,[147] CDs encapsulated in UiO-66-(COOH)₂ for the detection of Cu²⁺,[148] CdTe QDs encapsulated in the NH₂-MIL-53(Al) MOF for the detection of 6-mercaptopurine,[149] in situ growth of CsPbBr₃ QDs in Eu-BTC for the detection of Hg²⁺,[150] and Ru (bpy)₃²⁺ encapsulated in blue emission UiO-66-NH₂ by situ encapsulation method for the detection of Hg²⁺.[151]

For this type of DRFP, the encapsulated fluorescence guest can act as the response signal, while the MOFs play multiple
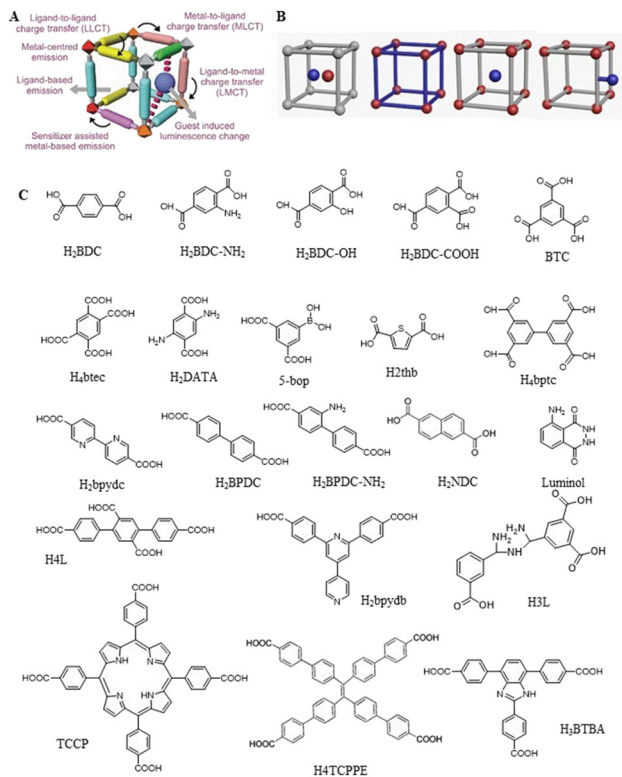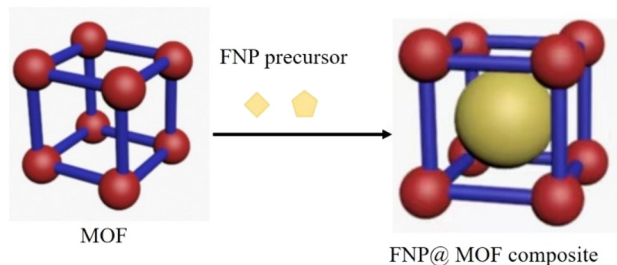
Fig. 9 (A) A schematic representation of the various possibilities contributing to the emission of MOFs. Reproduced with permission from ref. 120. Copyright 2017, the Royal Society of Chemistry. (B) MOF-based DRFPs synthesized by different design schemes. (C) Some commonly used fluorescent organic ligands for the construction of LMOFs.
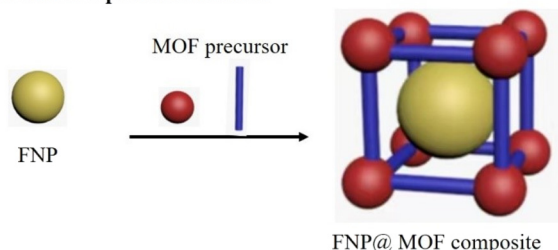

Fig. 10 Methods for the preparation FNP@MOF composites. (a) Ship in bottle and (b) bottle around ship.

functions, such as reference signal, stabilizing the fluorescence guest and accumulating the target to improve the detection sensitivity. For example, Hu's group synthesized

dual-emission CsPbBr$_3$@Eu-BTC *via* the *in situ* growth of CsPbBr$_3$ nanocrystals in Eu-BTC for the detection of Hg^{2+}.[131] As shown in Fig. 11A, the Eu-MOF prepared using 1,3,5-trimesic acid (H$_3$BTC) as the ligand displayed the red emission of the sensitized Eu^{3+}. Then, CsPbBr$_3$ QDs were grown in the pores of Eu-BTC by the *in situ* growth method. After the addition of Hg^{2+}, the green fluorescence of CsPbBr$_3$ QDs was quenched, which was attributed to the effective electron transfer process from CsPbBr$_3$ to the Hg^{2+} ions. Eu-BTC acted as the carrier and internal standard. The color of DRFP changed from green to red when increasing the concentration of Hg^{2+}.

In some cases, the MOF acts as the response signal and the encapsulated FNPs act as the reference. For example, Pei *et al.* encapsulated Ru(bpy)$_3$$^{2+}$ in the blue-emission UiO-66-NH$_2$ *via* the *in situ* encapsulation method for the detection of Hg^{2+}, as shown in Fig. 11B. UiO-66-NH$_2$ was prepared using 2-aminoterephthalic acid (H$_2$BDC-NH$_2$) as the ligand, providing rich amino groups to coordinate with Hg^{2+}. The electrode potential of Hg^{2+}/Hg is 0.85 eV, which is located between the conduction band of UiO-66-NH$_2$, leading to PET from UiO-66-NH$_2$ to Hg^{2+}. Thus, with the addition of Hg^{2+}, the blue fluorescence of UiO-66-NH$_2$ was quenched due to the coordination of the H$_2$BDC-NH$_2$ ligand with Hg^{2+}. Meanwhile, Ru(bpy)$_3$$^{2+}$ was unsusceptible to Hg^{2+}, as acting as the internal reference.[151]

In some cases, both the LMOF and the encapsulated FNPs respond to the target, inducing DRFPs with two reversible signal changes.[143,149] For example, Chi's group encapsulated b-CDs in red emitting Eu-MOFs *via* the "*in situ* growth" method for the detection of water in organic solvents.[143] In organic solvents, the encapsulated b-CDs aggregated and exhibited a weak blue signal. When Eu-MOFs/b-CDs were dispersed in water, the encapsulated b-CDs were released from the MOF, displaying bright blue emission. Meanwhile, the red emission of the Eu-MOFs was quenched due to the effect of the O–H oscillators. Even a slight increase in the water content in ethanol could induce an obvious color change.

In the case of non-fluorescent MOFs, DRFPs can be constructed by encapsulating two types of fluorescent guest.[152–155] The role of the host MOFs was to efficiently accumulate the target analytes. For example, Hu's group incorporated red-emission CdTe/CdS/ZnS QDs and b-CDs in a zeolitic imidazolate framework (ZIF-8) using a one-pot *in situ* growth method for the detection of Cu^{2+}. ZIF-8 is rich in acid–base groups and pores, which is beneficial to conveniently accumulate target analytes. With the addition of Cu^{2+}, Cu^{2+} bound on the surface of the QD and replaced Cd^{2+}, thus forming low-soluble CuTe particles on the surface of QDs, which quench the fluorescence of the QDs. During the detection process, the fluorescence intensity of b-CDs remained stable as the reference.

Another strategy to construct DRFPs using non-fluorescent MOFs is the multi-step method. Initially, a fluorescent guest can be encapsulated in a non-fluorescent MOF to form a single-emission MOF, and then a second fluorescence signal is introduced by post-modification. Generally, lanthanide ions
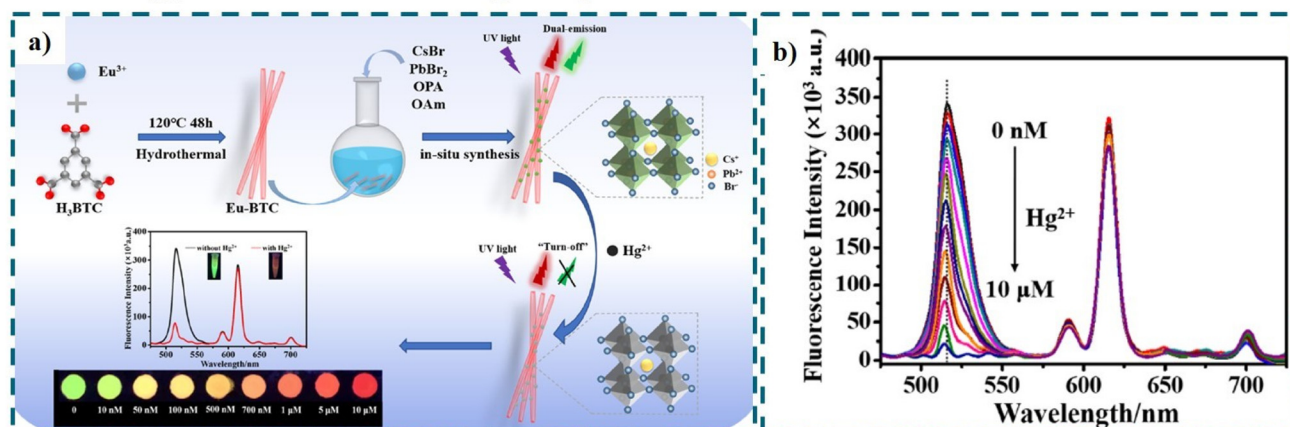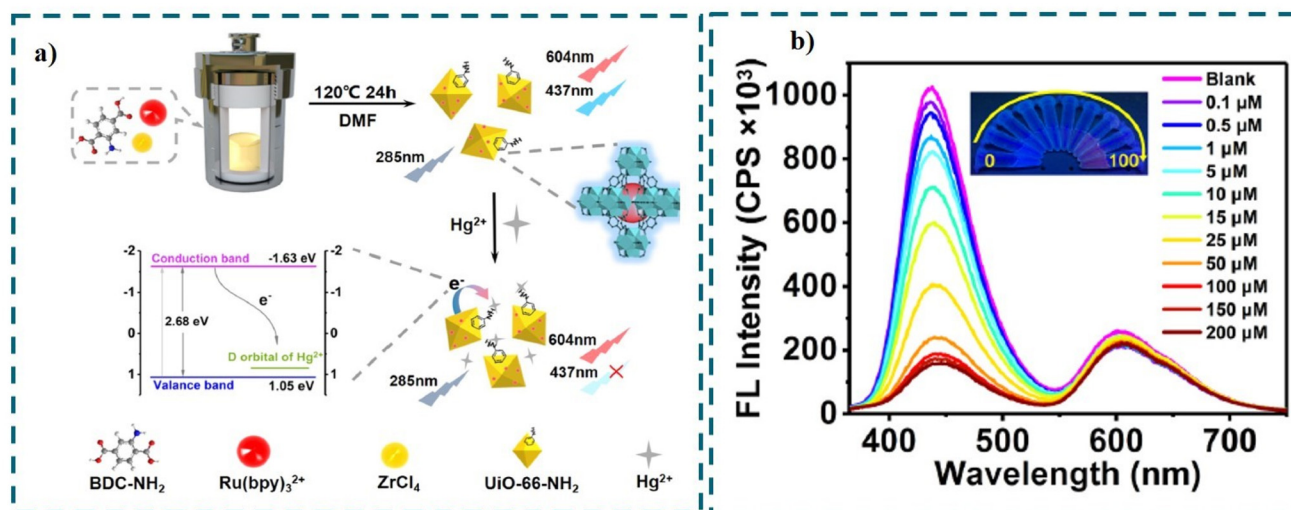
A. CsPbBr$_3$@Eu-BTC for detection of Hg^{2+} using Eu-MOF as reference

B. Ru (bpy)$_3$$^{2+}$ @UiO-66-NH$_2$ for detection of Hg^{2+} using MOF as response signal

Fig. 11 (A) CsPbBr$_3$@Eu-BTC for the detection of Hg^{2+} using Eu-MOF as a reference. (a) An illustration of the preparation and detection of CsPbBr$_3$@Eu-BTC and (b) the fluorescence spectra of CsPbBr$_3$@Eu-BTC with different concentrations of Hg^{2+}. (a and b) Reproduced with permission from ref. 131. Copyright 2022, Elsevier. (B) Ru(bpy)$_3$$^{2+}$@UiO-66-NH$_2$ for the detection of Hg^{2+} using an MOF as the response signal. (a) An illustration of the preparation and detection of Ru(bpy)$_3$$^{2+}$@UiO-66-NH$_2$ and (b) the fluorescence spectra of Ru(bpy)$_3$$^{2+}$@UiO-66-NH$_2$ with different concentrations of Hg^{2+}. (a and b) Reproduced with permission from ref. 151. Copyright 2023, Elsevier.

such as Eu^{3+} or Tb^{3+} are introduced by post-modification to form DRFP.[156–160] For example, Si-QDs were first encapsulated in the UiO-66-(COOH)$_2$ MOF by the *in situ* growth method, and further Eu^{3+} was decorated on its surface due to the coordination of free carboxyl groups and Eu^{3+}. With the addition of TC, the emission of the Si-QDs at 472 nm was quenched based on IFE, and the potential red emission of Eu^{3+} at 616 nm increased significantly due to AE, accompanied by obvious blue-red color switching.[156] Xu *et al.* encapsulated b-CDs in MOF-253 crystals *via* the *in situ* growth method. Then, Eu^{3+} was anchored to CD@MOF-253 by post-modification method. After coordination with Eu^{3+}, the product showed both the CD-centred emission and Eu^{3+}-characteristic sharp emissions. With the addition of Hg^{2+}, the emission of b-CDs was quenched due to the formation of a stable chelate with Hg^{2+}, while Eu^{3+} remained unchanged as the internal reference.[157]

3.2 FNPs with intrinsic dual emission

As discussed above, the construction of DRFPs always involves a "multi-step" approach, including the preparation of two types of FNPs separately, and then their assembly through physical or chemical reactions. However, the whole process is time-consuming and tedious. Thus, FNPs with intrinsic dual-emission properties are competitive for the construction DRFP. Thus, dual-emissive FNPs, including dual-emissive CDs (D-CDs), dual-emissive QDs (D-QDs), dual-emissive MOFs (D-MOFs), and dual-emissive nanohybrids (D-NH), have ushered in the rapid development of modification-free DRFPs. Specifically, the design and preparation of these dual-emission FNPs are the key to this strategy.

3.2.1 D-CDs. Since the first D-CD-based DRFP was presented in 2013,[161] numerous D-CDs have emerged. The fluo-

rescence of CDs may originate from the electronic conjugate structures and surface energy traps. The fluorescence properties of CDs may be governed by their carbon source, doped atoms, and solvent.[162] Table 2 presents a summary of the carbon source, solvent and optical property of some D-CDs.[163–190]

3.2.1.1 Single-excitation dual-emission CDs. The heteroatom doping can introduce electron donors or acceptors in the structures of CDs, and thus change their optical properties. The incorporation of N, B, O, and S, in CDs is a promising approach to vary the photoluminescence colors of D-CDs. For example, using *o*-phenylenediamine (*o*-PD) as the main precursor, different co-precursors resulted in the formation of D-CDs with different properties.[163–169] The CDs prepared using *o*-PD as a single precursor displayed bright green emission. When lysine (Lys) was used as a co-precursor and modulator, blue emission appeared because the introduction of MIPs efficiently suppressed the carbonization of the *o*-PD polymer chains.[163] When polyethylene glycol (PEG) and oxalic acid were used as a co-precursor, D-CDs with two emission peaks at 393 and 580 nm were prepared *via* a one-step hydrothermal method,[165] in which PEG acted as a surface passivation agent and oxalic acid offered rich-oxygen groups. When using oxalic acid as the co-precursor, D-CDs with two emission peaks at 453 nm and 560 nm were prepared.[166]

D-CDs can be prepared with a single carbon source by selecting ideal precursors containing heteroatoms.[184,185] For example, red/green D-CDs were synthesized using 2,5-di-aminotoluene sulfate as the only carbon source.[184] The presence of a C–S bond indicated the successful doping of S atoms in the D-CDs. The as-prepared D-CDs emitted fluorescence at 525 nm and 603 nm under the excitation of 370 nm, which could be directly utilized for the determination of trace $ONOO^-$. The green fluorescence at 525 nm decreased gradually with an increase in the concentration of $ONOO^-$ due to the electron transfer process, while the change in red fluorescence was negligible. Similarly, Alizarin carmine was used as the only carbon source to prepare blue and red D-CDs with emissions centred at 430 and 642 nm, respectively, for the detection of GSH.[185] The dual emission possibly stems from the conjugated aromatic π systems and the doping of S atoms. Because the disulfide bond was reduction sensitive and broken by the reduction of glutathione, the surface structure of the CDs was destroyed in the presence of GSH, inducing an increase in the blue emission and slight decrease in the red emission.

Doping metal ions, such as Cu^{2+}, Cd^{2+}, and Gd^{3+} can also be employed to prepare D-CDs.[171–173] For example, Tan *et al.* synthesized D-CDs using 1-(2-pyridylazo)-2-naphthol as the precursor and Cu^{2+} as the doping agent *via* the one-pot solvothermal method.[171] The prepared D-CDs exhibited two emissions at 426 and 488 nm under excitation at 350 nm. The larger conjugate planar structure from the 1-(2-pyridylazo)-2-naphthol precursor resulted in the host fluorescence emission. The conjugate structure could interact with Cu^{2+}. Therefore, the excited-state electron transfer to the copper energy level

induced a new emission. The as-prepared D-CDs could be employed to detect Fe^{3+}, AA and pH, respectively.

The solvent used in the hydrothermal process also plays a vital role in the optical property of as-prepared D-CDs. CDs prepared using *o*-PD as a single carbon source by the hydrothermal method in water displayed strong green fluorescence.[163] However, when using phosphoric acid as the solvent, the as-prepared CDs exhibited blue and red fluorescence at 440 and 624 nm simultaneously.[170] The red emission may have originated from the synergistic effect from the concentrated H_3PO_4 and the structure of *o*-PD. Interestingly, this probe exhibited two distinct responses toward lysine and pH. As shown in Fig. 12A, in the detection of lysine, the blue emission of D-CDs at 440 nm was enhanced due to their surface passivation, while the red emission at 624 nm remained constant. In the detection of pH in the range of 1.5–5.0, the red emission of D-CDs at 624 nm decreased, while the fluorescence emission at 440 nm remained stable. The response of red emission toward pH may have originated from the protonation and deprotonation of the doped N atom in the rigid carbon skeleton structure.

Chen's group discussed the role of the solvent in the formation of D-CDs using dicyandiamide and *o*-PD as the carbon source.[180] Hydrothermal treatment of dicyandiamide and *o*-PD in dilute H_2SO_4 resulted in the formation of D-CDs with emissions centred at 630 and 680 nm. Without H_2SO_4, the as-synthesized CDs showed single yellow emission at 580 nm. Using HNO_3 instead of H_2SO_4, the CDs showed yellow-green emission at about 576 nm, while other acids (such as hydrochloric acid and phosphoric acid) resulted in weak red emission. It was inferred that *o*-PD, dicyandiamide, hydrogen ion, and sulfate ion work together in the preparation of D-CDs.

When organic dyes are used as one of the starting materials, the prepared CDs display a fluorescence emission similar to the used dyes.[174–179] For example, using citric acid and basic fuchsine as precursors, Dong's group prepared D-CDs with dual emission at 478 and 552 nm upon excitation at 377 nm.[175] With the addition of ClO^-, the fluorescence at 552 nm was quenched dramatically due to the oxidation reaction, while the blue emission remained unchanged.

As mentioned above, element doping and dye doping are effective ways to prepare D-CDs. Therefore, the use of biomass rich in N, S atoms and chlorophyll as the carbon source is a green method to prepare D-CDs.[180–183] For example, using corn bract as the raw material, D-CDs with dual emission at 470 and 678 nm were prepared for the detection of Hg^{2+}.[180] The blue emission may be from the intrinsic emission of the CDs, while the red emission may originate from the porphyrins derived from chlorophyll. Hg^{2+} could quench the red emission through interaction with the electron-rich aromatic ring and had a slight effect on the blue emission. Liu *et al.* prepared D-CDs with dual emission at 470 nm and 670 nm using plant leaves as the precursor without any further treatment for the detection of Al^{3+} and H_2O, respectively.[181] The emission at 470 nm originated from the intrinsic structure of CDs, and the red emission at 670 nm was similar to the chlorophyll-derived

Table 2 The carbon source and optical property of D-CDs

Ser.	Carbon source	Solvent	Preparation method	Emission peak	Detection target	Ref.
1	*o*-PD and lysine	Water	Hydrothermal	390 nm and 520 nm	Solution polarity	163
2	*o*-PD and dicyandiamide	Dilute sulfuric acid	Hydrothermal	630 nm and 680 nm	Methyl blue, pH	164
3	*o*-PD, PEG and oxalic acid	Water	Hydrothermal	393 nm and 580 nm	pH	165
4	*o*-PD and oxalic acid	Water	Hydrothermal	453 nm and 560 nm	L-Glutamic acid	166
5	*o*-PD and ethanolamine	Ethanol	Hydrothermal	430 nm and 550 nm	2,4,6-Trinitrophenol	167
6	*o*-PD and 3-carboxyphenylboronic acid	Water	Hydrothermal	356 nm and 700 nm	IO_4^-	168
7	*o*-PD and DPA	Water (pH 12.2) with H_2O_2	Hydrothermal	460 nm and 540 nm	pH value and bilirubin	169
8	*o*-PD	H_3PO_4	Solvothermal	440 nm and 624 nm	Lysine and pH	170
9	PAN and $CuCl_2$	Ethanol	Hydrothermal	426 nm and 488 nm	Fe^{3+}, pH	171
10	PAN and $CuCl_2$	Ethanol	Hydrothermal	426 nm and 488 nm	Thiophanate-methyl	172
11	$Gd(NO_3)_3 \cdot 6H_2O$ and 3-aminothiophenol	Ethanol	Solvothermal	415 nm and 485 nm	Motin	173
12	Citric acid and basic fuchsin	Water	Hydrothermal	475 nm and 545 nm	PH	174
13	Citric acid and RhB	Water	Hydrothermal	415 nm and 580 nm	HClO	175
14	Neutral red and urea	Water	Hydrothermal	440 nm and 542 nm	L-Lysine	176
15	Citric acid, EDA and BrNpA	Ethanol	Hydrothermal	459 nm and 539 nm	FA, HSO_3^- and pH	177
16	PEI and TCPP	Water	Hydrothermal	471 nm and 665 nm	pH	178
17	Acid fuchsin and citric acid	Water	Hydrothermal	478 nm and 552 nm	HClO	179
18	Biomass corn bract	Ethanol	Hydrothermal	470 nm and 678 nm	Hg^{2+}	180
19	Plant leaves	Acetone	Hydrothermal	470 nm and 670 nm	Al^{3+}	181
20	Fresh spinach + PEG-NH_2			488 nm and 678 nm	Coenzyme A	182
21	Spinach + ethylenediamine	Water	Hydrothermal	477 nm and 651 nm	Pb^{2+}	183
22	2,5-Diaminotoluene sulfate	Ethanol	Hydrothermal	525 nm and 603 nm	$ONOO^-$	184
23	Alizarin carmine	Water	Hydrothermal	430 nm and 642 nm	GSH	185
24	AA	Ethylene glycol–water binary reaction media	Hydrothermal	410 nm and 530 nm	Captopril	186
25	Glutathione and polyethylenimine	Formamide	Solvothermal	460 nm and 680 nm	Lysozyme	187
26	Sodium alginate (SA) and glutathione (GSH)	Formamide	Solvothermal	480 nm and 650 nm	Fe^{3+}	188
27	*p*-Aminoazobenzene and *p*-phenylenediamine	Deionized water	Hydrothermal	508 nm and 610 nm	Acid red 18	189
28	Phloroglucinol dihydrate, boric acid and ethylenediamine	Water	One-step microwave method	484 nm and 565 nm	—	190

porphyrins. The presence of Al^{3+} induced the aggregation of CDs by coordinating with the amino groups of D-CDs, and then induced an enhancement in the blue emission. The presence of H_2O induced hydrophobicity in the chlorophyll-derived porphyrins structure, and then quenched the red fluorescence.

3.2.1.2 Dual-excitation dual-emission CDs. The above-discussed D-CDs displayed two emissions under single excitation.

Alternatively, some D-CDs display dual emission under two different excitation wavelengths, which are called dual-excitation dual-emission CDs (DD-CDs). For example, Li's group synthesized DD-CDs using tetrachlorobenzoquinone and ethylenediamine as raw materials by Schiff base condensation reaction for the detection of vitamin B12.[191] As shown in Fig. 12B, the blue emission located at 445 nm could be observed when excited at 350 nm and yellow emission located at 575 nm
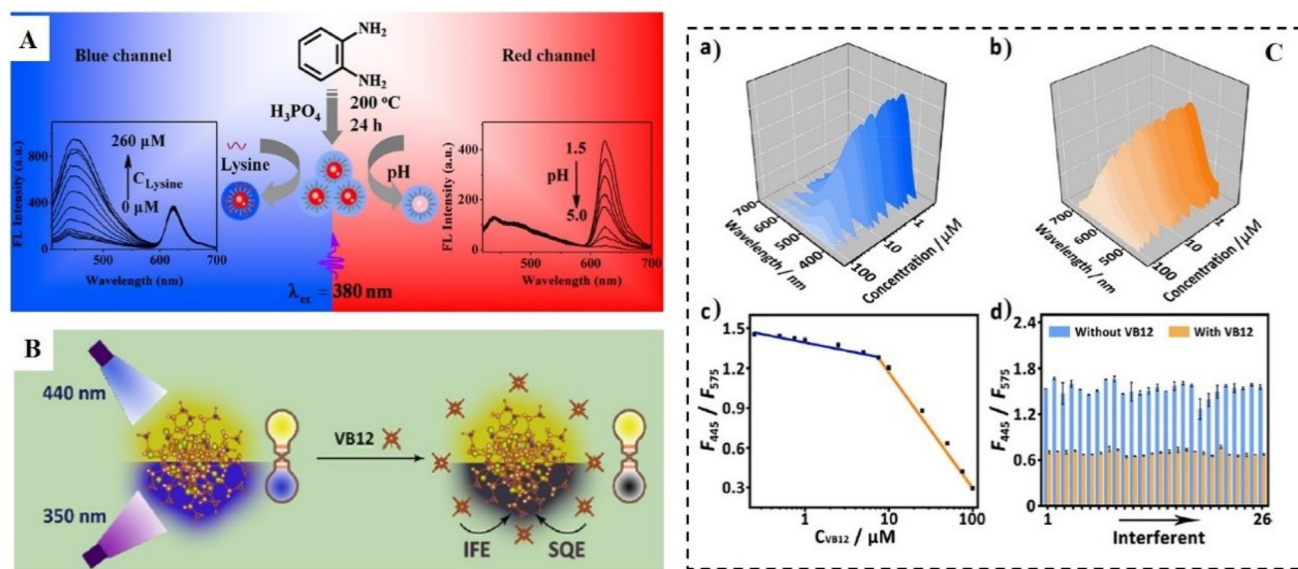
Fig. 12   (A) A schematic diagram of the procedure for the preparation of D-CDs and specific ratiometric detection of lysine and pH. Reproduced with permission from ref. 170. Copyright 2017, the American Chemical Society. (B). A schematic diagram of the application of DD-CDs for the detection of VB12. (C) Changes in the FL spectra of DD-CDs for the detection of VB12. (a) Blue emission channel and (b) yellow emission channel after the addition of VB12. (c) The sensitivity of VB12 sensing and (d) the FL responses of DD-CDs in the presence of different interferents. (B and C) Reproduced with permission from ref. 191. Copyright 2021, the American Chemical Society.

appeared when excited at 440 nm. The blue channel at 445 nm could be quenched by VB12 based on IFE, while the yellow emission served as a reference signal to avoid the background interference. For this type of DD-CDs, the two fluorescence signals need to be detected on the two excitation channels respectively, as shown in Fig. 12C.

Jia's group prepared DD-CDs with a dual-emission band centre at 450 nm when excited at 360 nm and 535 nm when excited at 490 nm by the hydrothermal method using 3-aminophenylboronic acid as the carbon source.[192] After the addition of Cr(VI), the blue emission was weakened because of IFE, while the green emission remained stable. Further, upon the addition of bisulfite, the weakened blue emission was restored, while the green emission was quenched. Bisulfite could reduce Cr^{6+} to Cr^{3+}, and then the IFE from Cr^{6+} was inhibited, which resulted in the enhancement of blue emission. However, the quenching mechanism for the green emission was not discussed. Our group synthesized blue and red dual-channel DD-CDs *via* a one-step hydrothermal method in a water–formamide binary system using citric acid and ethylenediamine as precursors.[193] The as-prepared DD-CDs displayed dual emission bands centred at 440 nm when excited at 365 nm and 580 nm when excited at 520 nm. Given that Cr^{3+} could only quench the blue emission, and Pb^{2+} only quenched the red emission, enabling the detection of Cr^{3+} and Pb^{2+} simultaneously under the dual channel. For this type of DD-CD, the two emission spectra should be measured under different excitation wavelengths. Thus, the detection process is more complex.

3.2.2   Dual-emissive MOFs (D-MOFs). Generally, the fluorescence of MOFs may originate from organic ligands, lantha-

nide metals or fluorescent guests. By rationally integrating the above-mentioned fluorescence sources, D-MOFs with excellent performance can be constructed. Considering that the different types of fluorescent guests encapsulated in D-MOFs were discussed in section 3.1.6, in this part, D-MOFs originating form organic ligands or lanthanide metals are discussed. Table 3 lists some of the D-MOFs originating from organic ligands and lanthanide metals.[194–225]

3.2.2.1   Single-ligand and single-metal ion D-MOF. The fluorescence of single-ligand and single-metal ion D-MOFs originates from the fluorescence of both the organic ligand and the sensitized lanthanide ions. This type of D-MOF may display strong ligand-centred emission and weak lanthanide ion emission due to their poor energy transfer, which can be designed for the detection of sensitizers. For example, Xiao's group prepared Tb-PTA-OH using the fluorescence ligand *p*-phthalic acid–OH (PTA-OH), which displayed a strong ligand emission at 436 nm and very weak Tb^{3+} emission at 551 nm.[194] The addition of DPA sensitized and enhanced the green emission of Tb^{3+}, while effect on the blue emission from the ligand was slight. Thus, a fluorescence color change from dark blue to green could be observed. If the fluorescence organic ligand can sensitize lanthanide ions effectively, D-MOFs with strong lanthanide ion emission and weak ligand emission can be prepared.[195,196] For example, Eu-BBDC was prepared using 5-borylbenzene-1,3-dicarboxylic acid (BBDC) as the ligand, which exhibited both the weak blue emission of the BBDC ligand at 370 nm and the strong emission of Eu^{3+} at 618 nm.[195] BBDC with boric acid group could specifically recognize ribavirin by forming an ester ring in alkaline solution. With the addition of ribavirin, the ligand-centred emis-

Table 3 The metal ions and ligands of D-MOFs

Ser.	D-MOF	Metal ions	Ligand	Preparation method	FL centre 1 (nm)	FL centre 2 (nm)	Target	Ref.
1	Tb-PTA-OH	Tb^{3+}	PTA-OH	One-pot hydrothermal	PTA-OH (436 nm)	Tb^{3+} (551 nm)	DPA	194
2	Eu-BBDC	Eu^{3+}	BBDC	One-pot hydrothermal	BBDC (370 nm)	Eu^{3+} (618 nm)	Ribavirin	195
3	Tb-BPTC	Tb^{3+}	BPTC	One-pot hydrothermal	BPTC (420 nm)	Tb^{3+} (551 nm)	ALP	196
4	Eu-BDC–CH=CH$_2$	Eu^{3+}	BDC–CH=CH$_2$	One-pot hydrothermal	BDC–CH=CH$_2$ (367 nm)	Eu^{3+} (618 nm)	H$_2$S	197
5	Eu-DMTP-DC	Eu^{3+}	H$_2$DMTP-DC	One-pot hydrothermal	H$_2$DMTP-DC	Eu^{3+} (618 nm)	Arg	198
6	Eu-DATA/BDC	Eu^{3+}	H$_2$BDC, H$_2$DATA	One-pot hydrothermal	H$_2$DATA (465 nm)	Eu^{3+} (618 nm)	Cu^{2+}	199
7	Eu-BDC-NH$_2$/DPA.	Eu^{3+}	BDC-NH$_2$, DPA	One-pot hydrothermal	BDC-NH$_2$ (433 nm)	Eu^{3+} (618 nm)	HClO	200
8	Luminol-Tb-GMP	Tb^{3+}	Luminol, GMP	One-pot hydrothermal	Luminol (392 nm)	Tb^{3+} (547 nm)	Amyloid β-peptide	201
9	Luminol-Tb-GMP	Tb^{3+}	Luminol, GMP	One-pot hydrothermal	Luminol (392 nm)	Tb^{3+} (547 nm)	pH	202
10	Eu-BTC-BDC-NH$_2$	Eu^{3+}	BTC, BDC-NH$_2$	One-pot hydrothermal	BDC-NH$_2$ (425 nm)	Eu^{3+} (614 nm)	Phosphate	203
11	Tb-ATA/GDP	Tb^{3+}	ATA, GDP	One-pot hydrothermal	ATA (430 nm)	Tb^{3+} (549 nm)	H$_2$O$_2$	204
12	NH$_2$-BDC–Tb-GMP	Tb^{3+}	NH$_2$-BDC, GMP	Self-assembly	BDC-NH$_2$ (425 nm)	Tb^{3+} (549 nm)	phosphate	205
13	Tb97.11Eu2.89-L1	Tu, Eu^{3+}	H6L1	Mixed Ln-MOF	Tb^{3+} (547 nm)	Eu^{3+} (621 nm)	Water in organic	206
14	Ce-Tb@GMP	Ce, Tb^{3+}	GMP	One-pot hydrothermal	Ce weak (384 nm)	Tb^{3+} (545 nm)	Alkaline phosphatase	207
15	Eu/Tb(HFA)	Eu/Tb	HFA	Ion exchange	Tb^{3+} (543 nm)	Eu^{3+} (614 nm)	Histamine	208
16	Eu0.02Dy0.18-MOF	Eu, Dy	H$_4$L	One-pot hydrothermal	Dy 480 (573 nm)	Eu^{3+} (614 nm)	Water	209
17	Gd$_{0.9}$Tb$_{0.1}$HL	Gd, Tb^{3+}	H$_4$L	One-pot hydrothermal	H$_4$L	Tb^{3+} (545 nm)	Temperature	210
18	Tb$_{0.01}$Gd$_{0.99}$L	Tb, Gd	H$_4$L	Mixed one-pot hydrothermal	H$_4$L (380 nm)	Tb^{3+} (545 nm)	Picric acid	211
19	Ca-MOF-Eu^{3+}	CaCl$_2$	H$_2$thb	PSM Eu^{3+}	H$_2$thb (380 nm)	Eu^{3+} (590 nm)	Hg^{2+}	212
20	Tb^{3+}@Cu-MOF	Cu	HCPOC	PSM Tb^{3+}	H$_2$CPOC	Tb^{3+} (545 nm)	H$_2$S	213
21	Eu3+@Mn-MOF	Mn	Htpbpc	PSM Eu^{3+}	Htpbpc (500 nm)	Eu^{3+} (617 nm)	Histidine	214
22	Eu@bpy-UiO	ZrCl$_4$	bpy	PSM Eu^{3+}	Bpy (535 nm)	Eu^{3+} (621 nm)	VOC	215
23	Eu/BPyDC@MOF-253-NH$_2$	Al	H$_2$N-BPDC$_2$, BPyDC^{2-}	PSM Eu^{3+}	H$_2$NBPDC$_2$ (471 nm)	Eu^{3+} (614 nm)	ClO$^-$ AA	216
24	Eu-UiO-66	Zr	H$_2$BDC-OH, H$_4$btec	PSM Eu^{3+}	H$_2$BDC-OH (450 nm)	Eu^{3+} (614 nm)	Al^{3+}	217
25	Eu^{3+}/Cu^{2+}@UiO-66-(COOH)$_2$	Zr	H$_4$btec	PSM Eu^{3+}	H$_4$btec (393 nm)	Eu^{3+} (614 nm)	H$_2$S	218
26	Eu^{3+}/Ag$^+$@UiO-66-(COOH)$_2$	Zr	H$_4$btec	PSM Eu^{3+}	H$_4$btec (393 nm)	Eu^{3+} (614 nm)	Formaldehyde	219
27	Tb@UiO-66-(COOH)$_2$NH$_2$	Zr	H$_4$btec	Incorporation of Tb^{3+} and H$_2$atp	H$_2$atp (433 nm)	Tb^{3+} (545 nm)	TCBQ	220
28	Eu@UiO-66-(COOH)$_2$	Zr	H$_4$btec	PSE H$_2$NDCPSM Eu^{3+}	H$_2$NDC (430 nm)	Eu^{3+} (614 nm)	Temperature	221
29	Tb^{3+}-NOTT-220	Bi	H$_4$BPTC	Doping Tb^{3+}	H$_4$BPTC 350 (nm)	Tb^{3+} (545 nm)	Serotonin	222
30	UiO-66(Zr&Eu)	Zr, Eu	H$_2$NDC	One-pot hydrothermal	H$_2$NDC (430 nm)	Eu^{3+} (614 nm)	Temperature	223
31	Eu/Fe-MOFs	Fe, Eu	TPA	One-pot hydrothermal	TPA (458 nm)	Eu^{3+} (614 nm)	H$_2$O$_2$	224
32	Tb/Eu@bio-MOF-1	Zn	BPDC	PSM Eu^{3+} and Tb^{3+}	Tb^{3+} (549 nm)	Eu^{3+} (614 nm)	DPA	225

sion increased, while the lanthanide ion-centred emission decreased. Inserting functional groups in ligands is an effect way to adjust the energy transfer to the prepared D-MOF with two bright emissions.[197,198] For example, He's group prepared Eu-BDC–CH=CH$_2$ using 2-vinylterephthalic acid (H$_2$BDC–CH=CH$_2$) as the organic ligand.[197] The vinyl groups attached to the benzene skeleton resulted in a high energy-back transfer from Eu^{3+} to the ligand, and thus Eu-BDC–CH=CH$_2$ displayed a ligand-centred emission at 367 nm and Eu ion-centred emission at 615 nm. In the presence of H$_2$S, the characteristic peak of the Eu^{3+} ions significantly decreased, while the ligand-centred emission was enhanced due to the electrophilic addition reaction between H$_2$S and vinyl functional groups.

3.2.2.2 Dual-ligand single Ln ion D-MOFs. The design and choice of ligand are very important in designing the single-ligand and single-metal ion type of D-MOFs. The energy transfer should be adjusted to keep the two emissions. However,

the process of screening ligands is complicated. Thus, to solve this problem, dual-ligand provides an efficient and robust strategy to prepare D-MOFs, where one ligand sensitizes the Ln^{3+} ions and the other maintains its own emission.[199–205] In some designs, the fluorescence ligand has a specific site to recognize the target.[199,200] For example, the dual-ligand Eu-DATA/BDC MOF was prepared using terephthalic acid (H$_2$BDC) to sensitize Eu^{3+} ions and 2,5-diaminoterephthalic acid (H$_2$DATA) maintained its own emission and provided amino group to specifically recognize Cu^{2+} ions, as shown in Fig. 13A.[199] The Cu^{2+} ions interacted with the amino groups in Eu-DATA/BDC and quenched the DATA-centred blue emission. The AE procedure was not affected, and thus the red emission was from Eu^{3+} as the reference. Sun *et al.* prepared Eu-BDC-NH$_2$/DPA using 2-aminoterephthalic acid (BDC-NH$_2$) and dipicolinic acid (DPA) as dual ligands.[200] BDC-NH$_2$ was selected because of its response to ClO$^-$ and bright blue fluo-

rescence emission, while DPA was employed to sensitize Eu^{3+} ions. With the addition of ClO^-, a hydrogen bond was formed between the $-NH_2$ group of BDC-NH_2 and HClO, which weakened the blue fluorescence derived from BDC–NH_2 at 433 nm, while the sensitized Eu^{3+} ions were not affected.

In another design, the sensitized Ln ions could be blocked by the target as the response signal. For example, luminol-Tb-GMP was prepared using guanine monophosphate (GMP) to strengthen the fluorescence of Tb^{3+}, and luminol as an auxiliary fluorescence ligand.[201,202] Luminol-Tb-GMP displayed bright blue emission from luminol at 390 nm and green emission of the sensitized Tb^{3+} at 547 nm. When Cu^{2+} was introduced, the energy transfer from GMP to Tb^{3+} was impeded because of the formation of a high-affinity Cu–O bond between Cu^{2+} and GMP, which weakened the FL emission of Tb^{3+}.[201] Amyloid β-peptide with high binding affinity to Cu^{2+} could block the Cu–O bond, and further enhance the green emission of Tb^{3+}. During the whole detection process, the emission from luminol remained constant as the reference. Thus, this sensor can be employed to detect Cu^{2+} and amyloid β-peptide using this on–off-on mode.

3.2.2.3 Single-ligand bimetallic Ln-MOF. Lanthanides have similar atomic radii and coordination characteristics, and thus polymetallic lanthanide D-MOFs can be easily synthesized *via* a one-pot method. Using a ligand that is a good sensitizer for two Ln^{3+}, D-MOFs can be prepared with a dual-Ln-centred emission.[206–209] For example, Yuan and co-workers synthesized the Tb^{3+}/Eu^{3+} mixed-lanthanide $Tb_{97.11}Eu_{2.89}$-L1 by varying the original molar ratios of Tb^{3+} to Eu^{3+} under hydrothermal condition.[206] The H_6L1 ligand is a good sensitizer for Tb^{3+} and Eu^{3+} based on AE, and thus $Tb_{97.11}Eu_{2.89}$-L1 showed the characteristic emission of both Tb^{3+} at 547 nm and Eu^{3+} ions at 621 nm in dry CH_3CN. As the water content increased, AE was blocked and the emission of Tb^{3+} and Eu^{3+} decreased with different sensitivity, and the fluorescence color changed from red-orange to yellow to green. Another example is the Ce-Tb@GMP bimetallic D-MOF prepared by Liu's group *via* the self-assembly of GMP with Ce^{3+}, where Tb^{3+} displayed the bright green emissions of Tb^{3+} at 552 nm and weak blue emission of Ce^{3+} at 384 nm because both Ce^{3+} and GMP can effectively sensitize Tb^{3+}.[207] ALP can hydrolyse phosphate ester in GMP, and then reduce the energy transfer from GMP to Tb^{3+} and Ce^{3+}. Thus, in presence of ALP, both the fluorescence intensity of Ce^{3+} and Tb^{3+} declined, while Tb^{3+} was more sensitive than Ce^{3+}.

3.2.2.4 D-MOF by post-synthesis modification. Mixed-lanthanide D-MOFs usually employ Tb^{3+} (544 nm) and Eu^{3+} (616 nm), which have a fixed level gap. Post-synthetic methods provide a potential alternative for obtaining D-MOFs with a wider level gap (or wider emission range). Post-synthetic modification (PSM),[226] post-synthetic ligand exchange (PSE)[227] and post-synthetic deprotection[228] are three types of post-synthetic methods reported. The incorporation of Eu^{3+} or Tb^{3+} in ligand-centred L-MOFs is a promising way to form D-MOFs.[229–235] As shown in Fig. 13B, a dual-emission Eu-Ca-MOF was prepared by introducing Eu^{3+} ions in Ca-MOF (Ca-H_2thb) with ligand-

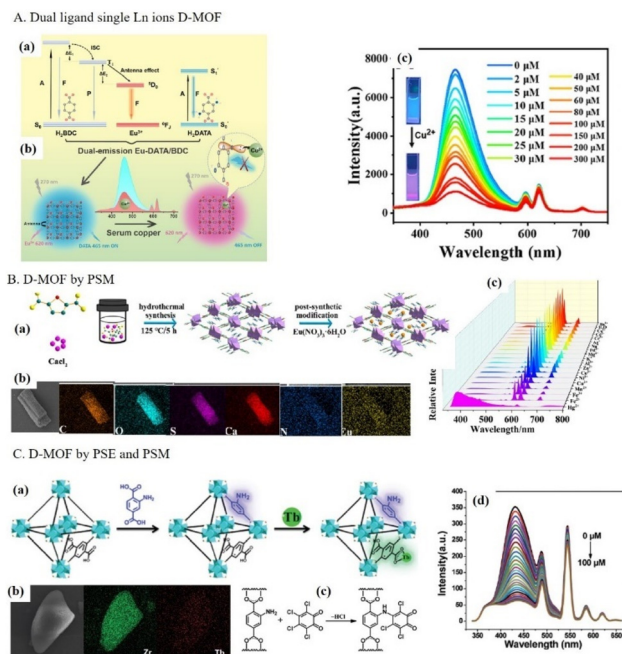**Fig. 13** (A) The design principle and preparation of Eu-DATA/BDC, where H_2BDC sensitizes Eu^{3+} ions to realize the antenna effect emission and DATA maintains its own emission and identifies Cu^{2+} ions, and the fluorescence spectra of Eu-DATA/BDC in aqueous solutions with Cu^{2+} ions at different concentrations. Reproduced with permission from ref. 199. Copyright 2022, Elsevier. (B) Eu-Ca-MOF prepared by PSM. (a) The synthesis of Eu-Ca-MOF. (b) The EDX element mapping diagram of Eu-Ca-MOFs and (c) the emission spectra of Eu-Ca-MOFs after treatment with different metal ions. Reproduced with permission from ref. 212. Copyright 2023, Elsevier. (C) The construction of D-MOFs by PSE. (a and b) The synthesis procedure, SEM image, and SEM-EDX elemental mapping of Tb@UiO-66-$(COOH)_2NH_2$. (c) The mechanism of capturing *o*-TCBQ by atp^{2-} ligand. (d) The photoluminescence spectra of Tb@UiO-66-$(COOH)_2NH_2$-40 at different concentrations of *o*-TCBQ. Reproduced with permission from ref. 220. Copyright 2016, the American Chemical Society.

centred blue emission.[212] The carboxylic acid in H_2thb provided active sites for the coordination of Eu^{3+}, while the S atom in the thiophene group provided the receptor site for Hg^{2+} recognition. The as-prepared Eu-Ca-MOF displayed the ligand- and Eu^{3+}-centred emission. Hg^{2+} could complex with S in the ligand and reduce the energy transfer from the ligand to Eu^{3+}. Thus, the addition of Hg^{2+} ions quenched the emission of Eu^{3+} and enhanced the ligand-centred blue emission. Eu-Ca-MOF displayed a wide detection range (0.02–200 μM) and a low limit detection (2.6 nM) for Hg^{2+} ions.

The carbonyl groups in UiO-66-$(COOH)_2$ provide coordination sites with Ln ions, making it a good candidate to prepare D-MOFs by PSM. For example, Yuan's group incorporated Eu^{3+} ions in UiO-66-$(COOH)_2$ by PSM. The prepared Eu-UiO-66 displayed blue emission at 450 nm from the 2-hydroxy-terephthalic acid (H_2BDC-OH) ligand and red emission at 614 nm from Eu^{3+} ions.[231] With the addition of Al^{3+}, the ligand emission was quenched, while the red emission of Eu^{3+} remained stable as the reference. The interactions between the

Al^{3+} ions and the hydroxyl O atoms led to electron transfer from H_2BDC-OH to Al^{3+}, thereby quenching the ligand-centred emission. The $I_{614\ nm}/I_{450\ nm}$ ratio was used as a metric to quantify Al^{3+} in the linear range of 0–90 μM with an LOD of 0.36 μM.

To introduce a target response site, Ln ions and auxiliary ions can be incorporated simultaneously.[218,219] For example, Qian's group encapsulated Eu^{3+} and Cu^{2+} in UiO-66-$(COOH)_2$ crystals for the detection of H_2S, in which Cu^{2+} was introduced as the target responding site.[218] Eu^{3+}/Cu^{2+}@UiO-66-$(COOH)_2$ displayed Eu^{3+}-centred emissions and H_4btec ligand-centred emission at 393 nm. The characteristic emissions of Eu^{3+} originated from the energy transfer (ET) from H_4btec to Eu^{3+}. However, the strong ligand-centred emission suggests that the ET efficiency was low. H_2S has a strong affinity for Cu^{2+} ions, and the bonding interaction between the Cu^{2+} and H_2S decreased the antenna efficiency from H_4btec to Eu^{3+}, which resulted in an enhanced Eu^{3+} emission and decreased ligand-centered emission.

In the case of non-fluorescent MOFs, fluorescence ligands can be introduced *via* a one-pot dual-ligand method[217] or PSE.[220,221] For example, Ruan's group prepared a UiO-66-based D-MOF by PSE and PSM.[220] As shown in Fig. 13C, 2-aminoterephthalate (H_2atp) was first incorporated in the non-fluorescent UiO-66 by ligand exchange processes, and then Tb^{3+} was introduced by coordination with the free carboxyl groups of UiO-66-$(COOH)_2$ to form Tb@UiO-66-$(COOH)_2$. With the addition of *o*-TCBQ, the emission of the H_2atp ligand at 433 nm was quenched obviously, while the intensity of Tb^{3+} at 545 nm was slightly reduced. Due to the different response sensitivities, *o*-TCBQ could be quantified using the intensity ratio (I_{433}/I_{545}).

Similar to D-MOF by incorporating Ln ions, dual-emission hydrogen-bonded organic frameworks (D-HOFs) can also be constructed by incorporating Eu^{3+} by PSM. For example, Yan's group prepared HOF Tt-TPA *via* the self-assembly of melamine (Tt) and terephthalic acid (H_2TPA) in aqueous medium.[222] The unbound carboxyl groups in the Tt-TPA framework provided coordination sites to load Eu^{3+}. The addition of methylamine induced a decrease in the characteristic emission of Eu^{3+}, while showing a slight effect on the ligand-centred emission at 425 nm.

3.2.2.5 D-MOFs by doping Ln ions. The preparation of D-MOFs by post modification involves two or three steps, which is time-consuming. Hence, it is challenging to synthesize D-MOFs with a wide emission range *in situ*. Doping Ln^{3+} in the synthesis solution was employed to prepare a D-MOF in one step.[223–227] For example, a D-MOF was constructed by *in situ*-doping Tb^{3+} in a Bi-MOF NOTT-220, which was synthesized using $Bi(NO_3)_3 \cdot 5H_2O$ and H_4BPTC *via* an *in situ* solvothermal method.[223] Tb^{3+}-NOTT-220 displayed a ligand-centred emission at 350 nm and the ligands sensitized the Tb^{3+} emission at 545 nm. Upon the addition of serotonin, the fluorescence emission of Tb^{3+} decreased, while the blue fluorescence emission recovered.

3.2.2.6 D-MOFs originating from dual ligands. As discussed above, lanthanide ions are commonly employed to construct D-MOFs. However, their application is hindered by their high price and toxicity. Mixed fluorescence ligands are favourable for the simple construction of D-MOFs. There is a high requirement for ligands with certain features. Specifically, ligands should have a similar size to form D-MOFs with a stable structure, and the emission of the fluorescence ligands should be excited under a single wavelength and display a large wavelength difference. For example, Wen's group prepared D-MOFs using 2-aminoterephthalic acid (BDC-NH_2) with maximum emissions at 434 and 2,5-dihydroxylterephthalic acid [BDC-$(OH)_2$] with maximum emissions at 543 nm as ligands, and Zn^{2+} as the metal centre for the detection of HCHO and Fe^{3+} ions.[231] Zn^{2+} was employed because its full electronic structure is not conducive to energy transfer from the ligand to Zn^{2+}, and thus the luminescence of the ligands could be maintained. The addition of HCHO or Fe^{3+} ions induced a decrease in the blue emission and increase in the yellow emission. For the detection of HCHO, the Schiff base reaction between the –NH_2 group and HCHO resulted in energy transfer between BDC-NH_2 and BDC-$(OH)_2$. For the detection of Fe^{3+}, the IFE and electrons transfer from the electron-rich –NH_2 group to Fe^{3+} ions resulted in the quenching of the blue emission.

Among the abovementioned D-MOFs, guest-encapsulated Ln-MOFs are limited by the leakage of the guest, dual-ligand D-MOFs are limited by the selection of dual ligands, and dual-Ln ion D-MOFs suffer from poor anti-interference ability because of the similar properties of lanthanide ions. Also, mixed Ln-MOF systems may exhibit the issue of low mixing uniformity. Considering the preparation process, single-ligand, single-Ln^{3+}-based D-MOFs are the simplest type. However, the design and screening of eligible ligands are vital.

3.2.3 Dual-emission QDs (D-QDs). The photophysical properties QDs can be tailored by controlling their size, composition, and surface modification. To date, the most commonly used methods for the preparation D-QDs are doping Mn^{2+}, formation of a core–shell structure, and surface modification.

3.2.3.1 D-QDs with Mn^{2+} doping. D-QDs can be prepared by doping Mn^{2+} ions in wide band gap ZnS (or ZnSe) QDs, which display intrinsic dual-emitting property, where one is high-energy exciton emission and the other is low-energy Mn^{2+}-doped emission. The first Mn^{2+}-doped D-QD-based DRFP was reported by Gamelin and co-workers in 2010,[235] and since then, Mn^{2+}-doped D-QDs attracted widespread attention.[236,237] For example, Xia's group developed dual-emitting ZnS: Mn^{2+} QD-based fluorescence sensors for the detection of glucose and H_2O_2 based on electron transfer and chemical reactions, respectively.[236] The ZnS: Mn^{2+} QDs displayed the host ZnS emission at 425 nm and the doped Mn^{2+} emission at 600 nm. As shown in Fig. 14A, negatively charged QDs were first mixed with positively charged boracic acid-substituted methyl viologen (BBV) to form a QD–BBV electron-transfer complex. The LUMO energy level of BBV is more matched with Mn $^4T_1$ than that of the ZnS conduction band. After the formation of the QD–BBV electron-transfer complex, the Mn^{2+} emission at 600 nm was quenched, while the host emission of ZnS at
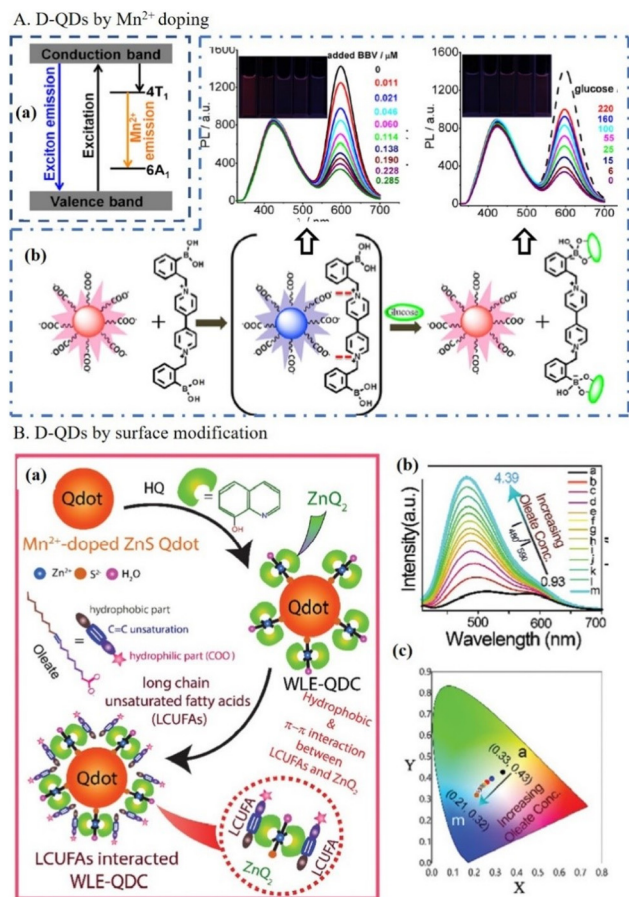
View Article Online

Fig. 14 (A) D-QDs prepared by Mn^{2+} doping. (a) The energy diagram of host (blue arrow) and Mn^{2+} emission (orange arrow). (b) Proposed mechanisms for the formation of the QD-BBV complex and the disorganization of the formed complex by the competitive effect of glucose. (a and b) Reproduced with permission from ref. 236. Copyright 2016, the American Chemical Society. (B) D-QDs formed by surface modification with inorganic complex. (a) A schematic illustration of the fabrication of QDCs by the reaction between QD and HQ and the proposed mechanism of recognition and ratiometric visual sensing of LCUFAs. (b) The representative emission spectra and (c) corresponding color chromaticity coordinates of QDC recorded following the addition of different concentrations of LCUFA. (a–c) Reproduced with permission from ref. 241. Copyright 2021, The Royal Society of Chemistry.

425 nm remained almost invariable. Glucose can react with boronic acid to form tetrahedral anionic glucuronate esters and neutralizes the charge of BBV. Thus, when glucose was further added to the QD-BBV complex, it disassembled, and the quenched Mn^{2+} emission recovered gradually. The fluorescence color change from blue to purple to red could be observed by the naked eye. The ZnS: Mn^{2+} QDs also were employed for the detection of H_2O_2 based on oxidation reactions. The oxidation of S atoms on the QD surface resulted in the quenching of the host ZnS emission, and the oxidation of Mn^{2+} to Mn^{3+} resulted in the quenching of the Mn^{2+} emission. The oxidation reaction starts from the QD surface, and the inner Mn^{2+} are less impacted by oxidation, and thus the addition of H_2O_2 induced the quenching of the two emissions

with different sensitivity. Therefore, ZnS: Mn^{2+} QDs can be employed to detect H_2O_2 and its related chemical reactions.

3.2.3.2 D-QDs by surface modification. Modifying the surface of QDs with organic molecules can generate a new emission from their surface, in addition to the original emission from the excitonic core.[238] The formed nanocomposite, which is called a quantum dot complex (QDC), can be employed for the ratiometric sensing of organic pollutants,[239] metal ions,[240] unsaturated fatty acids,[241] water in oil,[242] dopamine,[243] and phosphate.[244] For example, Chattopadhyay's group modified 8-hydroxyquinoline (HQ) on the surface of Mn^{2+}-doped ZnS QDs for the ratiometric detection of unsaturated fatty acids in vegetable oils,[241] as shown in Fig. 14B. The QDC generated a new green emission at 512 nm from the formed ZnQ_2 complex in addition to the original orange emission at 590 nm from Mn^{2+}-doped ZnS QDs. The addition of oleate led to a significant fluorescence enhancement at 480 nm, which shifted from the emission of ZnQ_2 at 512 nm, and a slight fluorescence enhancement at 590 nm. The liner range for the quantitative analysis of oleate using the emission intensity ratio (I_{480}/I_{590}) was 4.2–16.6 mM, and a luminescence color change from white to cyan could be observed. Xiao's group modified dimethyl aminoterephthalate on the surface of $CsPbBr_3$ PQDs to prepare $CsPbBr_3$@DMT-NH_2 QDs for the detection of water in oil.[242] The $CsPbBr_3$@DMT-NH_2 QDs displayed weak blue emission at 445 nm from the DMT-NH_2 ligand and green strong emission at 530 nm from the QDs. After exposure to water, the green fluorescence of $CsPbBr_3$ was quenched due to the fact that water can disintegrate the QDs to their colorless precursors. The blue fluorescence of DMT-NH_2 was enhanced due to the protonation of DMT-NH_2 by water.

3.2.4 Other dual-emission FNPs. In addition to the commonly used D-CDs, D-MOFs and D-QDs, other dual-emission FNPs, such as dual-emission Si NPs,[245] dual-emission Cu NCs,[246] dual-emission UCNPs,[247,248] and dual-emission Au NCs,[249] have also been prepared by adjusting the solvents, ligand, and components and used for the detection of Cu^{2+}, GSH, histamine, furfural, and ALP. Dual-emission fluorescent nanohybrids, such as AuNC-PbS-QD complex,[250] AuNC-CD complex,[251,252] and QD-CuNC complex[253] were also prepared *via* the co-template method, seed growth method, and *in situ* growth method. For example, Zhao *et al.*[250] proposed a protein-directed co-template strategy to synthesize dual-emission AuNCs-PbS-QDs based on the fact that bovine serum albumin (BSA) was a bio-template for the preparation of QDs and AuNCs simultaneously. Firstly, the BSA-templated AuNCs were synthesized, which were further used as a template for the synthesis of PbS QDs. The protein-directed co-template synthesis method avoids the tedious chemical coupling and modification steps and simplifies the preparation process. Liu's group prepared an Au NC-CD nanohybrid *via* the seed growth method.[251] Firstly, the seed of Au clusters was prepared using GSH as the reducing agent, then the solution of gold seeds was mixed with glucose, and CD-Au NC was synthesized *via* the microwave-assisted method. The dispersed Au clusters in the carbon skeleton displayed the properties of Au NCs,

where CD-Au NC displayed dual-emission property under single excitation.

3.3 Target-induced new fluorescence emission

The above-discussed two types of DRFPs display two fluorescence emissions in the absence of target. Alternatively, DRFPs can be construed based on target-induced new emissions. The appearance of the new emission may be due to the target-sensitized lanthanide ions, coordination-induced new emission, *in situ* growth of FNPs, *etc.*

3.3.1 Sensitized new emission. As discussed above, the luminescence of lanthanide ions can be sensitized by the "antenna effect".[254–256] Fluorescence nanohybrids including lanthanide ions can be employed for the detection of sensitizers, such as TC and DPA. This type of target-sensitized new fluorescence emission was discussed in section 3.1.5[105–116] and section 3.2.2,[212–217] and thus not emphasized in this part.

3.3.2 Coordination-induced new emission. Based on the fact that strong fluorescent complexes can be formed when metal ions are coordinated with non-fluorescent or weak fluorescent organic molecules, DRFPs can be designed based on the formation of new emissions when the organic target coordinates with metal ions in FNPs. For example, Zhang's group employed single-emission copper-doped ZnS QDs (ZnS: Cu QDs) to detect TC in milk.[257] Upon the addition of TC, the original fluorescence of the ZnS: Cu QDs at 578 nm was quenched, while a new green fluorescence emission at 520 nm stemming from TCs-Zn(bix) ternary complexes appeared. Using this new green emission, TC could be distinguished from other types of antibiotics. Similarly, based on the sensitization effect of Zn^{2+} to TC, CdTe QDs@ZIF-8,[258] CDs@ZIF-8,[259] and Ru@ZIF-8[260] were prepared for the detection of TCs. In addition to Zn^{2+}, Ca^{2+} can also coordinate with TCs to produce a new emission from TCs.[261,262] As shown in Fig. 15A, Jiang's groups chelated Ca^{2+} on the surface of CdTe QDs for the detection of OTC, in which the red-emitting CdTe QDs served as the reference and Ca^{2+} as the specific recognition unit and receptor.[261] The addition of OTC led to a new green emission at 511 nm from the coordination complex of Ca^{2+}-OTC.

Based on the fact that β-CD could significantly enhance the fluorescence of aflatoxin B1(AFB1) by encapsulating AFB1 into the host of β-CD and Pt^{2+} could further enhance the fluorescence of AFB1 by the formation of a coordination complex, β-CD@Cu NPs with single emission at 650 nm were prepared by chemically bonding fluorescent Cu NPs with SH-β-CD for the detection of AFB1.[263] With the addition of AFB1 and Pt^{2+}, a new blue fluorescence emission at 433 nm originating from AFB1 appeared due to the β-CD–AFB1 host–guest interaction and the complexation of AFB1 and Pt^{2+}. Meanwhile, the red fluorescence emission of Cu NPs was quenched based on IFE between AFB1 and Cu NPs.

3.3.3 Hydrogen bonding-induced new emission. The hydrogen bonding formed between the target and FNPs also induces new fluorescence emissions.[264–266] For example, the addition of ClO^- to UiO-66-NH$_2$ (Zr-NH$_2$-H$_2$BDC) induced a decrease in the original blue emission of UiO-66-NH$_2$, while a

new emission at 533 nm appeared and increased with an increase in the amount of ClO^-.[264] The new emission was attributed to the hydrogen bonding between the O atoms in ClO^- and the H atoms in $-NH_2$. The turn-off effect of UiO-66-NH$_2$ is ascribed to the formation of hydrogen bonding and energy transfer to ClO^-. In another example, Wu's group used the single emission of b-CDs for the ratiometric detection of water in organic solvents.[265] As shown in Fig. 15B, b-CDs prepared using 2,5-dihydroxyterephthalic acid as the precursor in absolute ethanol solution contained abundant carboxyl and hydroxyl groups and displayed blue emission centre at 467 nm when excited at 320 nm. Interestingly, the emission of the CDs shifted from 461 to 525 nm when the solution changed from ethanol to water, accompanied by changes in the fluorescence color from blue to green. Then, the CDs were employed to detect water in ethanol. When the content of water increased from 0–25% in ethanol solution, the fluorescence intensity at 467 nm gradually weakened, while a new emission emerged at 525 nm and was enhanced. The ratio of $I_{525\ nm}/I_{467\ nm}$ exhibited an excellent linear relationship against the water content ranging from 0.2% to 6%. The detection mechanism was based on the formation of intermolecular hydrogen bonding between water and the hydroxyl groups in b-CDs, and the original intramolecular hydrogen bonding of the CDs was broken, resulting in a redshift in the fluorescence emission.

3.3.4 New emission originating from chemical reactions. Based on some specific chemical reactions, such as enzyme catalyzed reaction and oxidization-regulated reaction, some non-fluorescent substrates can be efficiently converted into fluorescent substances. As shown in Fig. 16, non-fluorescence 4-methylumbelliferyl-β-glucuronide (MUG) can be hydrolyzed by β-glucuronidase (GCU) to produce blue emissive 4-methylumbelliferyl (4-MU),[267,268] *o*-PD can be oxidized to produce yellow-emission DPA,[269–272] dopamine (DA) reacts with resorcinol to produce catecholamines with strong blue emission,[273] terephthalic acid (TA) is oxidized with H_2O_2 to produce fluorescence oxTA,[274] and nicotinamide adenine dinucleotide (NAD^+) can be reduced to blue-emissive nicotinamide adenine dinucleotide (NADH) by the isopropanol-catalysed enzymatic reaction of secondary alcohol dehydrogenase (S-ADH).[275] DRFPs can be designed by further combining fluorescence turn-on sensors with some FNPs. For example, Xiao's group mixed MUG with the red emission Eu^{3+}@MOF-253 for the detection of GCU.[267] With the addition of GCU, MUG was hydrolyzed to produce 4-MU, which could further quench the red emission of Eu^{3+} by IFE. Thus, the addition of GCU induced an increase in the blue emission and quenched the red emission. In should be noted that Eu^{3+}@MOF-253 acted as a fluorescence signal and improved the enzymatic reaction efficiency of the dual roles in this design. Similarly, Wang's group mixed 4-methylumbelliferyl phosphate (4-MUP) with Ce^{3+}-modified red emission ZnCdSe/ZnS QDs for the detection of reactive oxygen species (ROS).[268] After the addition of ROS, such as H_2O_2, $ONOO^-$, and ClO^-, the Ce^{3+} on the surface of the QDs was oxidized to Ce^{4+} with phosphatase-like catalytic activity, which catalyzed the hydrolysis of 4-MUP to generate
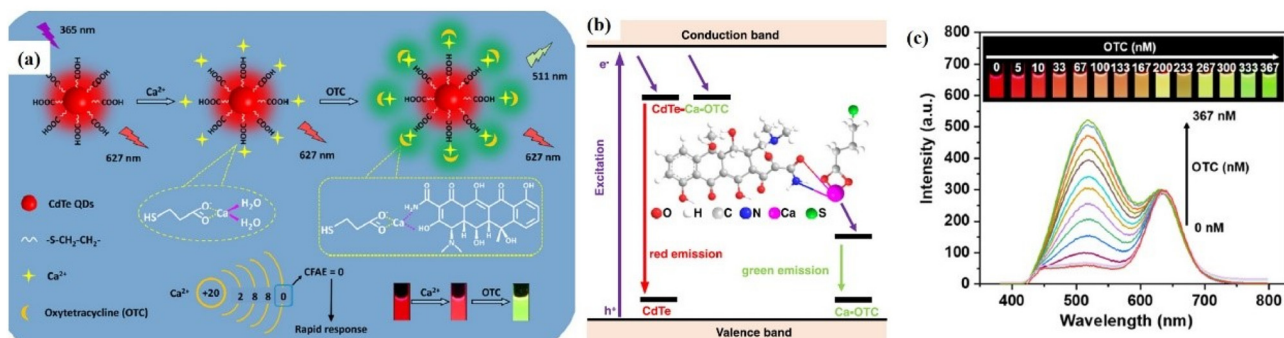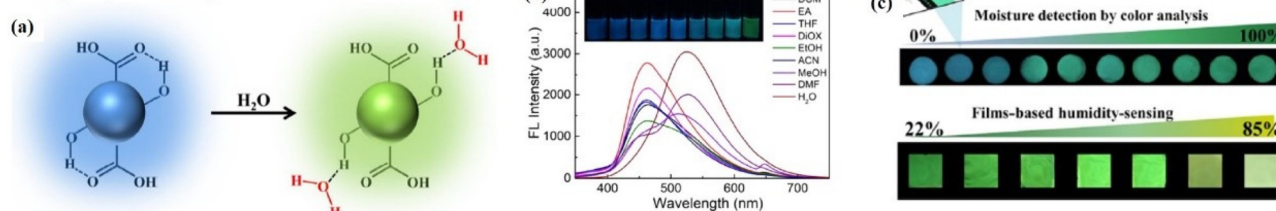
Fig. 15 (A) An example of coordination-induced new emission. (a) An illustration of the CdTe QDs@Ca^{2+} complex for fluorescent ratiometric sensing of OTC. (b) Schematic representation of the emission levels of Ca/CdTe QDs and the energy transfer from OTC to Ca^{2+}. (c) The fluorescence spectra of CdTe QDs@Ca^{2+} upon the exposure to different concentrations of OTC. The inset shows the corresponding fluorescence color photos under 365 nm UV irradiation. (a–c) Reproduced with permission from ref. 261. Copyright 2023, Elsevier. (B) An example of hydrogen bonding-induced new emission. (a) The water sensing mechanism of CDs, (b) fluorescence spectra of CDs in different solvents and (c) fluorescence images of the color change based on CD-loaded paper strips and films under a 365 nm UV lamp. (a–c) Reproduced with permission from ref. 265. Copyright 2021, the American Chemical Society.

4-MU. During the detection process, the red fluorescence emission of the QDs was slightly affected. Thus, the Ce^{3+}/QD/4-MUP system was used for the ratiometric sensing of ROS with good sensitivity.

Based on the fact that *o*-PD can be oxidized to yellow-emissive DPA, mixing *o*-PD with some FNPs can be employed for the detection of some ROS, such as H$_2$O$_2$ [269–271] and ClO.[27] For example, He's group constructed a cellulose nanocrystal (CNC)-stabilized AuNC and OPD system for the detection of ROS. CNCs were used as the carrier to grow AuNCs using L-Dopa as the reducing agent to prevent the aggregation of AuNCs and promote their stability. The positively charged *o*-PD was absorbed on the surface of the negatively charged CNC@AuNCs by electrostatic interaction to form DRFP. The addition of ROS, such as ClO$^-$, ONOO$^-$, and ˙OH, could oxidize *o*-PD to form DAP with yellow fluorescence. Thus, with addition of ROS, the fluorescence emission of AuNCs at 488 nm gradually decreased because of the strong oxidization, whereas that of DAP at 580 nm gradually increased. Meanwhile, the fluorescence of the probe changed from blue to yellow.

As shown in Fig. 17A, a Cu@Eu–BTC MOF and resorcinol nanosystem was constructed for the detection of DA.[273] Without DA, the system only displayed the characteristic red fluorescence of Eu^{3+} stemming from the Cu@Eu–BTC MOF. With addition of DA, DA reacted with resorcinol to produce catecholamines with strong blue emission, while the red emis-

sion of MOF remained stable as the internal standard. It should be noted that in addition to being used as a fluorescent internal standard, the Cu@Eu–BTC MOF also acted as a nanoreactor to promote the DA-resorcinol reaction and improve the detection sensitivity. As shown in Fig. 17B, Chen's group synthesized Ce-BDC MOFs through the coordination of Ce^{3+} with TA for the detection and elimination of ˙OH.[274] ˙OH could oxidize TA to produce 2-hydroxyterephthalic acid, leading to the appearance of blue emission at 440 nm. During the detection process, the fluorescent emission of Ce^{3+} at 355 nm served as the reference. This sensor could also be employed for the elimination of ˙OH based on the conversion of Ce^{3+} and Ce^{4+} and the constant amount of Ce^{3+} and Ce^{4+} in Ce-BDC MOFs.

3.3.5 Target-induced *in situ* formation of new FNPs. The target-induced formation of new FNPs can introduce new fluorescence emissions to form DRFPs. For example, an H$_2$S-activated DCNP@HSA-Ag$^+$ nanoprobe was reported by Song's group by the *in situ* formation of Ag$_2$S QDs.[276] The nanoprobe was prepared by first modifying human serum albumin (HSA) on the surface of DCNP (DCNP, NaYF$_4$: 20% Yb, 2% Er@NaYF4) by the coordination of carboxyl groups with Y^{3+} of DCNP, and then modifying Ag$^+$ on HSA through coordination with carboxyl groups. In the presence of H$_2$S, Ag$_2$S QDs were formed through the H$_2$S-induced chemical reaction between H$_2$S and Ag$^+$. The FL signal of DCNP was stable and the FL signal of Ag$_2$S QDs was H$_2$S concentration dependent.
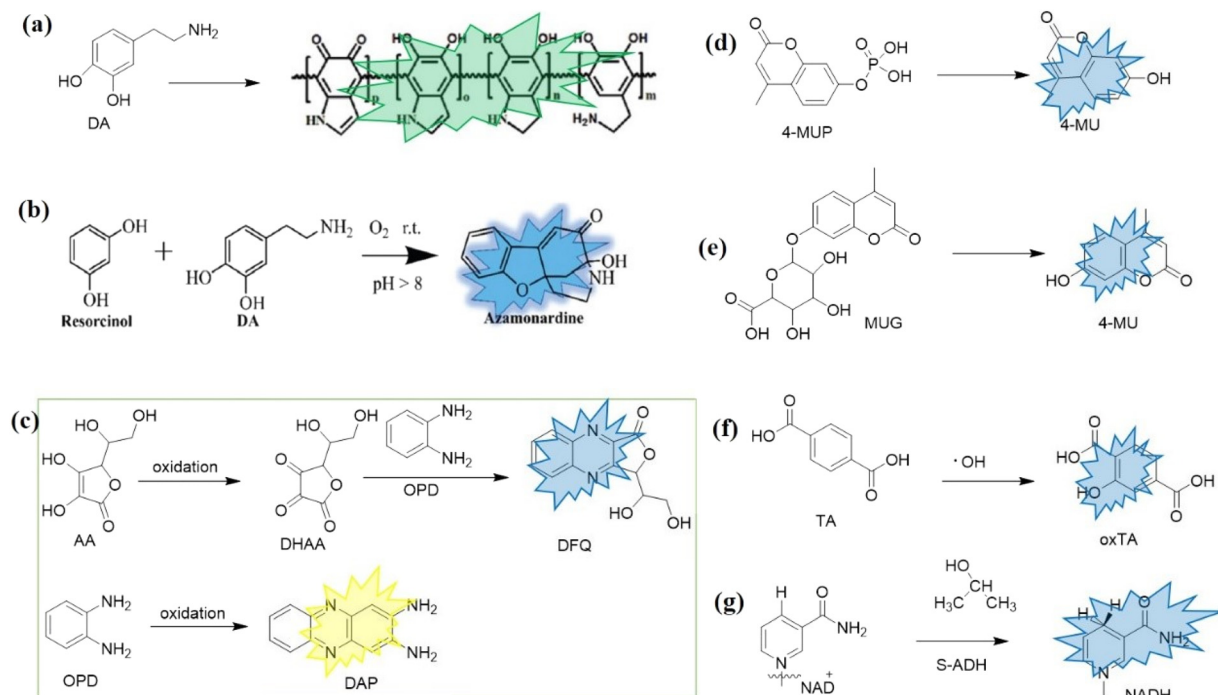
Fig. 16 Commonly used chemical reactions to construct DRFP. (a) DA can be oxidized to PDA NPs with green emission. (b) DA reacts with resorcinol to produce catecholamines with strong blue emission and (c) OPD can be oxidized to produce yellow emission DPA and AA can be oxidized to dehydro-L-ascorbic acid (DHAA). DHAA in turn reacts with o-PD to form a highly blue fluorescent quinoxaline derivative 3-(1,2-dihydroxyethyl) furo [3,4-b] quinoxaline-(3H)-one (DFQ) with a fluorescence emission peak at around 430 nm. (d) 4-Methylumbelliferyl phosphate (4-MUP) can be transformed into 4-MU with blue emission using phosphatase-like enzyme, (e) non-fluorescence 4-methylumbelliferyl-β-glucuronide (MUG) can be hydrolyzed by β-glucuronidase (GCU) to produce 4-methylumbelliferyl (4-MU) with blue emission, (f) terephthalic acid (TA) is oxidized with H_2O_2 to produce fluorescent oxTA, and (g) isopropanol can convert nicotinamide adenine dinucleotide (NAD^+) into reduced nicotinamide adenine dinucleotide (NADH) with blue emission through the enzymatic reaction of secondary alcohol dehydrogenase (S-ADH).
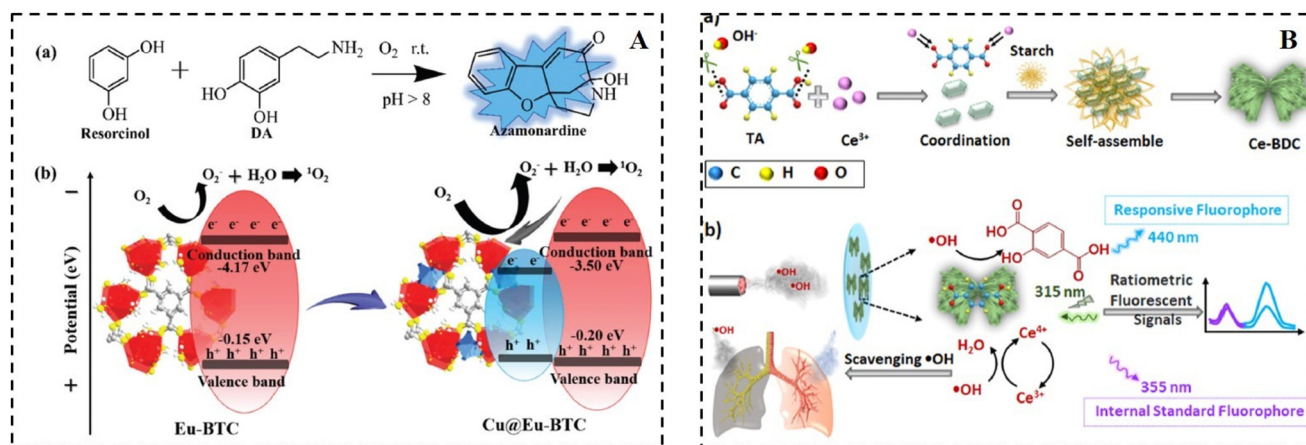
Fig. 17 (A) Cu@Eu−BTC MOF and resorcinol nanosystem for the detection of DA. (a) The specific turn-on fluorescence reaction of DA and resorcinol and (b) a schematic diagram of the specific DA catalytic detection mechanism assisted by MOFs. (a and b) Reproduced with permission from ref. 273. Copyright 2021, the Royal Society of Chemistry. (B) (a) A schematic illustration of the synthesis of Ce-BDC MOFs. (b) ˙OH detection and elimination mechanism based on Ce-BDC MOFs in gas from fuel combustion. (a and b) Reproduced with permission from ref. 274. Copyright 2022, Elsevier.

In another example, Tang's group proposed a method for the discriminative detection of glutathione (GSH) from cysteine (Cys) based on the GSH-induced *in situ* formation of

CuNCs on the surface of UiO-66-NH$_2$.[277] As shown in Fig. 18A, UiO-66-NH$_2$ was prepared using 2-aminoterephthalic acid (BDC-NH$_2$) and ZrCl$_4$, displaying weak blue emission at

A New emission from the target induced in situ formation of new FNPs
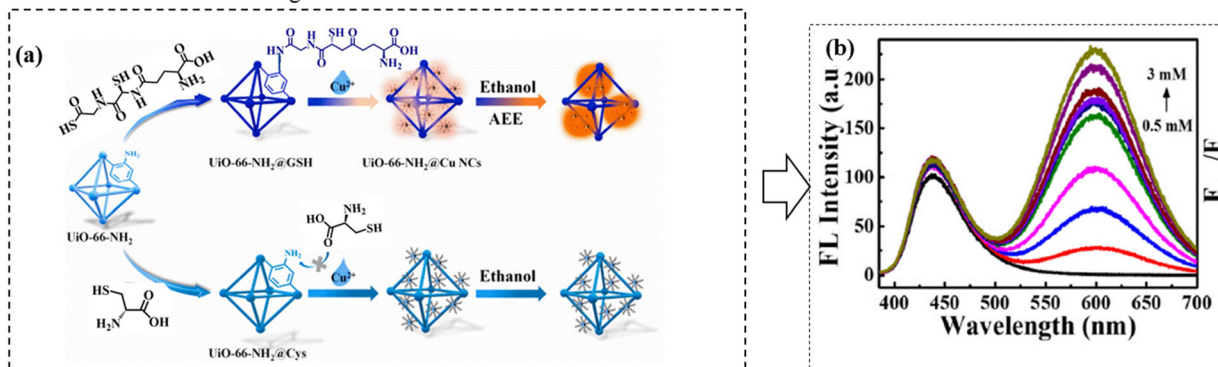
B New emission from decomposition of origin FNPs and formation of new FNPs

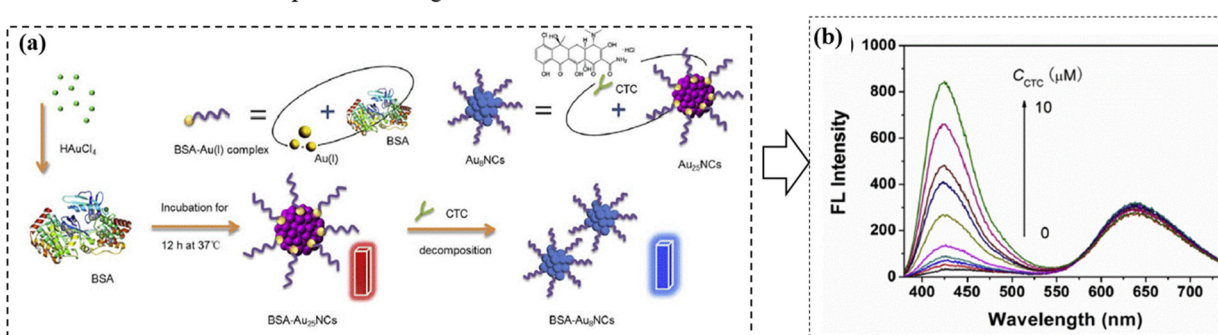**Fig. 18** (A) New emission from the target-induced *in situ* formation of CuNCs. (a) A scheme for the detection of GSH from Cys based on the *in situ* formation of CuNCs on the surface of UiO-66-NH$_2$ and (b) the FL spectra with the addition of GSH. Reproduced with permission from ref. 277. Copyright 2022, Elsevier. (B) New emission from the decomposition of the original Au$_{25}$ NCs and formation of Au$_8$NCs. (a) A schematic illustration of the synthesis of dual-emission BSA-AuNCs and the ratiometric detection of CTC. (b) The fluorescence emission spectra of BSA-AuNCs upon the addition of different concentrations of CTC. Reproduced with permission from ref. 278. Copyright 2023, Elsevier.

450 nm from the BDC-NH$_2$ ligand. GSH is a commonly used protecting ligand for synthesizing Cu NCs with orange or red emissions and aggregation-enhanced emission (AEE) properties. Then, with the addition of GSH and Cu^{2+}, Cu NCs were fabricated and the emitted AEE featured the orange-red fluorescence of Cu NCs at 600 nm when injected into ethanol. However, no emission of Cu NCs was detected upon the addition of Cu^{2+} to a solution of UiO-66-NH$_2$@Cys. Using the unique Cu NC emission, GSH and Cys could be discriminated. Based on the fluorescence intensity ratio of blue to orange-red, DRFP was developed for the detection of GSH in the linear range of 0.5–1.75 mM and LOD of 0.14 mM.

In some cases, the target-induced decomposition of the original FNPs and formation of new FNPs can result in the generation new emissions. For example, Wu's group employed Au$_{25}$NCs consisting of 25 gold atoms for the detection of chlortetracycline through a ratiometric approach.[278] As shown in Fig. 18B, Au$_{25}$NCs were prepared using BSA as a stabilizer, showing a red emission at 640 nm. In the presence of CTC, a new blue emission at 425 nm emerged and the original red emission at 640 nm decreased. This phenomenon is related to the conversion of Au$_{25}$NCs to Au$_8$NCs stemming from the secondary structure changes of BSA. CTC has both halogen and carbonyl groups in its aromatic ring, making the aryl carbon bonded to the halogen susceptible to react with the amino

aside residues in BSA. The reaction with CIC changed the secondary structure of BSA, and induced the decomposition of Au$_{25}$NCs to Au$_8$NCs. It should be noted that this sensor could discriminative detection of CTC from other TCs.

3.3.6 Aggregation- and dispersion-induced new emission. Some FNPs display AIE property, while some FNPs display ACQ property. The target induces the aggregation or change in the dispersion state of FNPs, resulting in a new emission.[279–281] For example, Paydar *et al.* prepared GSH-modified CDs for the detection of Pb^{2+} based on AIE.[280] Firstly, CDs were prepared *via* the pyrolysis of *m*-aminophenol in the presence of dimethylformamide and phosphoric acid. Then, GSH with high binding affinity for Pb^{2+} ions was modified on the surface of the CDs. Upon the addition of Pb^{2+}, the chemical binding of GSH ligands with Pb^{2+} ions led to the aggregation of the GSH-modified G-CDs, which resulted in the quenching of the original green emission at 522 nm, while a new well-separated emission emerged at 692 nm. The surface modification with GSH formed new emitting centers on the surface of the CDs. However, the new emission was suppressed through a PET process from the sulfur lone pair electrons of GSH. In the presence of Pb^{2+}, chemical binding between the sulfide groups of GSH and Pb^{2+} caused the CDs to aggregate, which stopped the PET process, and subsequently generated a new emission. The ratio of FL intensity (I_{692}/I_{522}) showed a linear relationship

with Pb^{2+} ranging from 10 to 700 nM with an LOD as low as 2.7 nM.

In addition to the target-induced aggregation or dispersion of FNPs inducing a new emission, the aggregation of the target will also induce a new emission. For example, based on the phenomenon that the aggregation of TC induces a new green emission, several MOF-based fluorescence sensors were designed.[282–284] Zhao's group embedded red-emitting Ru $(bpy)_3^{2+}$ into ZIF-8 for the detection of TC based on the aggregation of TCs in MOFs.[260] ZIF-8 was employed because it can interact with the molecules that enter its framework to cause the aggregation of these molecules. When TCs were added to the Ru@ZIF-8 system, the original red emission remained stable, while a new green emission was generated at 505 nm. TC has a p-conjugated six-membered ring structure and abundant N, O, and H atoms, and thus the TC molecules aggregated through π–π interactions, resulting in new peaks for TC.

3.3.7 FRET based on new emission. When FRET exists between FNPs and the target, the original FL is weakened, while a new emission from the target appears and increases with an increase in the concentration of the target.[285,286] For example, 11-mercaptoundecanoic acid (MUA)-modified CDs were used to detect DOX based on FRET-induced new emission.[285] Because the absorption spectrum of DOX overlapped well with the fluorescence emission spectrum of the CDs, when DOX was added to the solution of CDs, a new fluorescence emission appeared at 590 nm, accompanied by a decrease in the original green emission of CDs. The decrease in the fluorescence lifetime confirmed the existence of FRET between the CDs and DOX.

3.4 DRFP with auxiliary nanomaterials

In the above-discussed three types of DRFPs, the target directly interacts with the fluorescence signal to induce a change in fluorescence intensity. Even in the on–off–on mode, the primary target directly interacts with FNPs. Alternatively, DRFPs can be constructed by non-fluorescence auxiliary nanomaterials. Generally, the addition of auxiliary nanomaterials, such as AuNPs, Ag NPs, and MnO_2 nanosheets causes a FL change based on IFE or chemical reaction. With the addition of the target, it directly induces the aggregation, etching or decomposition of the auxiliary nanomaterials, subsequently inducing a change in the FL.

3.4.1 Auxiliary nanomaterials with IFE. On the one hand, the absorption spectrum of nanomaterials overlaps well with many FNPs, and thus the FNPs can be quenched by nanomaterials. On the other hand, the absorption spectra of nanomaterials can be changed by target-induced aggregation or etching. Thus, based on the IFE of nanomaterials, many DRFPs can be constructed. It is well known that AuNPs in their dispersion state display wine red color, while aggregated AuNPs display blue color. Thus, many colorimetric analysis methods have been constructed based on the target-induced aggregation of AuNPs. Compared with colorimetric analysis, fluorescence analysis displays higher sensitivity. Thus, colorimetric analysis can be converted into fluorescence sensors by

employing AuNPs and IFE-related FNPs. For example, our group constructed a DRFP based on the IFE between AuNPs and FNPs for the detection of TNT, as shown in Fig. 19A.[287] Firstly, g-CDs and red emissive CdTe QDs were embedded in SiO_2 NPs as a fluorophore pair. Based on the facts that (1) g-CDs can be quenched by dispersed AuNPs based on IFE, (2) TNT can induce the aggregation of AuNPs, and (3) red QDs can be quenched by aggregated AuNPs based IFE, a DRFP for the detection of TNT was constructed by mixing fluorescence silica spheres and AuNPs. It should be noted that this strategy displays wide applicability. Molecules that can cause the aggregation of AuNPs can be detected using this method. Since then, based on the target-induced aggregation of AuNPs, many DRFPs have been constructed for the detection of UO_2^{2+} (ref. 288) and pesticides.[289–291]

Ag NPs have also been employed as auxiliary NPs to construct DRFPs based on IFE. Based on the fact that Ag NPs can be etched to silver ions, and Ag NPs with the maximum absorbance band at 400 nm can quench FNPs with blue emission by IFE or FRET, fluorescence sensors were constructed for the detection of H_2O_2 [292] or glucose.[293] Similar to Ag NPs, silver nanoprisms (Ag NPRs) with the maximum absorbance band at 650 nm can also be employed to construct IFE-based DRFPs.[294] As shown in Fig. 19B, our group constructed a DRFP for the detection of H_2O_2 with the assistance of Ag NPRs.[294] Firstly, red CdTe QDs were embedded in SiO_2 NPs and b-CDs covalently linked on the surface of SiO_2 NPs to form r-QDs@SiO_2@b-CDs. mixed Ag NPRs were mixed with r-QDs@SiO_2@b-CDs, the red CdTe QDs could be quenched by Ag NPRs *via* IFE. With the addition of H_2O_2, Ag NPRs were etched to Ag^+ and weakened the IFE, and thus the fluorescence of the CdTe QDs recovered. Meanwhile, b-CDs were quenched by Ag^+ *via* charge transfer. Compared with the AuNP-assisted DRFPs, the detection target in the AgNP-auxiliary DRFPs was generally limited to H_2O_2 and H_2O_2-related substances, such as glucose and lactate.

The broad absorption spectrum of 2D MnO_2 nanosheets endow them with strong fluorescence quenching ability. MnO_2 NSs can be rapidly degraded to Mn^{2+} by some reducing agents, leading to their decomposition. Therefore, MnO_2 NSs have been used as auxiliary NPs to detect reducing substances, such as AA and GSH, using FNPs such as CDs, QDs, and even fluorescent dyes to form donor–acceptor pairs.[295] Based on the fluorescence quenching ability of MnO_2 NSs, many DRPFs have been designed.[296–299] Chen's group designed an Au/Ag NCs-MnO_2-VB1 (VB1 stands for thiamine) ternary system for the detection of proanthocyanidins.[297] In the absence of the target, the emission of Au/Ag NCs at 650 nm was quenched by the MnO_2 NSs based on FERT, and VB1 was oxidized by the MnO_2 NSs to produce oxVB1 with highly blue fluorescence emission at 450 nm. In the presence of proanthocyanidins, MnO_2 was reduced to Mn^{2+}, which caused its quenching capacity and oxidase-like activity to disappear, and thus the blue emission was reduced and the red fluorescence of Au/AgNCs recovered. Proanthocyanidins could be monitored by the DRFP with a linear range of 0.27–22.4 Mm and corres-

A DRFP based on the target induced aggregation of AuNPs.
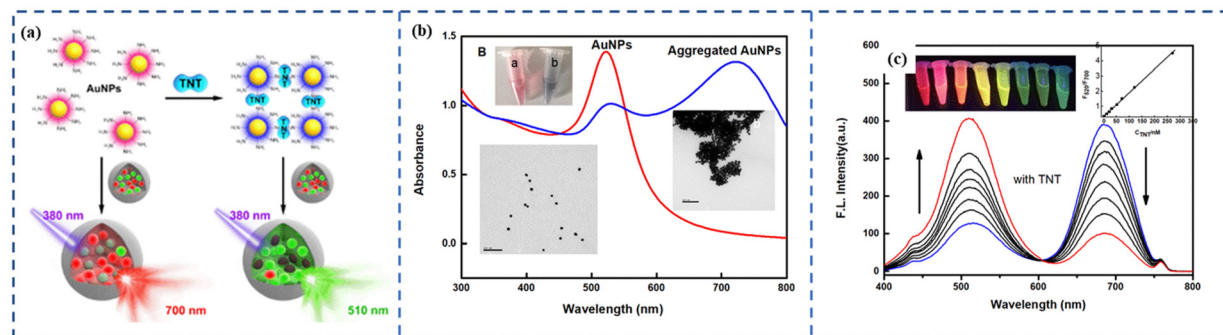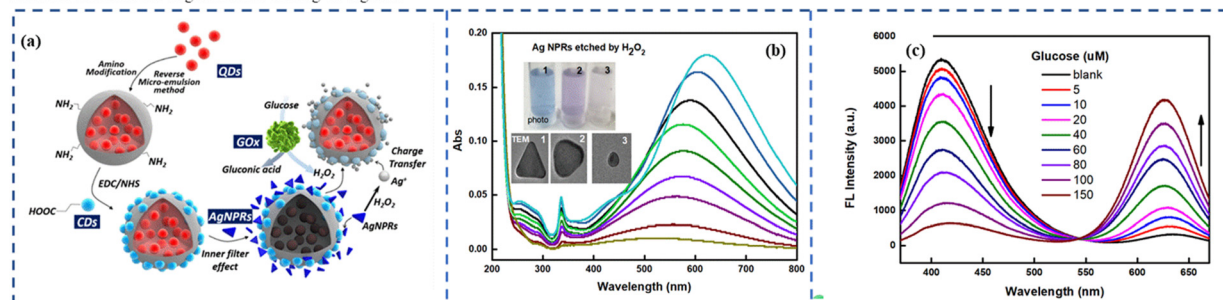
B DRFP based on the target induced etching of Ag NPs

Fig. 19 (A) DRFP constructed based on the IFE of AuNPs. (a) An illustration of the DRFP for the detection of TNT through the IFE of AuNPs and target-induced aggregation of AuNPs. (b) The UV−vis spectra of AuNPs without (red line) or with (blue line) the addition of 5 nM TNT. The insets are photographs of Au NPs under sunlight and TEM images of AuNPs without or with the addition of 1 μM TNT. (c) The fluorescence spectra of RFNs upon the addition of different concentrations of TNT ranging from 0.1 to 300 nM. Reproduced with permission from ref. 287. Copyright 2017, the American Chemical Society. (B) DRFP constructed based on the IFE of Ag NPRs. (a) Illustration of the DRFP for detection of H_2O_2 and glucose through the IFE of Ag NPRs and target-induced etching of Ag NPRs. (b) UV-vis spectra of Ag NPRs with the addition of different concentrations of H_2O_2. Inset photos and TEM images are the Ag NPRs with different concentrations of H_2O_2. (c) The corresponding fluorescence spectra of D-RFPs upon exposure to different concentrations of glucose. Reproduced with permission from ref. 294. Copyright 2018, Elsevier.

ponding LOD of 75.9 nM. Similarly, Au NCs-MnO$_2$-VB1 for AA[298] and curcumin (CUR)-MnO$_2$-Amplex Red (AR) system for GSH[299] were designed based on the quenching capacity and oxidase-like activity of MnO$_2$ NSs.

3.4.2 Auxiliary nanomaterials with enzyme mimicking activity. To date, various nanomaterials, such as noble metal nanoparticles, transition metal oxide-based nanoparticles, MOFs, carbon-based materials, and single-atom materials, have been developed to mimic peroxidase, oxidase, catalase, *etc*. These nanozymes can catalyze the oxidation of non-fluorescent substrates to produce fluorescent substances. Upon the addition of the target, the nanozyme is reduced or decomposed, resulting in the loss of its enzyme activity. Based on the enzyme mimicking activity of nanozymes, many DRFPs have been designed, as shown in Fig. 20. Taking MnO$_2$ NSs as an example, we discuss the strategy for the construction of DRFPs with nanozymes in detail.

MnO$_2$ nanosheets with high peroxidase-, oxidase-, and catalase-like activities, are capable of catalysing some non-fluorescent substrates, such as, *o*-PD, TA, Amplex Red (AR), VB1, and DA to fluorescent DPA, oxTA, ox AR, oxVB1 and PDA, respectively, in the presence of H_2O_2, as shown in Fig. 20. Based on this oxidase-like catalytic property, MnO$_2$ nanosheets have been widely used to construct DRFPs for detection of antioxidants and antioxidant-related species.

In the design of FNP-MnO$_2$-*o*-PD, *o*-PD was oxidized by MnO$_2$ NSs to yellow-emission DPA, and the blue-emission fluorescence signal from CDs, QDs, dyes or NCs was quenched by MnO$_2$ NSs based on IFE or FRET or quenched by DPA by IFE. In the presence of the target, generally, the reducing substances, MnO$_2$ NSs, were reduced to Mn^{2+}, which resulted in the recovery of the blue emission signal and reduction of the yellow emission of DPA. For example, the AgNC-MnO$_2$-*o*-PD system was employed to detect a-glucosidase (a-Glu), which could catalyze 2-*O*-a-D-glucopyranosyl-L-ascorbic acid (AAG) to produce AA.[300] MnO$_2$ NSs oxidized *o*-PD into DAP, which could quench blue-emissive AgNCs through IFE. When AAG as the a-Glu substrate and a-Glu were present, AA was released, and the MnO$_2$ NSs were reduced to Mn^{2+}, losing their oxidase-like property. Thus, the AgNC-MnO$_2$-OPD system was constructed for the detection of a-glucosidase (a-Glu). In another example, Li's group established the MnO$_2$-AuNC@ZIF-8-*o*-PD system for the sensitive monitoring of chlorpyrifos.[301] The AuNCs@ZIF-8 fluorescent composite was first prepared by embedding AuNCs in porous ZIF-8. Then, MnO$_2$ NSs were attached to the surface of AuNCs@ZIF-8. The as-prepared MnO$_2$-AuNCs@ZIF-8 composite played multiple roles, including fluorescence property of AuNCs, protection capacity of ZIF-8 and catalyst property of MnO$_2$. MnO$_2$ oxidized *o*-PD to produce the yellow-emission DAP, which quench AuNCs based on IFE. The acetylcholin-
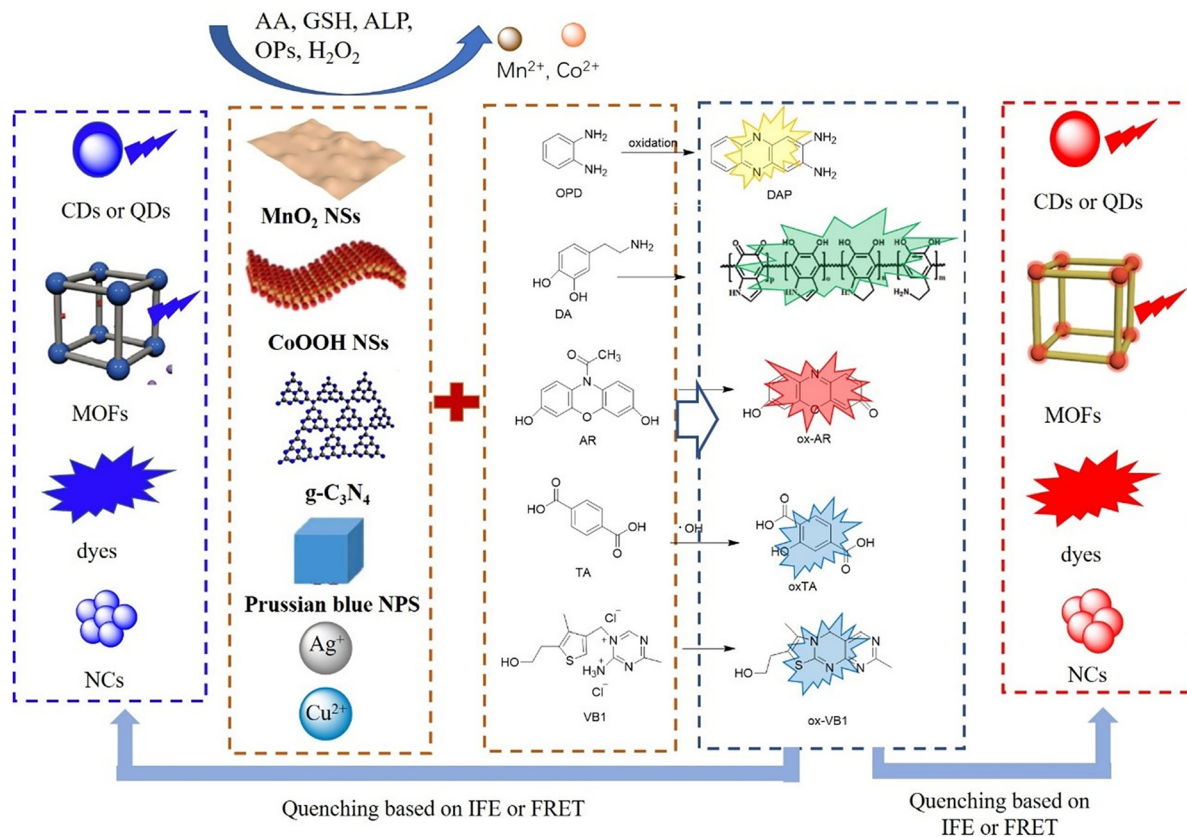
Fig. 20 An illustration of the construction of DRFP based on auxiliary nanomaterials with enzyme mimicking activity.

esterase (AChE) hydrolysis product thiocholine can reduce MnO_2 NSs to Mn^{2+}, and organophosphorus pesticides (OPs) can inhibit the hydrolysis reaction. Based on the cascade catalytic reactions, the MnO_2-AuNC@ZIF-8-o-PD system was employed for the detection of chlorpyrifos with high sensitivity and selectivity. Similarly, the CD-MnO_2-o-PD system for the detection of GSH,[302,303] AuNC-MnO_2-o-PD system for the detection of organophosphorus pesticide,[304] and MnO_2-o-PD-QD system for the detection of AA and ALP[305] have been constructed.

Based on the fact the MnO_2 NSs can oxidize the non-fluorescent VB1 to blue fluorescent oxVB1, oxidize DA to green fluorescent PDA nanoparticles, oxidize non-fluorescent Amplex Red (AR) to red fluorescent oxAR, many DRFP have been constructed. Also, the Pyronin Y-MnO_2-VB1 system for the detection of AA,[306] Cu/Ag NC-MnO_2 nanowire-VB1 system for the detection of GSH,[307] MnO_2-DA-QD system for the detection of ALP,[308] SC-MnO_2-AR system for the detection of GSH,[309] and Ops[310] have been constructed.

Using other nanozymes, such as 2D sheet-like g-C_3N_4,[311] CoOOH nanosheets,[312,313] Prussian blue nanoparticles (PBNPs),[314] and metal ions with oxidation properties, *i.e.*, mainly Cu^{2+} (ref. 315–319) and Ag^+,[320–322] FNP-nanoenzyme-o-PD systems also were construed. For example, CDs-g-C_3N_4-o-PD for the detection of glucose,[311] Si QDs-CoOOH-o-PD for the detection of thiocholine (TCh),[312] CD-Cu^{2+}-o-PD systems for

the direct detection of Cu^{2+}, OPD, H_2O_2,[315] or the inhibitor of catalytic property of Cu^{2+},[316–319] CD-Ag^+-o-PD system for the detection of GSH,[320] and Ag NP/UiO-66-NH_2-o-PD system for the detection of H_2O_2[321] have been reported. An ideal example is that flower-shaped peroxidase mimetic activity and fluorescence property nanohybrid MoOx QDs@Co/Zn-MOF was proposed for H_2O_2 by Feng's group,[322] as shown in Fig. 21. MoOx QDs and Co/Zn-MOFs exhibited peroxidase-like properties, respectively. Loading MoOx QDs on the surface of Co/Zn-MOFs induced synergistic catalytic capabilities. MoOx QDs@Co/Zn-MOFs efficiently catalyzed H_2O_2 to produce ·OH, and then oxidized OPD to DPA. DAP quenched MoOx QDs by FRET. In addition to effectively avoiding the aggregation of the MoOx QDs, the large specific surface area endowed the flower-like Co/Zn-MOFs with higher enzyme-like catalytic capabilities.

The above-mentioned method for the preparation of FNP-nanoenzyme o-OPD ternary systems requires FNPs and nanozymes as the two types of nanomaterials. With the development of nanomaterials with peroxidase mimetic activity and fluorescent property dual functions, FNP-nanoenzyme-o-PD ternary systems can be simplified as nanomaterial-o-PD binary systems. For example, peroxidase mimetic activity and fluorescence property bifunctional Cu-MOF,[323] Fe@PCN-222 MOF,[324] NH_2-MIL-101(Fe) MOF,[325,326] Au–Pt NCs,[327] UiO-66-NH_2@Au,[328] Pd-modified C_3N_4 nanosheets (Pd/C_3N_4),[329] aptamer-modified C_3N_4 nanosheets,[330] Cu-doped CDs (Cu-
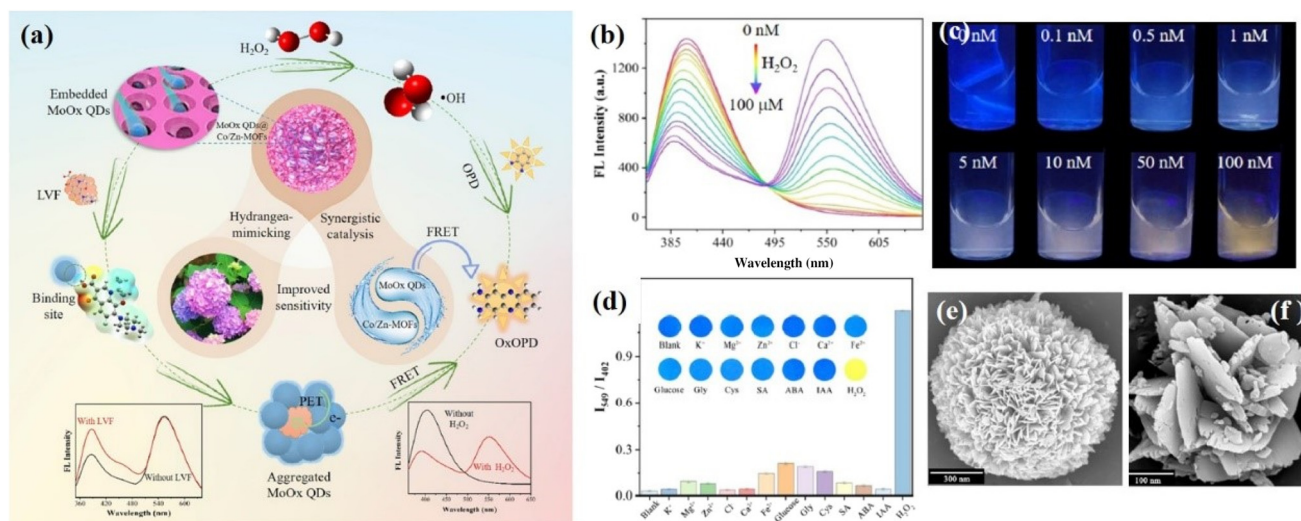
Fig. 21 (a) A schematic diagram of MoOx QDs@Co/Zn-MOFs for the detection of H_2O_2 and LVF. (b) The fluorescence spectra of the probe exposed to different concentrations of H_2O_2 and (c) solution under ultraviolet light with a catalytic reaction, (d) was the selectivity experiment. The SEM image of MoOx QDs@Co/Zn-MOFs before (e) and after (f) reaction with H_2O_2 for 1.0 h. Reproduced with permission from ref. 334. Copyright 2022, Elsevier.

CDs),[331] Fe/N-co-doped CDs (Fe/N-CDs),[332] FeCo/N-co-doped CDs (FeCo/N-CDs),[333] and Co- and N-doped CDs (CoN-CDs)[334] have been prepared and applied to propose DRFPs with o-PD.

The detection targets in the strategy of DRFRs constructed with auxiliary nanomaterials with peroxidase- or oxidase-like activities are commonly limited to reductant or reductant-related substrates or enzymes. An effect way to expand the detection target is using the molecular imprinting technique. Nanozymes are embedded in molecular-imprinted polymers (MIPs), and when the targets entre the recognition sites, the activity of the nanozyme is inhibited. For example, Zhang's group synthesized MIL-101(Co, Fe)@MIPs using MIL-101(Co, Fe) as a carrier for the ratiometric fluorescence detection of vanillin with high selectivity and sensitivity.[335] During the formation of the MIP layer, RhB was encapsulated as a reference. When the template molecule vanillin was completely eluted, imprinted cavities were formed in the MIP layer. H_2O_2 with a smaller size would enter the imprinted cavity channel and stimulated the peroxidase-like activity of MIL-101(Co, Fe) to oxidize the substrate TA to oxTA with high fluorescence. However, when vanillin was present in the detection system, it specifically occupied the imprinted cavities and the entry of H_2O_2 was prevented, thus reducing the fluorescence of oxTA. By changing the template molecules with prednisone and dexamethasone, the sensing platform still displayed a good performance, which shows great prospect in sensing applications.

Another problem faced by DRFRs constructed with nanoenzymes is their specificity. As discussed above, reductants such as AA, GSH, and other biothiols can also reduce peroxidase-like nanozymes. Thus, when these reductants coexist in one detection system, the detection selectivity is relatively low. Accordingly, to improve the selectivity of FNP-nanozyme-o-PD ternary systems, a nanozyme-o-PD binary system was proposed

for the detection of AA, which can reduce the interference from biothiols.[336-340] Using MnO_2 nanosheets as a model nanozyme, the detection mechanism is presented in Fig. 17c.[336] On one hand, MnO_2 NSs oxidize o-PD to yellow-emissive fluorescent DPA. AA was first oxidized by MnO_2 NSs to dehydro-L-ascorbic acid (DHAA), which in turn reacted with o-PD to produce a quinoxaline derivative 3-(1,2-dihydroxyethyl) furo[3,4-b]quinoxaline-(3H)-one (DFQ) with blue emission at around 430 nm. Because the blue emission originated from the presence of AA, GSH, which can strongly interfere with MnO_2 NS-based fluorescent sensors, had no interfering effect. This MnO_2-o-PD system could be used to detect AA[336] and AA-related reactions, such as ALP.[337] Based on a similar mechanism, an MnO_2 NS-o-PD ratiometric fluorescence system was proposed for the detection of the activity of α-glucosidase (α-Glu), which can catalyze the substrate 2-O-α-D-glucopyranose-L-ascorbic acid (AAG) to produce AA,[338] and the CuO NP-o-PD ratiometric fluorescence system was proposed for the detection of AA in serum and fruits.[339] The Cu^{2+}-AA-o-PD ternary system was proposed for the detection of bleomycin, which complexes with Cu^{2+} to form larger CuNPs, weakening the autocatalytic activity of Cu^{2+}.[340]

4. Conclusion and perspectives

DRFPs display improved accuracy and sensitivity due to their intrinsic built-in correction and low background signals. Especially, DRFPs can realize visual detection, making on-site rapid detection possible. In this review, we provided a comprehensive and systematic overview of the design of DRFPs based on FNPs, such as CDs, QDs, MOF, and NCs. The construction strategies mainly involved four types, including hybrid nanoparticles, single nanoparticles with intrinsic dual emission,

target analyte-induced fluorescence ratio and DRFPs based on auxiliary nanomaterials. However, although great progress has been achieved in the field of FNP-based DRFPs, there are still several limitations.

Firstly, compared to organic fluorescent molecules with a clear chemical structure, the structure and the groups of FNPs are not clear, and their fluorescence detection mechanism are complex. The preparation process of FNPs is usually complex, making it difficult to ensure that each particle has the same optical and chemical properties, which may affect their repeatability and accuracy. Also, FNPs pose potential risks when used for detection in biological systems due to their uncertain biological safety, such as they can remain in the reticuloendothelial system for a long time and cannot be metabolized quickly.

Secondly, only one target can be detected using one type of DRFP probe, and a few DRFPs can detect two types of substances based on the "on–off–on" mode. Actually, there are usually multiple contaminants in real complicated sample matrices simultaneously, such as metal ions, organic compounds, and antibiotics. Therefore, it is highly desirable to develop high-throughput DRFPs for the simultaneous detection of multiple targets. Although ion-imprinted ratiometric fluorescence probes for the simultaneous detection of two types of metal ions have been reported by our group,[341–343] and the DRFP-based array strategy can provide an attractive possibility for multi-analyte detection,[330] significant efforts are still needed to achieve high-throughput detection.

Thirdly, the selectivity of DRFPs should be further improved. For example, it is difficult for DRFRs to distinguish different TCs based on the change in the fluorescence signal of lanthanide ions by AE. DRFPs based on IFE cannot distinguish the substrate with a similar absorbance spectrum band. The molecularly imprinted technique can improve the selectivity of chemical sensors. However, it is necessary to overcome the various defects associated with MIPs, such as higher mass transfer resistance in high-crosslinked MIPs and decreased fluorescence performance caused by the imprinting process. Alternatively, FNPs are doped in the MIPs randomly, and the analyte-independent disturbance of FNPs results in a higher background. Also, the target is immobilized in the recognition sites, and thus many fluorescence detection mechanisms such as AEQ and AIE occur, making it difficult to adopt MIDRFPs. Thus, more efforts should be made to improve the detection sensitivity of MIDRFPs.

Fourthly, the stability of FNP-based DRFPs should be further improved. Single-emissive MOFs or MOFs with induced dual emission, even non-fluorescence MOFs can be employed to construct DRFPs. However, many MOFs cannot exist stably under acidic and basic condition and in aqueous solutions. Therefore, the solubility and stability of MOF-based DRFPs need to be improved. Also, the leakage of guest dyes or FNPs from encapsulated MOFs induces a higher background, which should be solved to obtain high detection sensitivity. QDs are sensitive to pH, temperature, and other environmental conditions, which can easily cause fluorescence quenching of

FNPs. NCs have a low fluorescence quantum yield, easy oxidation and poor stability. When used in real samples, the performance and stability of FNPs should be improved.

Fifthly, most DRFPs serve for a limited target. For example, lanthanide ion-based DRFPs are often employed to detect sensitizers based on AE, such as TCs and DPA. DRFPs based on the etching of Ag NPs are often employed to detect H_2O_2. DRFPs based on auxiliary materials with peroxidase mimicking activities are commonly employed to detect H_2O_2, AA, and GSH. Thus, the strategy design must be more flexible and the universality of the detection must be strengthened.

There is a continuing need to improve the accuracy, sensitivity, and selectivity of FNP-based DRFP. In the future, new emerging FNPs with enhanced fluorescence property will improve the properties of DRFPs. It can be envisaged that portable low-cost on-site detection platforms will be provided based on the development of DRFPs.

Abbreviations

4-MU	4-Methylumbelliferone
4-MUP	4-Methylumbelliferyl phosphate
AA	Ascorbic acid
AAG	2-O-a-D-Glucopyranosyl-L-ascorbic acid
AChE	Acetylcholinesterase
ACQ	Aggregation-caused quenching
AE	Antenna effect
AEE	Aggregation-enhanced emission
AFB1	Aflatoxin B1
Ag NPRs	Silver nanoprisms
Ag_2S	Silver sulfide
$AgInS_2$	Silver indium sulfide
a-Glu	a-Glucosidase
AIE	Aggregation-induced emission
ALP	Alkaline phosphatase
AR	Amplex Red
AuNCs	Au nanoclusters
AuNPs	Au nanoparticles
BBDC	5-Borylbenzene-1,3-dicarboxylic acidee3
BBV	Methyl viologen
b-CDs	Blue carbon dots
BDC-$(OH)_2$	2,5-Dihydroxylterephthalic acid
BDC–$CH{=}CH_2$	2-Vinylterephthalic acid
BDC-NH_2	2-Aminoterephthalic acid
BPDC	4,4′-Biphenyldicarboxylicacid
Bpy	2,2-Bipyridine-5,5-dicarboxylic acid
BrNpA	4-Bromo-1,8-naphthalic anhydride
BSA	Bovine serum albumin
BTC	Bis(trichloromethyl) carbonate
CA	Cellulose acetate
CAP	Chloramphenicol
CDs	Carbon dots
CNC	Cellulose nanocrystal
COF	Covalent organic framework

CoN-CDs	Co- and N-doped CDs
CTC	Chlortetracycline
Cu-CDs	Cu doped CDs
CuInS$_2$	Copper indium sulfide
CuNCs	Copper nanoclusters
DA	Dopamine
DAP	2,3-Diaminophenazine
D-CDs	Dual-emissive CDs
DCNP	Diethyl cyanophosphonate
DD-CDs	Dual excitation dual emission CDs
DFQ	3-(1,2-Dihydroxyethyl) furo [3,4-*b*] quinoxa-line-(3*H*)-one
DHAA	Dehydro-L-ascorbic acid
D-HOF	Hydrogen-bonded organic framework
D-MOFs	Dual emissive MOFs
D-NH	Dual emissive nanohybrid
DOX	Doxorubicin
DPA	Dipicolinic acid
D-QDs	Dual emission QDs
DRFP	Dual emission ratiometric fluorescent probes
EDA	Ethylenediamine
EDA-GO	Ethylenediamine grafted graphene oxide
EDC	1-Ethyl-3-(3-dimethylaminopropyl) carbodiimide
ET	Energy transfer
Eu-DPA/ PTA-NH$_2$	Eu-dipicolinic acid/2-aminophthalic acid
ESIPT	Excited-state intramolecular proton transfer
Fe/N-CDs	Fe/N-co-doped CDs
FeCo/N-CDs	FeCo/N-co-doped CDs
FITC	Fluorescein isothiocyanate
FNPs	Fluorescence nanoparticles
FRET	Fluorescence resonance energy transfer
g-C$_3$N$_4$	Nanoscale graphitic carbon nitride
g-CDs	Green carbon dots
GCU	β-Glucuronidase
GDP	Guanine diphosphate
Glu	Glucose
GMP	Guanine monophosphate
GSH	Glutathione
H$_2$BDC	Terephthalic acid
H$_2$BDC–CH=CH$_2$	2-Vinylterephthalic acid
H$_2$BDC-OH	2-Hydroxyterephthalic acid
H$_2$DATA	2,5-Diaminoterephthalic acid
H$_2$NDC	1,4-Naphthalene dicarboxylic acid
H$_2$TPA	Terephthalic acid
H$_3$BTC	1,3,5-Trimesic acid
H$_4$BTC	1,2,4,5-Benzenetetracarboxylic acid
H$_4$L	[1,1′:4′,1″-Terphenyl]-2′,4,4″,5′-tetracarboxylic acid
H$_6$L$_1$	Hexakis-(4-carboxylatophenoxy) cyclotriphosphazene
HAS	Human serum albumin
HCHO	Formaldehyde
HOF	Hydrogen-bonded organic framework

HOMO	Highest occupied molecular orbital
HQ	8-Hydroxyquinoline
ICT	Intramolecular charge transfer
IFE	Inner filter effect
TICT	Twist intramolecular charge transfer

Conflicts of interest

There are no conflicts to declare.

Acknowledgements

References

1 W. Q. Meng, A. C. Sedgwick, N. Kwon, M. Sun, K. Xiao, X. P. He, E. V. Anslyn, T. D. James and J. Yoon, Fluorescent probes for the detection of chemical warfare agents, *Chem. Soc. Rev.*, 2023, **52**, 601–662.

2 Y. Sun, P. Sun, Z. Li, L. Qu and W. Guo, Natural flavylium-inspired far-red to NIR-II dyes and their applications as fluorescent probes for biomedical sensing, *Chem. Soc. Rev.*, 2022, **51**, 7170–7205.

3 X. Zhu, W. Jiang, Y. Zhao, H. Liu and B. Sun, Single, dual and multi-emission carbon dots based optosensing for food safety, *Trends Food Sci. Technol.*, 2021, **111**, 388–404.

4 J. Tian, M. An, X. Zhao, Y. Wang and M. Hasan, Advances in Fluorescent Sensing Carbon Dots: An Account of Food Analysis, *ACS Omega*, 2023, **8**, 9031–9039.

5 C. S. M. Martins, A. P. LaGrow and J. A. V. Prior, Quantum Dots for Cancer-Related miRNA Monitoring, *ACS Sens.*, 2022, **7**, 1269–1299.

6 J. W. Zhou, X. M. Zou, S. H. Song and G. H. Chen, Quantum Dots Applied to Methodology on Detection of Pesticide and Veterinary Drug Residues, *J. Agric. Food Chem.*, 2018, **66**, 1307–1319.

7 T. Wu, X.-j. Gao, F. Ge and H.-g. Zheng, Metal–organic frameworks (MOFs) as fluorescence sensors: principles, development and prospects, *CrystEngComm*, 2022, **24**, 7881–7901.

8 Y. Zhao, H. Zeng, X. W. Zhu, W. Lu and D. Li, Metal-organic frameworks as photoluminescent biosensing platforms: mechanisms and applications, *Chem. Soc. Rev.*, 2021, **50**, 4484–4513.

9 B. Qu, J. Sun, P. Li and L. Jing, Current advances on g-C$_3$N$_4$-based fluorescence detection for environmental contaminants, *J. Hazard. Mater.*, 2022, **425**, 127990.

10 L. Chen, D. Liu, J. Peng, Q. Du and H. He, Ratiometric fluorescence sensing of metal-organic frameworks: Tactics and perspectives, *Coord. Chem. Rev.*, 2020, **404**, 213113.

11 F. Y. Ruiqi Zhang, H. Yicun, K. Depeng, Y. Qianghua, X. Jinxia and C. Li, Rhodamine-based ratiometric fluorescent probes based on excitation energy transfer mechanisms: construction and applications in ratiometric sensing, *RSC Adv.*, 2016, **6**, 50732–50760.

12 L. Zhao, C. Zhao, J. Zhou, H. Ji, Y. Qin, G. Li, L. Wu and X. Zhou, Correction: Conjugated polymer-based luminescent probes for ratiometric detection of biomolecules, *J. Mater. Chem. B*, 2022, **10**, 5493.

13 A. Bigdeli, F. Ghasemi, S. Abbasi-Moayed, M. Shahrajabian, N. Fahimi-Kashani, S. Jafarinejad, M. A. Farahmand Nejad and M. R. Hormozi-Nezhad, Ratiometric fluorescent nanoprobes for visual detection: Design principles and recent advances - A review, *Anal. Chim. Acta*, 2019, **1079**, 30–58.

14 C. Chen, R. Tian, Y. Zeng, C. Chu and G. Liu, Activatable Fluorescence Probes for "Turn-On" and Ratiometric Biosensing and Bioimaging: From NIR-I to NIR-II, *Bioconjugate Chem.*, 2020, **31**, 276–292.

15 R. Gui, H. Jin, X. Bu, Y. Fu, Z. Wang and Q. Liu, Recent advances in dual-emission ratiometric fluorescence probes for chemo/biosensing and bioimaging of biomarkers, *Coord. Chem. Rev.*, 2019, **383**, 82–103.

16 Y. Cai, J. You, Z. You, F. Dong, S. Du and L. Zhang, Profuse color-evolution-based fluorescent test paper sensor for rapid and visual monitoring of endogenous Cu^{2+} in human urine, *Biosens. Bioelectron.*, 2018, **99**, 332–337.

17 L. He, X. Yang, K. Xu, Y. Yang and W. Lin, A multifunctional logic gate by means of a triple-chromophore fluorescent biothiol probe with diverse fluorescence signal patterns, *Chem. Commun.*, 2017, **53**, 13168–13171.

18 P. Chen, J. Wu, H. Fei, H. He, S. Cao, L. Zuo, Y. Jin, L. Zhang and S. Du, Acoustofluidics-manipulated triple-emission fluorescent nanoprobe aggregates with multicolor-variation for colorimetric quantitative assay, *Chem. Eng. J.*, 2022, **441**, 135976.

19 H. Zhao, J. Ni, J. J. Zhang, S. Q. Liu, Y. J. Sun, H. Zhou, Y. Q. Li and C. Y. Duan, A trichromatic MOF composite for multidimensional ratiometric luminescent sensing, *Chem. Sci.*, 2018, **9**, 2918–2926.

20 S. Tang, D. Chen, Y. Yang, C. Wang, X. Li, Y. Wang, C. Gu and Z. Cao, Mechanisms behind multicolor tunable Near-Infrared triple emission in graphene quantum dots and ratio fluorescent probe for water detection, *J. Colloid Interface Sci.*, 2022, **617**, 182–192.

21 Q. Yang, J. Li, X. Wang, H. Xiong and L. Chen, Ternary Emission of a Blue-, Green-, and Red-Based Molecular Imprinting Fluorescence Sensor for the Multiplexed and Visual Detection of Bovine Hemoglobin, *Anal. Chem.*, 2019, **91**, 6561–6568.

22 Q. Yang, C. Li, J. Li, X. Wang, M. Arabi, H. Peng, H. Xiong and L. Chen, Rational construction of a triple emission molecular imprinting sensor for accurate naked-eye detection of folic acid, *Nanoscale*, 2020, **12**, 6529–6536.

23 L. Zhao, C. Zhao, J. Zhou, H. Ji, Y. Qin, G. Li, L. Wu and X. Zhou, Conjugated polymer-based luminescent probes for ratiometric detection of biomolecules, *J. Mater. Chem. B*, 2022, **10**, 7309–7327.

24 M. H. Lee, J. S. Kim and J. L. Sessler, Small molecule-based ratiometric fluorescence probes for cations, anions, and biomolecules, *Chem. Soc. Rev.*, 2015, **44**, 4185–4191.

25 S. H. Park, N. Kwon, J. H. Lee, J. Yoon and I. Shin, Synthetic ratiometric fluorescent probes for detection of ions, *Chem. Soc. Rev.*, 2020, **49**, 143–179.

26 P. Wu, X. Hou, J. J. Xu and H. Y. Chen, Ratiometric fluorescence, electrochemiluminescence, and photoelectrochemical chemo/biosensing based on semiconductor quantum dots, *Nanoscale*, 2016, **8**, 8427–8442.

27 C. Ji, Y. Zhou, R. M. Leblanc and Z. Peng, Recent Developments of Carbon Dots in Biosensing: A Review, *ACS Sens.*, 2020, **5**, 2724–2741.

28 L. Yang, Y. Song and L. Wang, Multi-emission metal-organic framework composites for multicomponent ratiometric fluorescence sensing: recent developments and future challenges, *J. Mater. Chem. B*, 2020, **8**, 3292–3315.

29 N. Patel, P. Shukla, P. Lama, S. Das and T. K. Pal, Engineering of Metal–Organic Frameworks as Ratiometric Sensors, *Cryst. Growth Des.*, 2022, **22**, 3518–3564.

30 X. Huang, J. Song, B. C. Yung, X. Huang, Y. Xiong and X. Chen, Ratiometric optical nanoprobes enable accurate molecular detection and imaging, *Chem. Soc. Rev.*, 2018, **47**, 2873–2920.

31 Y. Shen, Y. Wei, C. Zhu, J. Cao and D.-M. Han, Ratiometric fluorescent signals-driven smartphone-based portable sensors for onsite visual detection of food contaminants, *Coord. Chem. Rev.*, 2022, **458**, 214442.

32 H. S. Jung, P. Verwilst, W. Y. Kim and J. S. Kim, Fluorescent and colorimetric sensors for the detection of humidity or water content, *Chem. Soc. Rev.*, 2016, **45**, 1242–1256.

33 G. Chen, F. Song, X. Xiong and X. Peng, Fluorescent Nanosensors Based on Fluorescence Resonance Energy Transfer (FRET), *Ind. Eng. Chem. Res.*, 2013, **52**, 11228–11245.

34 L. Wu, C. Huang, B. P. Emery, A. C. Sedgwick, S. D. Bull, X. P. He, H. Tian, J. Yoon, J. L. Sessler and T. D. James, Forster resonance energy transfer (FRET)-based small-molecule sensors and imaging agents, *Chem. Soc. Rev.*, 2020, **49**, 5110–5139.

35 Z. Wang, L. Zhang, Y. Hao, W. Dong, Y. Liu, S. Song, S. Shuang, C. Dong and X. Gong, Ratiometric fluorescent sensors for sequential on-off-on determination of riboflavin, Ag^+ and L-cysteine based on NPCl-doped carbon quantum dots, *Anal. Chim. Acta*, 2021, **1144**, 1–13.

36 Y.-S. He, C.-G. Pan, H.-X. Cao, M.-Z. Yue, L. Wang and G.-X. Liang, Highly sensitive and selective dual-emission ratiometric fluorescence detection of dopamine based on carbon dots-gold nanoclusters hybrid, *Sens. Actuators, B*, 2018, **265**, 371–377.

37 X. Yue, Y. Li, S. Xu, J. Li, M. Li, L. Jiang, M. Jie and Y. Bai, A portable smartphone-assisted ratiometric fluorescence sensor for intelligent and visual detection of malachite green, *Food Chem.*, 2022, **371**, 131164.

38 Y. Ma, Y. Wang, Y. Liu, L. Shi and D. Yang, A cascade-triggered ratiometric fluorescent sensor based on nanocomposite for lactate determination, *Sens. Actuators, B*, 2022, **355**, 131295.

39 S. Rong, Q. Chen, G. Xu, F. Wei, J. Yang, D. Ren, X. Cheng, X. Xia, J. Li, M. Gao, Q. Hu and Y. Cen, Novel and facile synthesis of heparin sulfur quantum dots via oxygen acceleration for ratiometric sensing of uric acid in human serum, *Sens. Actuators, B*, 2022, **353**, 131146.

40 J. S. Kim and D. T. Quang, Calixarene-derived fluorescent probes, *Chem. Rev.*, 2007, **107**, 3780–3799.

41 Y. Ye, T. Wu, X. Jiang, J. Cao, X. Ling, Q. Mei, H. Chen, D. Han, J. J. Xu and Y. Shen, Portable Smartphone-Based QDs for the Visual Onsite Monitoring of Fluoroquinolone Antibiotics in Actual Food and Environmental Samples, *ACS Appl. Mater. Interfaces*, 2020, **12**, 14552–14562.

42 L. Yu, Q. Zheng, H. Wang, C. Liu, X. Huang and Y. Xiao, Double-Color Lanthanide Metal-Organic Framework Based Logic Device and Visual Ratiometric Fluorescence Water Microsensor for Solid Pharmaceuticals, *Anal. Chem.*, 2020, **92**, 1402–1408.

43 Q. Zhang, Z. Zhang, S. Xu, L. Da, D. Lin and C. Jiang, Enzyme-free and rapid visual quantitative detection for pesticide residues utilizing portable smartphone integrated paper sensor, *J. Hazard. Mater.*, 2022, **436**, 129320.

44 J. Luo, Z. Xie, J. W. Lam, L. Cheng, H. Chen, C. Qiu, H. S. Kwok, X. Zhan, Y. Liu, D. Zhu and B. Z. Tang, Aggregation-induced emission of 1-methyl-1,2,3,4,5-pentaphenylsilole, *Chem. Commun.*, 2001, **18**, 1740–1741.

45 Y. Hong, J. W. Lam and B. Z. Tang, Aggregation-induced emission: phenomenon, mechanism and applications, *Chem. Commun.*, 2009, **29**, 4332–4353.

46 L. Zhu, B. Zhu, J. Luo and B. Liu, Design and Property Modulation of Metal–Organic Frameworks with Aggregation-Induced Emission, *ACS Mater. Lett.*, 2020, **3**, 77–89.

47 Z. Zhang, M. Kang, H. Tan, N. Song, M. Li, P. Xiao, D. Yan, L. Zhang, D. Wang and B. Z. Tang, The fast-growing field of photo-driven theranostics based on aggregation-induced emission, *Chem. Soc. Rev.*, 2022, **51**, 1983–2030.

48 H. Wang, L. Da, L. Yang, S. Chu, F. Yang, S. Yu and C. Jiang, Colorimetric fluorescent paper strip with smartphone platform for quantitative detection of cadmium ions in real samples, *J. Hazard. Mater.*, 2020, **392**, 122506.

49 R. Jiang, D. Lin, Q. Zhang, L. Li and L. Yang, Multiplex chroma-response based fluorescent smartphone sensing platform for rapid and visual quantitative determination of antibiotic residues, *Sens. Actuators, B*, 2022, **350**, 130902.

50 A. Singh, A. Nair, S. Shah, S. Ray and N. D. Singh, ESIPT-, AIE-, and AIE + ESIPT-Based Light-Activated Drug Delivery Systems and Bioactive Donors for Targeted Disease Treatment, *J. Med. Chem.*, 2023, **66**, 3732–3745.

51 L. Fan, C. Tong, Y. Cao, R. Long, Q. Wei, F. Wang, X. Tong, S. Shi and Y. Guo, Highly specific esterase activated AIE plus ESIPT probe for sensitive ratiometric detection of carbaryl, *Talanta*, 2022, **246**, 123517.

52 A. Ito, S. Ishizaka and N. Kitamura, A ratiometric TICT-type dual fluorescent sensor for an amino acid, *Phys. Chem. Chem. Phys.*, 2010, **12**, 6641–6649.

53 Q. Hu, Q. Huang, K. Liang, Y. Wang, Y. Mao, Q. Yin and H. Wang, An AIE + TICT activated colorimetric and ratiometric fluorescent sensor for portable, rapid, and selective detection of phosgene, *Dyes Pigm.*, 2020, **176**, 108229.

54 A. Gupta and N. Kumar, A review of mechanisms for fluorescent "turn-on" probes to detect Al^{3+} ions, *RSC Adv.*, 2016, **6**, 106413–106434.

55 A. Pal, S. Srivastava, P. Saini, S. Raina, P. Ingole, R. Gupta and S. Sapra, Probing the Mechanism of Fluorescence Quenching of QDs by Co(III)-Complexes: Size of QD and Nature of the Complex Both Dictate Energy and Electron Transfer Processes, *J. Phys. Chem. C*, 2015, **119**, 22690–22699.

56 H. Wang, L. Yang, S. Chu, B. Liu, Q. Zhang, L. Zou, S. Yu and C. Jiang, Semiquantitative Visual Detection of Lead Ions with a Smartphone via a Colorimetric Paper-Based Analytical Device, *Anal. Chem.*, 2019, **91**, 9292–9299.

57 Y. Zhou, T. Wu, L. Duan, G. Hu, J. Shi, Y. Nie and Y. Zhou, Synthesizing carbon dots with functional preservation strategy as a facile ratiometric fluorescent sensing platform for monitoring hypochlorite in living cells and zebrafish, *Sens. Actuators, B*, 2022, **365**, 131946.

58 X. Chen, J. Lin, Y. Zhuang, S. Huang, J. Chen and Z. Han, Dual-mode turn-on ratiometric fluorescence sensor based on carbon dots and $CuInS_2$/ZnS quantum dots for detection of chlorotetracycline, *Spectrochim. Acta, Part A*, 2022, **270**, 120851.

59 R. C. Castro, R. Pascoa, M. Saraiva, J. L. M. Santos and D. S. M. Ribeiro, Photoluminescent and visual determination of ibandronic acid using a carbon dots/$AgInS_2$ quantum dots ratiometric sensing platform, *Spectrochim. Acta, Part A*, 2022, **267**, 120592.

60 L. Yu, C. He, Q. Zheng, L. Feng, L. Xiong and Y. Xiao, Dual Eu-MOFs based logic device and ratiometric fluorescence paper microchip for visual H_2O_2 assay, *J. Mater. Chem. C*, 2020, **8**, 3562–3570.

61 L. Chen, J. Lu, M. Luo, H. Yu, X. Chen, J. Deng, X. Hou, E. Hao, J. Wei and P. Li, A ratiometric fluorescent sensing system for the selective and ultrasensitive detection of pesticide residues via the synergetic effects of copper nanoclusters and carbon dots, *Food Chem.*, 2022, **379**, 132139.

62 Y. Qin, P. Huang and F.-Y. Wu, Histamine-responsive dye-incorporated carbon dots for visual monitoring of food spoilage, *Sens. Actuators, B*, 2022, **365**, 131911.

63 W. Xue, J. Zhong, H. Wu, J. Zhang and Y. Chi, A visualized ratiometric fluorescence sensing system for copper ions

based on gold nanoclusters/perovskite quantum dot@SiO₂ nanocomposites, *Analyst*, 2021, **146**, 7545–7553.

64 Y. Zhao, Y. Xu, L. Shi and Y. Fan, Perovskite Nanomaterial-Engineered Multiplex-Mode Fluorescence Sensing of Edible Oil Quality, *Anal. Chem.*, 2021, **93**, 11033–11042.

65 K. Jia, K. Yi, W. Zhang, P. Yan, S. Zhang and X. Liu, Carbon nanodots calibrated fluorescent probe of QD@amphiphilic polyurethane for ratiometric detection of Hg(ɪɪ), *Sens. Actuators, B*, 2022, **370**, 132443.

66 N. Zhao, J. Song, Z. Huang, X. Yang, Y. Wang and L. Zhao, Ratiometric fluorescence probe of Cu^{2+} and biothiols by using carbon dots and copper nanoclusters, *RSC Adv.*, 2021, **11**, 33662–33674.

67 J. Hou, P. Jia, K. Yang, T. Bu, S. Zhao, L. Li and L. Wang, Fluorescence and Colorimetric Dual-Mode Ratiometric Sensor Based on Zr-Tetraphenylporphyrin Tetrasulfonic Acid Hydrate Metal-Organic Frameworks for Visual Detection of Copper Ions, *ACS Appl. Mater. Interfaces*, 2022, **14**, 13848–13857.

68 J. Qiu, L. Na, Y. Li, W. Bai, J. Zhang and L. Jin, N,S-GQDs mixed with CdTe quantum dots for ratiometric fluorescence visual detection and quantitative analysis of malachite green in fish, *Food Chem.*, 2022, **390**, 133156.

69 N. Liang, X. Hu, W. Li, Y. Wang, Z. Guo, X. Huang, Z. Li, X. Zhang, J. Zhang, J. Xiao, X. Zou and J. Shi, A dual-signal fluorescent sensor based on MoS₂ and CdTe quantum dots for tetracycline detection in milk, *Food Chem.*, 2022, **378**, 132076.

70 F. Shahdost-Fard, A. Bigdeli and M. R. Hormozi-Nezhad, A Smartphone-Based Fluorescent Electronic Tongue for Tracing Dopaminergic Agents in Human Urine, *ACS Chem. Neurosci.*, 2021, **12**, 3157–3166.

71 Z. Lu, J. Li, K. Ruan, M. Sun, S. Zhang, T. Liu, J. Yin, X. Wang, H. Chen, Y. Wang, P. Zou, Q. Huang, J. Ye and H. Rao, Deep learning-assisted smartphone-based ratio fluorescence for "on–off-on" sensing of Hg^{2+} and thiram, *Chem. Eng. J.*, 2022, **435**, 134979.

72 L. Han, T. Liu, D. Cui, J. Yi, W. Jiang, X. Li, N. Niu and L. Chen, Quantitative detection of captopril in urine by smartphone-assisted ratiometric fluorescence sensing platform, *Spectrochim. Acta, Part A*, 2022, **280**, 121562.

73 S. Sh. Mohammed Ameen, N. M. Sher Mohammed and K. M. Omer, Visual monitoring of silver ions and cysteine using bi-ligand Eu-based metal organic framework as a reference signal: Color tonality, *Microchem. J.*, 2022, **181**, 107721.

74 Y. Yan, J. Sun, K. Zhang, H. Zhu, H. Yu, M. Sun, D. Huang and S. Wang, Visualizing gaseous nitrogen dioxide by ratiometric fluorescence of carbon nanodots-quantum dots hybrid, *Anal. Chem.*, 2015, **87**, 2087–2093.

75 W. He, R. Gui, H. Jin, B. Wang, X. Bu and Y. Fu, Ratiometric fluorescence and visual imaging detection of dopamine based on carbon dots/copper nanoclusters dual-emitting nanohybrids, *Talanta*, 2018, **178**, 109–115.

76 C. Wang, H. Lin, Z. Xu, Y. Huang, M. G. Humphrey and C. Zhang, Tunable Carbon-Dot-Based Dual-Emission Fluorescent Nanohybrids for Ratiometric Optical Thermometry in Living Cells, *ACS Appl. Mater. Interfaces*, 2016, **8**, 6621–6628.

77 X. J. Wu, F. Kong, C. Q. Zhao and S. N. Ding, Ratiometric fluorescent nanosensors for ultra-sensitive detection of mercury ions based on AuNCs/MOFs, *Analyst*, 2019, **144**, 2523–2530.

78 C. Zou, M. F. Foda, X. Tan, K. Shao, L. Wu, Z. Lu, H. S. Bahlol and H. Han, Carbon-Dot and Quantum-Dot-Coated Dual-Emission Core-Satellite Silica Nanoparticles for Ratiometric Intracellular Cu^{2+} Imaging, *Anal. Chem.*, 2016, **88**, 7395–7403.

79 P. Lesani, G. Singh, Z. Lu, M. Mirkhalaf, E. J. New and H. Zreiqat, Two-photon ratiometric carbon dot-based probe for real-time intracellular pH monitoring in 3D environment, *Chem. Eng. J.*, 2022, **433**, 133668.

80 S. Tang, D. Chen, X. Li, C. Wang, T. Li, J. Ma, G. Guo and Q. Guo, Promising energy transfer system between fuorine and nitrogen Co-doped graphene quantum dots and Rhodamine B for ratiometric and visual detection of doxycycline in food, *Food Chem.*, 2022, **388**, 132936.

81 R. S. Li, J. Liu, Y. Yan, C. Su, T. Lai, Y. Liao, Y. F. Li, N. Li and C. Z. Huang, Aggregation-Enhanced Energy Transfer for Mitochondria-Targeted ATP Ratiometric Imaging in Living Cells, *Anal. Chem.*, 2021, **93**, 11878–11886.

82 H. Tian, Y. Dai, W. Fu, H. Liu, M. Li, M. Lv and X. Yin, Dansyl-modified carbon dots with dual-emission for pH sensing, Fe^{3+} ion detection and fluorescent ink, *RSC Adv.*, 2020, **10**, 36971–36979.

83 H. Kou, S. Pang, B. Yang, M. Wang, J. Ding, Z. Zhang and X. Yang, A dual-emission ratiometric fluorescent nanoprobe based on silicon nanoparticles and carbon dots for efficient detection of Cu(ɪɪ), *CrystEngComm*, 2021, **23**, 2599–2605.

84 C. Wang, T. Hu, T. Thomas, S. Song, Z. Wen, C. Wang, Q. Song and M. Yang, Surface state-controlled C-dot/C-dot based dual-emission fluorescent nanothermometers for intra-cellular thermometry, *Nanoscale*, 2018, **10**, 21809–21817.

85 Y. Yang, G. Mao, X. Ji and Z. He, Synthesis of bio-templated clickable quantum dots a dual-emitting organic/inorganic complex for ratiometric fluorescence visual assay of blood glucose, *J. Mater. Chem. B*, 2022, **10**, 4473.

86 W. Sun, F. Zhang, M. Wang, N. Wang, G. Wang and X. Su, A ratiometric fluorescence strategy based on polyethyleneimine surface-modified carbon dots and Eosin Y for the ultrasensitive determination of protamine and trypsin, *Analyst*, 2022, **147**, 677–684.

87 Q. Lin, H. Chu, J. Chen, L. Gao, W. Zong, S. Han and J. Li, Dual-emission ratiometric fluorescence probe based on copper nanoclusters for the detection of rutin and picric acid, *Spectrochim. Acta, Part A*, 2022, **270**, 120829.

88 Y. Hao, W. Dong, Y. Liu, X. Wen, S. Shuang, Q. Hu, C. Dong and X. Gong, Nitrogen-doped carbon dots

coupled with morin-Al^{3+}: Cleverly design an integrated sensing platform for ratiometric optical dual-mode and smartphone-assisted visual detection of fluoride ion, *J. Hazard. Mater.*, 2022, **439**, 129596.

89 J. Zhou, Q. Zhou and C. Chu, Dyes-modified metal – organic frameworks composite as a sensitive, reversible and ratiometric fluorescent probe for the rapid detection of malachite green, *Microchem. J.*, 2022, **180**, 107631.

90 H. Wang, Q. Li, X. Niu and J. Du, Tetraphenylporphyrin-modified perovskite nanocrystals enable ratiometric fluorescent determination of sulfide ion in water samples, *J. Mater. Sci.*, 2021, **56**, 15029–15039.

91 Y. Zhan, Y. Zeng, L. Li, F. Luo, B. Qiu, Z. Lin and L. Guo, Ratiometric Fluorescent Hydrogel Test Kit for On-Spot Visual Detection of Nitrite, *ACS Sens.*, 2019, **4**, 1252–1260.

92 Y. Wang, J. Jian, B. Sun, Y. Wei, D. Pan, J. Cao and Y. Shen, Engineering of onsite point-of-care testing of Fe^{3+} with visual ratiometric fluorescent signals of copper nanoclusters-driven portable smartphone, *Sens. Actuators, B*, 2022, **370**, 132413.

93 Y. Zhan, F. Luo, L. Guo, B. Qiu, Y. Lin, J. Li, G. Chen and Z. Lin, Preparation of an Efficient Ratiometric Fluorescent Nanoprobe (m-CDs@[Ru(bpy)$_3$]$^{2+}$) for Visual and Specific Detection of Hypochlorite on Site and in Living Cells, *ACS Sens.*, 2017, **2**, 1684–1691.

94 H. Mei, Q. Wang, J. Jiang, X. Zhu, H. Wang, S. Qu and X. Wang, A novel ratiometric nanoprobe based on copper nanoclusters and graphitic carbon nitride nanosheets using Ce(III) as crosslinking agent and aggregation-induced effect initiator for sensitive detection of hydrogen peroxide and glucose, *Talanta*, 2022, **248**, 123604.

95 J. Zhou, Y. Xiao, X. Zhang and S. Wang, A novel ratiometric fluorescence nanoprobe based on aggregation-induced emission of silver nanoclusters for the label-free detection of biothiols, *Talanta*, 2018, **188**, 623–629.

96 X. Qin, Z. Zhang, T. Yang, L. Yuan, Y. Guo and X. Yang, Auto-fluorescence of cellulose paper with spatial solid phrase dispersion-induced fluorescence enhancement behavior for three heavy metal ions detection, *Food Chem.*, 2022, **389**, 133093.

97 T. Yang, C. M. Li, J. H. He, B. Chen, Y. F. Li and C. Z. Huang, Ratiometrically Fluorescent Electrospun Nanofibrous Film as a Cu^{2+}-Mediated Solid-Phase Immunoassay Platform for Biomarkers, *Anal. Chem.*, 2018, **90**, 9966–9974.

98 A. Chen, X. Peng, Z. Pan, K. Shao, J. Wang and M. Fan, Visual Assay of Glutathione in Vegetables and Fruits Using Quantum Dot Ratiometric Hybrid Probes, *J. Agric. Food Chem.*, 2018, **66**, 6431–6438.

99 X. Liu, N. Zhang, T. Bing and D. Shangguan, Carbon dots based dual-emission silica nanoparticles as a ratiometric nanosensor for Cu^{2+}, *Anal. Chem.*, 2014, **86**, 2289–2296.

100 X. Liang, Z. Lin, L. Li, D. Tang and J. Kong, Ratiometric fluorescence enzyme-linked immunosorbent assay based on carbon dots@SiO$_2$@CdTe quantum dots with dual

functionalities for alpha-fetoprotein, *Analyst*, 2022, **147**, 2851–2858.

101 L. Chen, L. Sun, J. Zheng, J. Dai, Y. Wu, X. Dai, C. Li and Y. Yan, Dual-emission ratiometric fluorescence detection of aspirin in human saliva: onsite naked-eye detection and high stability, *New J. Chem.*, 2017, **41**, 14551–14556.

102 Y. Cao, J. Li, M. Chen, L. Zhou, Q. Zhang, W. Liu and Y. Liu, Construction of multicolor fluorescence hydrogels based on the dual-emission CDs@SiO$_2$/AuNCs for alternative visual recognition of copper ions and glutathione, *Microchem. J.*, 2022, **181**, 107801.

103 J. An, R. Chen, M. Chen, Y. Hu, Y. Lyu and Y. Liu, An Ultrasensitive Turn-On Ratiometric Fluorescent Probes for Detection of Ag$^+$ Based on Carbon Dots/SiO$_2$ and Gold Nanoclusters, *Sens. Actuators, B*, 2021, **329**, 129097.

104 Y. Liu, M. Xiao, N. Xu, M. Yang and C. Yi, Point-of-need quantitation of 2,4-dichlorophenoxyacetic acid using a ratiometric fluorescent nanoprobe and a smartphone-based sensing system, *Sens. Actuators, B*, 2022, **367**, 132083.

105 R. Yao, Z. Li, P. Huo, C. Gong, J. Li, C. Fan and S. Pu, A Eu^{3+}-based high sensitivity ratiometric fluorescence sensor for determination of tetracycline combining bifunctional carbon dots by surface functionalization and heteroatom doping, *Dyes Pigm.*, 2022, **201**, 110190.

106 P. Huo, Z. Li, R. Yao, Y. Deng, C. Gong, D. Zhang, C. Fan and S. Pu, Dual-ligand lanthanide metal-organic framework for ratiometric fluorescence detection of the anthrax biomarker dipicolinic acid, *Spectrochim. Acta, Part A*, 2022, **282**, 121700.

107 C. Fu, F. Ai, J. Huang, Z. Shi, X. Yan and X. Zheng, Eu doped Ti$_3$C$_2$ quantum dots to form a ratiometric fluorescence platform for visual and quantitative point-of-care testing of tetracycline derivatives, *Spectrochim. Acta, Part A*, 2022, **272**, 120956.

108 Z. Shen, C. Zhang, X. Yu, J. Li, Z. Wang, Z. Zhang and B. Liu, Microwave-assisted synthesis of cyclen functional carbon dots to construct a ratiometric fluorescent probe for tetracycline detection, *J. Mater. Chem. C*, 2018, **6**, 9636–9641.

109 Q. Wang, X. Li, K. Yang, S. Zhao, S. Zhu, B. Wang, J. Yi, Y. Zhang, X. Song and M. Lan, Carbon Dots and Eu^{3+} Hybrid-Based Ratiometric Fluorescent Probe for Oxytetracycline Detection, *Ind. Eng. Chem. Res.*, 2022, **61**, 5825–5832.

110 M. Mo, X. Wang, L. Ye, Y. Su, Y. Zhong, L. Zhao, Y. Zhou and J. Peng, A simple paper-based ratiometric luminescent sensor for tetracyclines using copper nanocluster-europium hybrid nanoprobes, *Anal. Chim. Acta*, 2022, **1190**, 339257.

111 J. Zhang and G. Shi, Rational design of MoS$_2$ QDs and Eu^{3+} as a ratiometric fluorescent probe for point-of-care visual quantitative detection of tetracycline via smartphone-based portable platform, *Anal. Chim. Acta*, 2022, **1198**, 339572.

112 M. Yuan, Y. Jin, L. Yu, Y. Bu, M. Sun, C. Yuan and S. Wang, Europium-modified carbon nitride nanosheets for smartphone-based fluorescence sensitive recognition of anthrax biomarker dipicolinic acid, *Food Chem.*, 2023, **398**, 133884.

113 L. Han, Y. Z. Fan, M. Qing, S. G. Liu, Y. Z. Yang, N. B. Li and H. Q. Luo, Smartphones and Test Paper-Assisted Ratiometric Fluorescent Sensors for Semi-Quantitative and Visual Assay of Tetracycline Based on the Target-Induced Synergistic Effect of Antenna Effect and Inner Filter Effect, *ACS Appl. Mater. Interfaces*, 2020, **12**, 47099–47107.

114 X. Chen, L. Jia, L. Zhang, Y. Li and J. Xu, Stimulus response of HNT-CDs-Eu nano-sensor: Toward visual point-of-care monitoring of a bacterial spore biomarker with hypersensitive multi-color agarose gel based analytical device, *Colloids Surf., A*, 2022, **639**, 128356.

115 S. Yin and C. Tong, Lanthanide coordination polymer nanoparticles as a ratiometric fluorescence sensor for real-time and visual detection of tetracycline by a smartphone and test paper based on the analyte-triggered antenna effect and inner filter effect, *Anal. Chim. Acta*, 2022, **1206**, 339809.

116 Y. Xu, Y. Lin, N. Chu, Y. Xing and X. Chen, Crystal engineering of novel MOF@iCOF composite as a multifunction platform for targeted monitoring and capturing of norfloxacin, *Chem. Eng. J.*, 2022, **435**, 134907.

117 F. Ahmed, S. Iqbal and H. Xiong, Multifunctional dual emissive fluorescent probe based on europium-doped carbon dots (Eu-TCA/NCDs) for highly selective detection of chloramphenicol, Hg^{2+} and Fe^{3+}, *Environ. Sci.: Nano*, 2022, **9**, 2624–2637.

118 T. K. Mondal, U. K. Ghorai and S. K. Saha, Dual-Emissive Carbon Quantum Dot-Tb Nanocomposite as a Fluorescent Indicator for a Highly Selective Visual Detection of Hg(II) in Water, *ACS Omega*, 2018, **3**, 11439–11446.

119 C. Liu, D. Ning, C. Zhang, Z. Liu, R. Zhang, J. Zhao, T. Zhao, B. Liu and Z. Zhang, Dual-Colored Carbon Dot Ratiometric Fluorescent Test Paper Based on a Specific Spectral Energy Transfer for Semiquantitative Assay of Copper Ions, *ACS Appl. Mater. Interfaces*, 2017, **9**, 18897–18903.

120 Y. Shu, Q. Ye, T. Dai, Q. Xu and X. Hu, Encapsulation of Luminescent Guests to Construct Luminescent Metal-Organic Frameworks for Chemical Sensing, *ACS Sens.*, 2021, **6**, 641–658.

121 N. Zhang, D. Zhang, J. Zhao and Z. Xia, Fabrication of a dual-emitting dye-encapsulated metal-organic framework as a stable fluorescent sensor for metal ion detection, *Dalton Trans.*, 2019, **48**, 6794–6799.

122 Z. Zhang, Z. Wei, F. Meng, J. Su, D. Chen, Z. Guo and H. Xing, RhB-Embedded Zirconium-Naphthalene-Based Metal-Organic Framework Composite as a Luminescent Self-Calibrating Platform for the Selective Detection of Inorganic Ions, *Chemistry*, 2020, **26**, 1661–1667.

123 T. Du, J. Wang, T. Zhang, L. Zhang, C. Yang, T. Yue, J. Sun, T. Li, M. Zhou and J. Wang, An Integrating Platform of Ratiometric Fluorescent Adsorbent for Unconventional Real-Time Removing and Monitoring of Copper Ions, *ACS Appl. Mater. Interfaces*, 2020, **12**, 13189–13199.

124 M. Zhang, R. Liang, K. Li, T. Chen, S. Li, Y. Zhang, D. Zhang and X. Chen, Dual-emitting metal-organic frameworks for ratiometric fluorescence detection of fluoride and Al^{3+} in sequence, *Spectrochim. Acta, Part A*, 2022, **271**, 120896.

125 Y. Li, Z. Wei, Y. Zhang, Z. Guo, D. Chen, P. Jia, P. Chen and H. Xing, Dual-Emitting EY@Zr-MOF Composite as Self-Calibrating Luminescent Sensor for Selective Detection of Inorganic Ions and Nitroaromatics, *ACS Sustainable Chem. Eng.*, 2019, **7**, 6196–6203.

126 W. Liu, S.-Q. Li, J. Shao and J.-L. Tian, A dual-emission Acf@bioMOF-1 platform as fluorescence sensor for highly efficient detection of inorganic ions, *J. Solid State Chem.*, 2020, **290**, 121580.

127 H.-R. Fu, Y. Zhao, T. Xie, M.-L. Han, L.-F. Ma and S.-Q. Zang, Stable dye-encapsulated indium–organic framework as dual-emitting sensor for the detection of $Hg^{2+}/Cr_2O_7^{2-}$ and a wide range of nitro-compounds, *J. Mater. Chem. C*, 2018, **6**, 6440–6448.

128 X. Zheng, Y. Zhao, P. Jia, Q. Wang, Y. Liu, T. Bu, M. Zhang, F. Bai and L. Wang, Dual-Emission Zr-MOF-Based Composite Material as a Fluorescence Turn-On Sensor for the Ultrasensitive Detection of Al^{3+}, *Inorg. Chem.*, 2020, **59**, 18205–18213.

129 H. R. Fu, X. X. Wu, L. F. Ma, F. Wang and J. Zhang, Dual-Emission SG7@MOF Sensor via SC-SC Transformation: Enhancing the Formation of Excimer Emission and the Range and Sensitivity of Detection, *ACS Appl. Mater. Interfaces*, 2018, **10**, 18012–18020.

130 K. Xing, R. Fan, X. Du, X. Zheng, X. Zhou, S. Gai, P. Wang and Y. Yang, Dye-insertion dynamic breathing MOF as dual-emission platform for antibiotics detection and logic molecular operation, *Sens. Actuators, B*, 2019, **288**, 307–315.

131 Y. Shu, Q. Ye, T. Dai, J. Guan, Z. Ji, Q. Xu and X. Hu, Incorporation of perovskite nanocrystals into lanthanide metal-organic frameworks with enhanced stability for ratiometric and visual sensing of mercury in aqueous solution, *J. Hazard. Mater.*, 2022, **430**, 128360.

132 M. Yu, Y. Xie, X. Wang, Y. Li and G. Li, Highly Water-Stable Dye@Ln-MOFs for Sensitive and Selective Detection toward Antibiotics in Water, *ACS Appl. Mater. Interfaces*, 2019, **11**, 21201–21210.

133 X.-y. Sun, H.-j. Zhang, Q. Sun and E.-Q. Gao, PB@UiO-67-CDC-$(CH_3)_2$ as an Ultrasensitive Ratiometric Fluorescence Sensor: Visible "Turn-On" Effect for Detecting Preservatives and Amino Acids, *Cryst. Growth Des.*, 2021, **21**, 7218–7229.

134 X. Q. Wang, M. Zhang, X. Ma, J. Yang, D. Wu, J. Yang and T. Hu, RhB-encapsulated metal-organic cage as a dual-

emission fluorescence sensor for detection of malachite green and glycine, *Spectrochim. Acta, Part A*, 2022, **279**, 121346.

135 D. M. Chen, N. N. Zhang, C. S. Liu and M. Du, Dual-Emitting Dye@MOF Composite as a Self-Calibrating Sensor for 2,4,6-Trinitrophenol, *ACS Appl. Mater. Interfaces*, 2017, **9**, 24671–24677.

136 C. Wang, L. Tian, W. Zhu, S. Wang, P. Wang, Y. Liang, W. Zhang, H. Zhao and G. Li, Dye@bio-MOF-1 Composite as a Dual-Emitting Platform for Enhanced Detection of a Wide Range of Explosive Molecules, *ACS Appl. Mater. Interfaces*, 2017, **9**, 20076–20085.

137 Y. Zhang, B. Li, H. Ma, L. Zhang and W. Zhang, An RGH–MOF as a naked eye colorimetric fluorescent sensor for picric acid recognition, *J. Mater. Chem. C*, 2017, **5**, 4661–4669.

138 L. Yang, Y. L. Liu, C. G. Liu, F. Ye and Y. Fu, Two luminescent dye@MOFs systems as dual-emitting platforms for efficient pesticides detection, *J. Hazard. Mater.*, 2020, **381**, 120966.

139 Z. Wei, D. Chen, Z. Guo, P. Jia and H. Xing, Eosin Y-Embedded Zirconium-Based Metal-Organic Framework as a Dual-Emitting Built-In Self-Calibrating Platform for Pesticide Detection, *Inorg. Chem.*, 2020, **59**, 5386–5393.

140 Y. Zhang, L. Gao, S. Ma and T. Hu, Porous MB@Cd-MOF Obtained by Post-Modification: Self-Calibrated Fluorescent Turn-on Sensor for Highly Sensitive Detection of Carbaryl, *Cryst. Growth Des.*, 2022, **22**, 2662–2669.

141 M. Li, Y. Gao, W. Yang, C. Zhang, Y. Fang, C. Wang, S. Song and Q. Pan, Dye-Encapsulated Lanthanide-Based Metal-Organic Frameworks as a Dual-Emission Sensitization Platform for Alachlor Sensing, *Inorg. Chem.*, 2022, **61**, 9801–9807.

142 J. Li, P. Du, J. Chen, S. Huo, Z. Han, Y. Deng, Y. Chen and X. Lu, Dual-Channel Luminescent Signal Readout Strategy for Classifying Aprotic/Protic Polar Organic Medium and Naked-Eye Monitoring of Water in Organic Solvents, *Anal. Chem.*, 2020, **92**, 8974–8982.

143 Y. Dong, J. Cai, Q. Fang, X. You and Y. Chi, Dual-Emission of Lanthanide Metal-Organic Frameworks Encapsulating Carbon-Based Dots for Ratiometric Detection of Water in Organic Solvents, *Anal. Chem.*, 2016, **88**, 1748–1752.

144 X. Fu, R. Lv, J. Su, H. Li, B. Yang, W. Gu and X. Liu, A dual-emission nano-rod MOF equipped with carbon dots for visual detection of doxycycline and sensitive sensing of MnO_4^-, *RSC Adv.*, 2018, **8**, 4766–4772.

145 X. Luo, G. Huang, Y. Li, J. Guo, X. Chen, Y. Tan, W. Tang and Z. Li, Dual-modes of ratiometric fluorescent and smartphone-integrated colorimetric detection of glyphosate by carbon dots encapsulated porphyrin metal–organic frameworks, *Appl. Surf. Sci.*, 2022, **602**, 154368.

146 J. Hao, F. Liu, N. Liu, M. Zeng, Y. Song and L. Wang, Ratiometric fluorescent detection of Cu^{2+} with carbon dots chelated Eu-based metal-organic frameworks, *Sens. Actuators, B*, 2017, **245**, 641–647.

147 Y. Wang, J. He, M. Zheng, M. Qin and W. Wei, Dual-emission of Eu based metal-organic frameworks hybrids with carbon dots for ratiometric fluorescent detection of Cr(VI), *Talanta*, 2019, **191**, 519–525.

148 J. X. Wu and B. Yan, Visible detection of copper ions using a fluorescent probe based on red carbon dots and zirconium metal-organic frameworks, *Dalton Trans.*, 2017, **46**, 15080–15086.

149 M. Jin, Z. L. Mou, R. L. Zhang, S. S. Liang and Z. Q. Zhang, An efficient ratiometric fluorescence sensor based on metal-organic frameworks and quantum dots for highly selective detection of 6-mercaptopurine, *Biosens. Bioelectron.*, 2017, **91**, 162–168.

150 Y. Shu, Q. Ye, T. Dai, J. Guan, Z. Ji, Q. Xu and X. Hu, Incorporation of perovskite nanocrystals into lanthanide metal-organic frameworks with enhanced stability for ratiometric and visual sensing of mercury in aqueous solution, *J. Hazard. Mater.*, 2022, **430**, 128360.

151 P. Jia, K. Yang, J. Hou, Y. Cao, X. Wang and L. Wang, Ingenious dual-emitting Ru@UiO-66-NH$_2$ composite as ratiometric fluorescence sensor for detection of mercury in aqueous, *J. Hazard. Mater.*, 2021, **408**, 124469.

152 X. Sun, X. Xin, W. He, X. Cao and J. Shen, Tandem Forster resonance energy transfer induced visual ratiometric fluorescence sensing of tetracyclines based on zeolitic imidazolate framework-8 incorporated with carbon dots and safranine T, *Analyst*, 2022, **147**, 1152–1158.

153 X. Li, J. Luo, L. Deng, F. Ma and M. Yang, In Situ Incorporation of Fluorophores in Zeolitic Imidazolate Framework-8 (ZIF-8) for Ratio-Dependent Detecting a Biomarker of Anthrax Spores, *Anal. Chem.*, 2020, **92**, 7114–7122.

154 Y. Ma, G. Xu, F. Wei, Y. Cen, Y. Ma, Y. Song, X. Xu, M. Shi, S. Muhammad and Q. Hu, A dual-emissive fluorescent sensor fabricated by encapsulating quantum dots and carbon dots into metal–organic frameworks for the ratiometric detection of Cu^{2+} in tap water, *J. Mater. Chem. C*, 2017, **5**, 8566–8571.

155 R. Jalili, A. Khataee, M.-R. Rashidi and R. Luque, Dual-colored carbon dot encapsulated metal-organic framework for ratiometric detection of glutathione, *Sens. Actuators, B*, 2019, **297**, 126775.

156 L. Zhang, J. Chen, F. Zhang, J. Xu, N. Bi, J. Gou and L. Jia, Silicon quantum dots and MOFs hybrid multicolor fluorescent nanosensor for ultrasensitive and visual intelligent sensing of tetracycline, *Colloids Surf., A*, 2022, **652**, 129853.

157 X.-Y. Xu and B. Yan, Fabrication and application of a ratiometric and colorimetric fluorescent probe for Hg^{2+} based on dual-emissive metal–organic framework hybrids with carbon dots and Eu^{3+}, *J. Mater. Chem. C*, 2016, **4**, 1543–1549.

158 S.-J. Qin and B. Yan, Dual-emissive ratiometric fluorescent probe based on Eu^{3+}/C-dots@MOF hybrids for the biomarker diaminotoluene sensing, *Sens. Actuators, B*, 2018, **272**, 510–517.

159 J. X. Wu and B. Yan, A dual-emission probe to detect moisture and water in organic solvents based on green-Tb[3+] post-coordinated metal-organic frameworks with red carbon dots, *Dalton Trans.*, 2017, **46**, 7098–7105.

160 D. Zhang, Y. Zhou, J. Cuan and N. Gan, A lanthanide functionalized MOF hybrid for ratiometric luminescent detection of an anthrax biomarker, *CrystEngComm*, 2018, **20**, 1264–1270.

161 S. Qu, H. Chen, X. Zheng, J. Cao and X. Liu, Ratiometric fluorescent nanosensor based on water soluble carbon nanodots with multiple sensing capacities, *Nanoscale*, 2013, **5**, 5514–5518.

162 M. J. Krysmann, A. Kelarakis, P. Dallas and E. P. Giannelis, Formation Mechanism of Carbogenic Nanoparticles with Dual Photoluminescence Emission, *J. Am. Chem. Soc.*, 2011, **134**, 747–750.

163 E. Shuang, Q. X. Mao, J. H. Wang and X. W. Chen, Carbon dots with tunable dual emissions: from the mechanism to the specific imaging of endoplasmic reticulum polarity, *Nanoscale*, 2020, **12**, 6852–6860.

164 Y. Hu, Z. Yang, X. Lu, J. Guo, R. Cheng, L. Zhu, C. F. Wang and S. Chen, Facile synthesis of red dual-emissive carbon dots for ratiometric fluorescence sensing and cellular imaging, *Nanoscale*, 2020, **12**, 5494–5500.

165 C. Xia, M. Cao, J. Xia, G. Zhou, D. Jiang, D. Zhang, J. Wang and H. Li, An ultrafast responsive and sensitive ratiometric fluorescent pH nanoprobe based on label-free dual-emission carbon dots, *J. Mater. Chem. C*, 2019, **7**, 2563–2569.

166 L. Yuan, L. Liu, Y. Bai, J. Qin, M. Chen and F. Feng, A novel ratiometric fluorescent probe for detection of L-glutamic acid based on dual-emission carbon dots, *Talanta*, 2022, **245**, 123416.

167 K. Wang, X. Wang, X. Liu, E. Li, R. Zhao and S. Yang, Facile synthesis of dual emission carbon dots for the ratiometric fluorescent detection of 2,4,6-trinitrophenol and cell imaging, *J. Mol. Struct.*, 2022, **1263**, 133167.

168 Y. Wu, D. Qin, Z. Luo, S. Meng, G. Mo, X. Jiang and B. Deng, High Quantum Yield Boron and Nitrogen Codoped Carbon Quantum Dots with Red/Purple Emissions for Ratiometric Fluorescent IO_4^- Sensing and Cell Imaging, *ACS Sustainable Chem. Eng.*, 2022, **10**, 5195–5202.

169 L. Bao and S. Liu, A dual-emission polymer carbon nanoparticles for ratiometric and visual detection of pH value and bilirubin, *Spectrochim. Acta, Part A*, 2022, **267**, 120513.

170 W. Song, W. Duan, Y. Liu, Z. Ye, Y. Chen, H. Chen, S. Qi, J. Wu, D. Liu, L. Xiao, C. Ren and X. Chen, Ratiometric Detection of Intracellular Lysine and pH with One-Pot Synthesized Dual Emissive Carbon Dots, *Anal. Chem.*, 2017, **89**, 13626–13633.

171 P. P. Zhu, Z. Cheng, L. L. Du, Q. Chen and K. J. Tan, Synthesis of the Cu-Doped Dual-Emission Fluorescent Carbon Dots and Its Analytical Application, *Langmuir*, 2018, **34**, 9982–9989.

172 Y. Han, W. Yang, X. Luo, X. He, Y. Yu, C. Li, W. Tang, T. Yue and Z. Li, Cu^{2+}-Triggered Carbon Dots with Synchronous Response of Dual Emission for Ultrasensitive Ratiometric Fluorescence Determination of Thiophanate-Methyl Residues, *J. Agric. Food Chem.*, 2019, **67**, 12576–12583.

173 H. Wang, H. Xing, W. Liu, Y. Hao, L. Zhang, Z. Yang, Q. Hu, S. Shuang, C. Dong and X. Gong, Gadolinium-doped carbon dots as a ratiometric fluorometry and colorimetry dual-mode nano-sensor based on specific chelation for morin detection, *Sens. Actuators, B*, 2022, **352**, 130991.

174 J. Shangguan, D. He, X. He, K. Wang, F. Xu, J. Liu, J. Tang, X. Yang and J. Huang, Label-Free Carbon-Dots-Based Ratiometric Fluorescence pH Nanoprobes for Intracellular pH Sensing, *Anal. Chem.*, 2016, **88**, 7837–7843.

175 H. Zhang, Y. Gao, Y. Jiao, W. Lu, S. Shuang and C. Dong, Highly sensitive fluorescent carbon dots probe with ratiometric emission for the determination of ClO^-, *Analyst*, 2020, **145**, 2212–2218.

176 D. Chang, Z. Zhao, H. Shi, J. Feng, Y. Yang and L. Shi, Ratiometric fluorescent carbon dots for enantioselective sensing of L-lysine and pH discrimination in vivo and in vitro, *Sens. Actuators, B*, 2022, **362**, 131792.

177 G.-Y. Zou, L. Guo, S. Chen, N.-Z. Liu and Y.-L. Yu, Multifunctional ratiometric fluorescent sensing platform constructed by grafting various response groups on carbon dots with bromine active site for biosensing and bioimaging, *Sens. Actuators, B*, 2022, **357**, 131376.

178 X. Hu, Q. Zhang, X. Dai, J. Sun and F. Gao, Dual-Emission Carbonized Polymer Dots for Ratiometric pH Sensing, pH-Dependent Generation of Singlet Oxygen, and Imaging-Guided Dynamics Monitoring of Photodynamic Therapy, *ACS Appl. Bio Mater.*, 2021, **4**, 7663–7672.

179 Y. Ma, G. Xu, F. Wei, Y. Cen, X. Xu, M. Shi, X. Cheng, Y. Chai, M. Sohail and Q. Hu, One-Pot Synthesis of a Magnetic, Ratiometric Fluorescent Nanoprobe by Encapsulating Fe_3O_4 Magnetic Nanoparticles and Dual-Emissive Rhodamine B Modified Carbon Dots in Metal-Organic Framework for Enhanced HClO Sensing, *ACS Appl. Mater. Interfaces*, 2018, **10**, 20801–20805.

180 J. Zhao, M. Huang, L. Zhang, M. Zou, D. Chen, Y. Huang and S. Zhao, Unique Approach To Develop Carbon Dot-Based Nanohybrid Near-Infrared Ratiometric Fluorescent Sensor for the Detection of Mercury Ions, *Anal. Chem.*, 2017, **89**, 8044–8049.

181 H. Rao, W. Liu, K. He, S. Zhao, Z. Lu, S. Zhang, M. Sun, P. Zou, X. Wang, Q. Zhao, Y. Wang and T. Liu, Smartphone-Based Fluorescence Detection of Al^{3+} and H_2O Based on the Use of Dual-Emission Biomass Carbon Dots, *ACS Sustainable Chem. Eng.*, 2020, **8**, 8857–8867.

182 Y. Cui, R. Liu, F. Ye and S. Zhao, Single-excitation, dual-emission biomass quantum dots: preparation and application for ratiometric fluorescence imaging of coenzyme A in living cells, *Nanoscale*, 2019, **11**, 9270–9275.

183 Y. Gao, Y. Jiao, H. Zhang, W. Lu, Y. Liu, H. Han, X. Gong, L. Li, S. Shuang and C. Dong, One-step synthesis of a dual-emitting carbon dot-based ratiometric fluorescent probe for the visual assay of Pb^{2+} and PPi and development of a paper sensor, *J. Mater. Chem. B*, 2019, **7**, 5502–5509.

184 J. Liu, Y. Dong, Y. Ma, Y. Han, S. Ma, H. Chen and X. Chen, One-step synthesis of red/green dual-emissive carbon dots for ratiometric sensitive $ONOO^-$ probing and cell imaging, *Nanoscale*, 2018, **10**, 13589–13598.

185 L. Li, L. Shi, J. Jia, O. Eltayeb, W. Lu, Y. Tang, C. Dong and S. Shuang, Dual Photoluminescence Emission Carbon Dots for Ratiometric Fluorescent GSH Sensing and Cancer Cell Recognition, *ACS Appl. Mater. Interfaces*, 2020, **12**, 18250–18257.

186 P. Chen, H. Lao, F. Qu and J. You, Ratiometric captopril assay based on the recovery of the Bi(III)-quenched yellow fluorescence of dually emitting carbon nanodots, *New J. Chem.*, 2017, **41**, 2227–2230.

187 W. Ji, J. Yu, J. Cheng, L. Fu, Z. Zhang, B. Li, L. Chen and X. Wang, Dual-Emissive Near-Infrared Carbon Dot-Based Ratiometric Fluorescence Sensor for Lysozyme, *ACS Appl. Nano Mater.*, 2022, **5**, 1656–1663.

188 C. Liang, X. Xie, Q. Shi, J. Feng, D. Zhang and X. Huang, Nitrogen/sulfur-doped dual-emission carbon dots with tunable fluorescence for ratiometric sensing of ferric ions and cell membrane imaging, *Appl. Surf. Sci.*, 2022, **572**, 151447.

189 R. Dai and Y. Hu, Green/red dual emissive carbon dots for ratiometric fluorescence detection of acid red 18 in food, *Sens. Actuators, B*, 2022, **370**, 132420.

190 J. Wang, Q. Li, J. Zheng, Y. Yang, X. Liu and B. Xu, N, B-Codoping Induces High-Efficiency Solid-State Fluorescence and, Dual Emission of Yellow/Orange Carbon Dots, *ACS Sustainable Chem. Eng.*, 2021, **9**, 2224–2236.

191 Y. T. Gao, B. B. Chen, L. Jiang, J. Lv, S. Chang, Y. Wang, R. C. Qian, D. W. Li and M. E. Hafez, Dual-Emitting Carbonized Polymer Dots Synthesized at Room Temperature for Ratiometric Fluorescence Sensing of Vitamin B12, *ACS Appl. Mater. Interfaces*, 2021, **13**, 50228–50235.

192 L. Peng, M. Yang, M. Zhang and M. Jia, A ratiometric fluorescent sensor based on carbon dots for rapid determination of bisulfite in sugar, *Food Chem.*, 2022, **392**, 133265.

193 H. Lu, S. Xu and J. Liu, One Pot Generation of Blue and Red Carbon Dots in One Binary Solvent System for Dual Channel Detection of Cr^{3+} and Pb^{2+} Based on Ion Imprinted Fluorescence Polymers, *ACS Sens.*, 2019, **4**, 1917–1924.

194 L. Yu, L. Feng, L. Xiong, S. Li, S. Wang, Z. Wei and Y. Xiao, Portable visual assay of Bacillus anthracis biomarker based on ligand-functionalized dual-emission lanthanide metal-organic frameworks and smartphone-integrated mini-device, *J. Hazard. Mater.*, 2022, **434**, 128914.

195 X. Hu, Y. Guo, T. Wang, C. Liu, Y. Yang and G. Fang, A selectivity-enhanced ratiometric fluorescence imprinted sensor based on synergistic effect of covalent and non-covalent recognition units for ultrasensitive detection of ribavirin, *J. Hazard. Mater.*, 2022, **421**, 126748.

196 L. Yu, L. Feng, L. Xiong, S. Li, Q. Xu, X. Pan and Y. Xiao, Rational Design of Dual-Emission Lanthanide Metal-Organic Framework for Visual Alkaline Phosphatase Activity Assay, *ACS Appl. Mater. Interfaces*, 2021, **13**, 11646–11656.

197 X. Han, J. Liu, K. Yu, Y. Lu, W. Xiang, D. Zhao and Y. He, Water-Stable Eu_6-Cluster-Based fcu-MOF with Exposed Vinyl Groups for Ratiometric and Fluorescent Visual Sensing of Hydrogen Sulfide, *Inorg. Chem.*, 2022, **61**, 5067–5075.

198 J. J. Hu, Y. G. Li, H. R. Wen, S. J. Liu, Y. Peng and C. M. Liu, Stable Lanthanide Metal-Organic Frameworks with Ratiometric Fluorescence Sensing for Amino Acids and Tunable Proton Conduction and Magnetic Properties, *Inorg. Chem.*, 2022, **61**, 6819–6828.

199 Y. D. Xia, Y. Q. Sun, Y. Cheng, Y. Xia and X. B. Yin, Rational design of dual-ligand Eu-MOF for ratiometric fluorescence sensing Cu^{2+} ions in human serum to diagnose Wilson's disease, *Anal. Chim. Acta*, 2022, **1204**, 339731.

200 Y. Q. Sun, Y. Cheng and X. B. Yin, Dual-Ligand Lanthanide Metal-Organic Framework for Sensitive Ratiometric Fluorescence Detection of Hypochlorous Acid, *Anal. Chem.*, 2021, **93**, 3559–3566.

201 X. Liu, X. Li, S. Xu, S. Guo, Q. Xue and H. Wang, Efficient ratiometric fluorescence probe based on dual-emission luminescent lanthanide coordination polymer for amyloid β-peptide detection, *Sens. Actuators, B*, 2022, **352**, 131052.

202 P. Lv, Y. Cao, Z. Liu, R. Wang, B. Ye and G. Li, Dual luminescent lanthanide coordination polymers for ratiometric sensing and efficient removal of Hg^{2+}, *Anal. Methods*, 2020, **12**, 91–96.

203 W. Shi, S. Zhang, Y. Wang, Y. D. Xue and M. Chen, Preparation of dual-ligands Eu-MOF nanorods with dual fluorescence emissions for highly sensitive and selective ratiometric/visual fluorescence sensing phosphate, *Sens. Actuators, B*, 2022, **367**, 132008.

204 X. Zhu, X. Wu, J. Liu, L. Zou, B. Ye and G. Li, Lanthanide coordination polymers used for fluorescent ratiometric sensing of H_2O_2 and glucose, *Inorg. Chem. Commun.*, 2022, **144**, 109849.

205 L. Han, S. G. Liu, Y. Z. Yang, Y. Z. Fan, J. Zhou, X. Y. Zhang, N. B. Li and H. Q. Luo, A lanthanide coordination polymer as a ratiometric fluorescent probe for rapid and visual sensing of phosphate based on the target-triggered competitive effect, *J. Mater. Chem. C*, 2020, **8**, 13063–13071.

206 B. Li, W. Wang, Z. Hong, E. M. El-Sayed and D. Yuan, Ratiometric fluorescence detection of trace water in an organic solvent based on bimetallic lanthanide metal-organic frameworks, *Chem. Commun.*, 2019, **55**, 6926–6929.

207 J. Li, C. Gong, Z. Li, R. Yao, P. Huo, B. Deng, G. Liu and S. Pu, A self-assembly lanthanide nanoparticle for ratiometric fluorescence determination of alkaline phosphatase activity, *J. Photochem. Photobiol., A*, 2022, **432**, 114054.

208 L. Guo, X. Tian, C. Zhu, S. Hussain, J. Han and H. Li, A dual-emission fluorescent ratiometric probe based on bimetallic lanthanide complex interacted in nanoclay for monitoring of food spoilage, *Sens. Actuators, B*, 2022, **366**, 131992.

209 H. Li, W. Han, R. Lv, A. Zhai, X. L. Li, W. Gu and X. Liu, Dual-Function Mixed-Lanthanide Metal-Organic Framework for Ratiometric Water Detection in Bioethanol and Temperature Sensing, *Anal. Chem.*, 2019, **91**, 2148–2154.

210 X. Liu, W. Fu and E. Bouwman, One-step growth of lanthanoid metal-organic framework (MOF) films under solvothermal conditions for temperature sensing, *Chem. Commun.*, 2016, **52**, 6926–6929.

211 L. Li, J. Cheng, Z. Liu, L. Song, Y. You, X. Zhou and W. Huang, Ratiometric Luminescent Sensor of Picric Acid Based on the Dual-Emission Mixed-Lanthanide Coordination Polymer, *ACS Appl. Mater. Interfaces*, 2018, **10**, 44109–44115.

212 N. W. Hao Guo, L. Peng, Y. Chen, Y. Liu, C. Li, H. Zhang and W. Yang, A novel ratiometric fluorescence sensor based on lanthanide-functionalized MOF for Hg^{2+} detection, *Talanta*, 2022, **250**, 123710.

213 X. Zheng, R. Fan, Y. Song, A. Wang, K. Xing, X. Du, P. Wang and Y. Yang, A highly sensitive turn-on ratiometric luminescent probe based on postsynthetic modification of Tb^{3+}@Cu-MOF for H_2S detection, *J. Mater. Chem. C*, 2017, **5**, 9943–9951.

214 J. Xiao, L. Song, M. Liu, X. Wang and Z. Liu, Intriguing pH-modulated Luminescence Chameleon System based on Postsynthetic Modified Dual-emitting Eu^{3+}@Mn-MOF and Its Application for Histidine Chemosensor, *Inorg. Chem.*, 2020, **59**, 6390–6397.

215 Y. Zhou and B. Yan, A responsive MOF nanocomposite for decoding volatile organic compounds, *Chem. Commun.*, 2016, **52**, 2265–2268.

216 Y. N. Zeng, H. Q. Zheng, J. F. Gu, G. J. Cao, W. E. Zhuang, J. D. Lin, R. Cao and Z. J. Lin, Dual-Emissive Metal-Organic Framework as a Fluorescent "Switch" for Ratiometric Sensing of Hypochlorite and Ascorbic Acid, *Inorg. Chem.*, 2019, **58**, 13360–13369.

217 Y. F. Xia, G. M. Bao, X. X. Peng, X. Y. Wu, H. F. Lu, Y. F. Zhong, W. Li, J. X. He, S. Y. Liu, Q. Fan, S. H. Li, W. Xiao and H. Q. Yuan, A highly water-stable dual-emission fluorescent probe based on Eu^{3+}-loaded MOF for the simultaneous detection and quantification of Fe^{3+} and Al^{3+} in swine wastewater, *Anal. Chim. Acta*, 2022, **1221**, 340115.

218 X. Zhang, Q. Hu, T. Xia, J. Zhang, Y. Yang, Y. Cui, B. Chen and G. Qian, Turn-on and Ratiometric Luminescent Sensing of Hydrogen Sulfide Based on Metal-Organic Frameworks, *ACS Appl. Mater. Interfaces*, 2016, **8**, 32259–32265.

219 J. N. Hao and B. Yan, A dual-emitting 4d-4f nanocrystalline metal-organic framework as a self-calibrating luminescent sensor for indoor formaldehyde pollution, *Nanoscale*, 2016, **8**, 12047–12053.

220 X.-M. Du, Q. Wang, Q. Liu, D. Ning, B. Zhao, Y. Li and W.-J. Ruan, A dual-emissive MOF for the simultaneous detection of tetrachlorobenzoquinone isomers in their mixtures, *J. Mater. Chem. C*, 2019, **7**, 8626–8633.

221 J. F. Feng, S. Y. Gao, T. F. Liu, J. Shi and R. Cao, Preparation of Dual-Emitting Ln@UiO-66-Hybrid Films via Electrophoretic Deposition for Ratiometric Temperature Sensing, *ACS Appl. Mater. Interfaces*, 2018, **10**, 6014–6023.

222 Y. Liu, X. Xu, H. Lu and B. Yan, Dual-emission ratiometric fluorescent probe-based lanthanide-functionalized hydrogen-bonded organic framework for the visual detection of methylamine, *J. Mater. Chem. C*, 2022, **10**, 1212–1219.

223 L. Song, F. Tian and Z. Liu, Lanthanide doped metal-organic frameworks as a ratiometric fluorescence biosensor for visual and ultrasensitive detection of serotonin, *J. Solid State Chem.*, 2022, **312**, 123231.

224 J. F. Feng, T. F. Liu, J. Shi, S. Y. Gao and R. Cao, Dual-Emitting UiO-66(Zr&Eu) Metal-Organic Framework Films for Ratiometric Temperature Sensing, *ACS Appl. Mater. Interfaces*, 2018, **10**, 20854–20861.

225 J. Yao, Z. Xie, X. Zeng, L. Wang and T. Yue, Bimetallic Eu/Fe-MOFs ratiometric fluorescent nanoenzyme for selective cholesterol detection in biological serum: Synthesis, characterization, mechanism and DFT calculations, *Sens. Actuators, B*, 2022, **354**, 130760.

226 Y. Zhou, B. Yan and F. Lei, Postsynthetic lanthanide functionalization of nanosized metal-organic frameworks for highly sensitive ratiometric luminescent thermometry, *Chem. Commun.*, 2014, **50**, 15235–15238.

227 H. Fei, S. Pullen, A. Wagner, S. Ott and S. M. Cohen, Functionalization of robust Zr(iv)-based metal-organic framework films via a postsynthetic ligand exchange, *Chem. Commun.*, 2015, **51**, 66–69.

228 K. K. Tanabe, C. A. Allen and S. M. Cohen, Photochemical activation of a metal-organic framework to reveal functionality, *Angew. Chem., Int. Ed.*, 2010, **49**, 9730–9733.

229 Y. Zhou and B. Yan, Ratiometric detection of temperature using responsive dual-emissive MOF hybrids, *J. Mater. Chem. C*, 2015, **3**, 9353–9358.

230 X.-Y. Xu and B. Yan, Eu(iii)-functionalized ZnO@MOF heterostructures: integration of pre-concentration and efficient charge transfer for the fabrication of a ppb-level sensing platform for volatile aldehyde gases in vehicles, *J. Mater. Chem. A*, 2017, **5**, 2215–2223.

231 X. B. Yin, Y. Q. Sun, H. Yu, Y. Cheng and C. Wen, Design and Multiple Applications of Mixed-Ligand Metal-Organic

Frameworks with Dual Emission, *Anal. Chem.*, 2022, **94**, 4938–4947.

232 X. Wang, Y. Wang, X. Wang, C. Hu, X. Wu, W. Guo, S. Zhen, C. Huang and Y. Li, Dual-ligand two-dimensional Europium-organic gels nanosheets for ratiometric fluorescence detecting anthrax spore biomarker, *Chem. Eng. J.*, 2022, **435**, 134912.

233 X. Wang, C. Hu, X. Wang, Z. Luo, S. Zhen, L. Zhan, C. Huang and Y. Li, Facile synthesis of dual-ligand terbium-organic gels as ratiometric fluorescence probes for efficient mercury detection, *J. Hazard. Mater.*, 2022, **436**, 129080.

234 X. Wang, Z. Jiang, C. Yang, S. Zhen, C. Huang and Y. Li, Facile synthesis of binary two-dimensional lanthanide metal-organic framework nanosheets for ratiometric fluorescence detection of mercury ions, *J. Hazard. Mater.*, 2022, **423**, 126978.

235 V. A. Vlaskin, N. Janssen, J. van Rijssel, R. Beaulac and D. R. Gamelin, Tunable dual emission in doped semiconductor nanocrystals, *Nano Lett.*, 2010, **10**, 3670–3674.

236 L. Lu, G. Yang and Y. Xia, From pair to single: sole fluorophore for ratiometric sensing by dual-emitting quantum dots, *Anal. Chem.*, 2014, **86**, 6188–6191.

237 W. Gu, S. Gong, Y. Zhou and Y. Xia, Ratiometric sensing of metabolites using dual-emitting ZnS: Mn^{2+} quantum dots as sole luminophore via surface chemistry design, *Biosens. Bioelectron.*, 2017, **90**, 487–493.

238 M. Manna, S. Pramanik and S. Bhandari, Surface Modification of Dual-Emitting Quantum Dot Complex by Ionic Liquid for Bright and Stable White-Light Emission, *ACS Appl. Nano Mater.*, 2022, **5**, 11906–11911.

239 S. Bhandari, S. Roy, S. Pramanik and A. Chattopadhyay, Double channel emission from a redox active single component quantum dot complex, *Langmuir*, 2015, **31**, 551–561.

240 M. Manna, S. Roy, S. Bhandari and A. Chattopadhyay, A dual-emitting quantum dot complex nanoprobe for ratiometric and visual detection of Hg^{2+} and Cu^{2+} ions, *J. Mater. Chem. C*, 2020, **8**, 6972–6976.

241 M. Manna, S. Bhandari and A. Chattopadhyay, Recognition and ratiometric visual sensing of long-chain unsaturated fatty acids by a white-light-emitting quantum-dot complex, *J. Mater. Chem. C*, 2021, **9**, 13810–13817.

242 S. Wang, L. Yu, Z. Wei, Q. Xu, W. Zhou and Y. Xiao, Dual-response ratiometric fluorescence based on ligand-functionalized $CsPbBr_3$ perovskite quantum dots for sensitive detection of trace water in edible oils, *Sens. Actuators, B*, 2022, **366**, 132010.

243 S. Pramanik, S. Bhandari, U. N. Pan, S. Roy and A. Chattopadhyay, A White Light-Emitting Quantum Dot Complex for Single Particle Level Interaction with Dopamine Leading to Changes in Color and Blinking Profile, *Small*, 2018, **14**, e1800323.

244 M. Manna, S. Roy, S. Bhandari and A. Chattopadhyay, A Ratiometric and Visual Sensing of Phosphate by White Light Emitting Quantum Dot Complex, *Langmuir*, 2021, **37**, 5506–5512.

245 M. Tang, B. Zhu, Y. Qu, Z. Jin, S. Bai, F. Chai, L. Chen, C. Wang and F. Qu, Fluorescent silicon nanoparticles as dually emissive probes for copper(ɪɪ) and for visualization of latent fingerprints, *Mikrochim. Acta*, 2019, **187**, 65.

246 L. Li, J. Chen, R. Jin, Y. Yan, Z. Song, J. Wang, X. Wang, Q. Zhang and C. Zhang, 2-Mercaptobenzothiazole-supported ratiometric fluorescent copper nanoclusters for activatable GSH sensing to drive tumor recognition, *Colloids Surf., B*, 2022, **217**, 112698.

247 Y. Rong, M. M. Hassan, Q. Ouyang, L. Wang, T. Jiao and Q. Chen, Ratiometric upconversion fluorometric turn-off nanosensor for quantification of furfural in foods, *Sens. Actuators, B*, 2022, **350**, 130843.

248 Y. Cao, X. Wang, T. Feng, Z. Li, C. Xue and J. Xu, Ratiometric fluorescent nanosystem based on upconversion nanoparticles for histamine determination in seafood, *Food Chem.*, 2022, **390**, 133194.

249 L. Pu, M. Xia, P. Sun and Y. Zhang, Ratiometric fluorescence determination of alkaline phosphatase activity based on dual emission of bovine serum albumin-stabilized gold nanoclusters and the inner filter effect, *Analyst*, 2021, **146**, 943–948.

250 P. Zhao, K. He, Y. Han, Z. Zhang, M. Yu, H. Wang, Y. Huang, Z. Nie and S. Yao, Near-infrared dual-emission quantum dots-gold nanoclusters nanohybrid via co-template synthesis for ratiometric fluorescent detection and bioimaging of ascorbic acid in vitro and in vivo, *Anal. Chem.*, 2015, **87**, 9998–10005.

251 L. Zhang, D. Wang, H. Huang, L. Liu, Y. Zhou, X. Xia, K. Deng and X. Liu, Preparation of Gold-Carbon Dots and Ratiometric Fluorescence Cellular Imaging, *ACS Appl. Mater. Interfaces*, 2016, **8**, 6646–6655.

252 H. Lu and S. Xu, Visualizing BPA by molecularly imprinted ratiometric fluorescence sensor based on dual emission nanoparticles, *Biosens. Bioelectron.*, 2017, **92**, 147–153.

253 X. Niu, H. Gao and J. Du, $CsPbBr_3$ Perovskite Nanocrystals Decorated with Cu Nanoclusters for Ratiometric Detection of Glucose, *ACS Appl. Nano Mater.*, 2022, **5**, 2350–2357.

254 Z. Sun, Y. Gao, Z. Niu, H. Pan, X. Xu, W. Zhang and X. Zou, Programmable-Printing Paper-Based Device with a MoS_2 NP and Gmp/Eu-Cit Fluorescence Couple for Ratiometric Tetracycline Analysis in Various Natural Samples, *ACS Sens.*, 2021, **6**, 4038–4047.

255 Y. Sang, K. Wang, X. Kong, F. Cheng, C. Zhou and W. Li, Color-multiplexing europium doped carbon dots for highly selective and dosage-sensitive cascade visualization of tetracycline and Al^{3+}, *Sens. Actuators, B*, 2022, **362**, 131780.

256 X. An, X. Zhu, J. Liu, L. Zou, G. Li and B. Ye, Ratiometric fluorescence detection of ciprofloxacin using the terbium-based coordination polymers, *Spectrochim. Acta, Part A*, 2022, **269**, 120775.

257 J. Zhang, Z. Bao, J. Qian, H. Zhou and K. Zhang, Copper doped zinc sulfide quantum dots as ratiometric fluorescent probes for rapid and specific detection of tetra-

cycline residues in milk, *Anal. Chim. Acta*, 2022, **1216**, 339991.

258 W. Yang, X. Zheng, F. Gao, H. Li, B. Fu, D. Y. Guo, F. Wang and Q. Pan, CdTe QDs@ZIF-8 composite-based recyclable ratiometric fluorescent sensor for rapid and sensitive detection of chlortetracycline, *Spectrochim. Acta, Part A*, 2022, **270**, 120785.

259 Y. Li, Y. Wang, P. Du, L. Zhang, Y. Liu and X. Lu, Fabrication of carbon dots@hierarchical mesoporous ZIF-8 for simultaneous ratiometric fluorescence detection and removal of tetracycline antibiotics, *Sens. Actuators, B*, 2022, **358**, 131526.

260 K. Yang, P. Jia, J. Hou, S. Zhao and L. Wang, An ingenious turn-on ratiometric fluorescence sensor for sensitive and visual detection of tetracyclines, *Food Chem.*, 2022, **396**, 133693.

261 L. Li, D. Lin, S. Xu, L. Yang, S. Yu and C. Jiang, Ratiometric fluorescent sensor for shutter-speedy and ultra-sensitive monitoring of antibiotic utilizing multiple fluorescent devices, *Sens. Actuators, B*, 2022, **363**, 131819.

262 Y. Zhuang, B. Lin, Y. Yu, Y. Wang, L. Zhang, Y. Cao and M. Guo, A ratiometric fluorescent probe based on sulfur quantum dots and calcium ion for sensitive and visual detection of doxycycline in food, *Food Chem.*, 2021, **356**, 129720.

263 M. Li, Z. J. Qian, C. F. Peng, X. L. Wei and Z. P. Wang, Ultrafast Ratiometric Detection of Aflatoxin B1 Based on Fluorescent beta-CD@Cu Nanoparticles and Pt^{2+} Ions, *ACS Appl. Bio Mater.*, 2022, **5**, 285–294.

264 F. Yu, T. Du, Y. Wang, C. Li, Z. Qin, H. Jiang and X. Wang, Ratiometric fluorescence sensing of $UiO-66-NH_2$ toward hypochlorite with novel dual emission in vitro and in vivo, *Sens. Actuators, B*, 2022, **353**, 131032.

265 Y. Qin, Y. Bai, P. Huang and F.-Y. Wu, Dual-Emission Carbon Dots for Ratiometric Fluorescent Water Sensing, Relative Humidity Sensing, and Anticounterfeiting Applications, *ACS Appl. Nano Mater.*, 2021, **4**, 10674–10681.

266 J. Othong, J. Boonmak, F. Kielar and S. Youngme, Dual Function Based on Switchable Colorimetric Luminescence for Water and Temperature Sensing in Two-Dimensional Metal-Organic Framework Nanosheets, *ACS Appl. Mater. Interfaces*, 2020, **12**, 41776–41784.

267 S. Li, L. Yu, L. Xiong and Y. Xiao, Ratiometric fluorescence and chromaticity dual-readout assay for β-glucuronidase activity based on luminescent lanthanide metal-organic framework, *Sens. Actuators, B*, 2022, **355**, 131282.

268 W. Mao, L. Dai, L. Hu, J. Song, T. Huang and M. Wang, Dual-channel fluorescent imaging of reactive oxygen species in living cells based on Ce(III) modified quantum dots with oxidation triggered phosphatase-like activity, *Sens. Actuators, B*, 2022, **367**, 132178.

269 J. Wen, N. Li, D. Li, M. Zhang, Y. Lin, Z. Liu, X. Lin and L. Shui, Cesium-Doped Graphene Quantum Dots as Ratiometric Fluorescence Sensors for Blood Glucose Detection, *ACS Appl. Nano Mater.*, 2021, **4**, 8437–8446.

270 A. Molla, H. Lee, Y. Ju, J. Choi and J. Kim, Ratiometric fluorescence probe based on monochromatic dual-emission carbon nanodots with fluorescence spectral change, *Dyes Pigm.*, 2022, **197**, 109883.

271 J. W. Liu, Y. Luo, Y. M. Wang, L. Y. Duan, J. H. Jiang and R. Q. Yu, Graphitic Carbon Nitride Nanosheets-Based Ratiometric Fluorescent Probe for Highly Sensitive Detection of H_2O_2 and Glucose, *ACS Appl. Mater. Interfaces*, 2016, **8**, 33439–33445.

272 Z. Quan, F. Xue, H. Li, Z. Chen, L. Wang, H. Zhu, C. Pang and H. He, A bioinspired ratiometric fluorescence probe based on cellulose nanocrystal-stabilized gold nanoclusters for live-cell and zebrafish imaging of highly reactive oxygen species, *Chem. Eng. J.*, 2022, **431**, 133954.

273 L. Yu, L. Feng, L. Xiong, S. Li, Q. Xu, X. Pan and Y. Xiao, Multifunctional nanoscale lanthanide metal-organic framework based ratiometric fluorescence paper microchip for visual dopamine assay, *Nanoscale*, 2021, **13**, 11188–11196.

274 X. Wei, T. Ji, S. Zhang, Z. Xue, C. Lou, M. Zhang, S. Zhao, H. Liu, X. Guo, B. Yang and J. Chen, Cerium-terephthalic acid metal-organic frameworks for ratiometric fluorescence detecting and scavenging. OH from fuel combustion gas, *J. Hazard. Mater.*, 2022, **439**, 129603.

275 F. Yang, D. Lin, L. Pan, J. Zhu, J. Shen, L. Yang and C. Jiang, Portable Smartphone Platform Based on a Single Dual-Emissive Ratiometric Fluorescent Probe for Visual Detection of Isopropanol in Exhaled Breath, *Anal. Chem.*, 2021, **93**, 14506–14513.

276 C. Wang, M. Niu, W. Wang, L. Su, H. Feng, H. Lin, X. Ge, R. Wu, Q. Li, J. Liu, H. Yang and J. Song, In Situ Activatable Ratiometric NIR-II Fluorescence Nanoprobe for Quantitative Detection of H_2S in Colon Cancer, *Anal. Chem.*, 2021, **93**, 9356–9363.

277 J. Ma, Z. Lu, C. Li, Y. Luo, Y. E. Shi, P. Alam, J. W. Y. Lam, Z. Wang and B. Z. Tang, Fluorescence ratiometric assay for discriminating GSH and Cys based on the composites of $UiO-66-NH_2$ and Cu nanoclusters, *Biosens. Bioelectron.*, 2022, **215**, 114582.

278 L. Meng, C. Lan, Z. Liu, N. Xu and Y. Wu, A novel ratiometric fluorescence probe for highly sensitive and specific detection of chlorotetracycline among tetracycline antibiotics, *Anal. Chim. Acta*, 2019, **1089**, 144–151.

279 H. K. Sadhanala, S. Aryal, K. Sharma, Z. Orpaz, S. Michaeli and A. Gedanken, Nitrogen-doped carbon dots as a highly selective and sensitive fluorescent probe for sensing Mg^{2+} ions in aqueous solution, and their application in the detection and imaging of intracellular Mg^{2+} ions, *Sens. Actuators, B*, 2022, **366**, 131958.

280 S. Paydar, F. Feizi, M. Shamsipur, A. Barati, N. Chehri, A. Taherpour and M. Jamshidi, An ideal ratiometric fluorescent probe provided by the surface modification of carbon dots for the determination of Pb^{2+}, *Sens. Actuators, B*, 2022, **369**, 132243.

281 X. Hu, X. Zhang, H. Cao and Y. Huang, Cu-based metal-organic frameworks-derived copper nanoclusters with

tunable emission for ratiometric pH sensing, *Sens. Actuators, B*, 2022, **353**, 131130.

282 L. Yu, H. Chen, J. Yue, X. Chen, M. Sun, H. Tan, A. M. Asiri, K. A. Alamry, X. Wang and S. Wang, Metal-Organic Framework Enhances Aggregation-Induced Fluorescence of Chlortetracycline and the Application for Detection, *Anal. Chem.*, 2019, **91**, 5913–5921.

283 Y. Si, Y. Li, G. Yang, S. Zhang, L. Yang, W. Dai and H. Wang, Zeolitic imidazolate framework-8 for ratiometric fluorescence sensing tetracyclines in environmental water based on AIE effects, *Anal. Chim. Acta*, 2022, **1199**, 339576.

284 H. Zhang, Q. Nian, H. Dai, X. Wan and Q. Xu, A nano-fiber-mat-based solid-phase sensor for sensitive ratio-metric fluorescent sensing and fine visual colorimetric detection of tetracycline, *Food Chem.*, 2022, **395**, 133597.

285 L. Zhang, H. Xing, W. Liu, Z. Wang, Y. Hao, H. Wang, W. Dong, Y. Liu, S. Shuang, C. Dong and X. Gong, 11-Mercaptoundecanoic Acid-Functionalized Carbon Dots As a Ratiometric Optical Probe for Doxorubicin Detection, *ACS Appl. Nano Mater.*, 2021, **4**, 13734–13746.

286 K. K. Chan, S. H. K. Yap, D. Giovanni, T. C. Sum and K.-T. Yong, Water-stable Perovskite Quantum Dots-based FRET Nanosensor for the Detection of Rhodamine 6G in Water, Food, and Biological Samples, *Microchem. J.*, 2022, **180**, 107624.

287 H. Lu, S. Quan and S. Xu, Highly Sensitive Ratiometric Fluorescent Sensor for Trinitrotoluene Based on the Inner Filter Effect between Gold Nanoparticles and Fluorescent Nanoparticles, *J. Agric. Food Chem.*, 2017, **65**, 9807–9814.

288 H. R. Nan, Y. H. Liu, W. J. Gong, H. B. Peng, Y. Q. Wang, Z. B. Zhang and X. H. Cao, An inner-filter-effect based ratiometric fluorescent sensor for the detection of uranyl ions in real samples, *Anal. Methods*, 2022, **14**, 532–540.

289 S. Chu, H. Wang, X. Ling, S. Yu, L. Yang and C. Jiang, A Portable Smartphone Platform Using a Ratiometric Fluorescent Paper Strip for Visual Quantitative Sensing, *ACS Appl. Mater. Interfaces*, 2020, **12**, 12962–12971.

290 D. Wei, Y. Wang, N. Zhu, J. Xiao, X. Li, T. Xu, X. Hu, Z. Zhang and D. Yin, A Lab-in-a-Syringe Device Integrated with a Smartphone Platform: Colorimetric and Fluorescent Dual-Mode Signals for On-Site Detection of Organophosphorus Pesticides, *ACS Appl. Mater. Interfaces*, 2021, **13**, 48643–48652.

291 X. Yan, H. Li, X. Han and X. Su, A ratiometric fluorescent quantum dots based biosensor for organophosphorus pesticides detection by inner-filter effect, *Biosens. Bioelectron.*, 2015, **74**, 277–283.

292 H. Lu, C. Yu, S. Quan and S. Xu, A novel dual response ratiometric fluorescent probe for the determination of H_2O_2 and glucose via etching of silver nanoparticles, *Analyst*, 2019, **144**, 1153–1158.

293 P. Du, Q. Niu, J. Chen, Y. Chen, J. Zhao and X. Lu, "Switch-On" Fluorescence Detection of Glucose with High Specificity and Sensitivity Based on Silver Nanoparticles

294 H. Lu, C. Yu, Y. Zhang and S. Xu, Efficient core shell struc-tured dual response ratiometric fluorescence probe for determination of H_2O_2 and glucose via etching of silver nanoprisms, *Anal. Chim. Acta*, 2019, **1048**, 178–185.

295 S. D. Hiremath, M. Banerjee and A. Chatterjee, Review of 2D MnO_2 Nanosheets as FRET-Based Nanodot Fluorescence Quenchers in Chemosensing Applications, *ACS Appl. Nano Mater.*, 2022, **5**, 17373–17412.

296 H. Lu and S. Xu, CDs-MnO_2-TPPS Ternary System for Ratiometric Fluorescence Detection of Ascorbic Acid and Alkaline Phosphatase, *ACS Omega*, 2021, **6**, 16565–16572.

297 Y. Hu, Y. C. Fan, X. H. Jiang, L. M. Zhou and Z. J. Cheng, A ratiometric fluorescent sensing of proanthocyanidins by MnO_2 nanosheets simultaneously tuning the photo-luminescence of Au/AgNCs and thiamine, *Talanta*, 2021, **234**, 122607.

298 J. Zhang, R. Chen, Q. Chen, Y. Hu, S. Pan and X. Hu, Ratiometric fluorescent probe for ascorbic acid detection based on MnO_2 nanosheets, gold nanoclusters and thia-mine, *Colloids Surf., A*, 2021, **622**, 126605.

299 H. Li, Z. Wang, J. Zhao, Y. Guan and Y. Liu, Dual Colorimetric and Ratiometric Fluorescent Responses for the Determination of Glutathione Based on Fluorescence Quenching and Oxidase-Like Activity of MnO_2 Nanosheets, *ACS Sustainable Chem. Eng.*, 2020, **8**, 16136–16142.

300 M. Shi, Y. Cen, G. Xu, F. Wei, X. Xu, X. Cheng, Y. Chai, M. Sohail and Q. Hu, Ratiometric fluorescence monitor-ing of alpha-glucosidase activity based on oxidase-like property of MnO_2 nanosheet and its application for inhibitor screening, *Anal. Chim. Acta*, 2019, **1077**, 225–231.

301 C. Sun, N. Liu, J. Liu, T. Lv, C. Yang, C. Su, N. Zhang, H. Li and X. Yan, MnO_2 nanosheets anchored gold nanoclusters@ZIF-8 based ratiometric fluorescence sensor for monitoring chlorpyrifos degradation, *Sens. Actuators, B*, 2023, **375**, 132924.

302 F. Bai, H. Wang, L. Lin and L. Zhao, A ratiometric fluo-rescence platform composed of MnO_2 nanosheets and nitrogen, chlorine co-doped carbon dots and its logic gate performance for glutathione determination, *New J. Chem.*, 2022, **46**, 1972–1983.

303 Y. Cao, J. Liu, L. Zou, B. Ye and G. Li, Ratiometric fluo-rescence sensing of glutathione by using the oxidase-mimicking activity of MnO_2 nanosheet, *Anal. Chim. Acta*, 2021, **1145**, 46–51.

304 H. Li, R. Zou, C. Su, N. Zhang, Q. Wang, Y. Zhang, T. Zhang, C. Sun and X. Yan, Ratiometric fluorescent hydrogel for point-of-care monitoring of organopho-sphorus pesticide degradation, *J. Hazard. Mater.*, 2022, **432**, 128660.

305 Q. Yang, C. Li, J. Li, M. Arabi, X. Wang, H. Peng, H. Xiong, J. Choo and L. Chen, Multi-emitting fluorescence sensor of MnO_2–OPD–QD for the multiplex and visual detection

of ascorbic acid and alkaline phosphatase, *J. Mater. Chem. C*, 2020, **8**, 5554–5561.

306 B. Li, M. Wang and J. Zhao, MnO_2 nanosheet-assisted ratiometric fluorescent sensor for ascorbic acid based on Pyronin Y and thiamine, *Microchem. J.*, 2022, **181**, 107835.

307 X. Hu, X. Liu, X. Zhang, H. Cao and Y. Huang, MnO_2 nanowires tuning of photoluminescence of alloy Cu/Ag NCs and thiamine enables a ratiometric fluorescent sensing of glutathione, *Sens. Actuators, B*, 2019, **286**, 476–482.

308 Q. Yang, X. Wang, H. Peng, M. Arabi, J. Li, H. Xiong, J. Choo and L. Chen, Ratiometric fluorescence and colorimetry dual-mode assay based on manganese dioxide nanosheets for visual detection of alkaline phosphatase activity, *Sens. Actuators, B*, 2020, **302**, 127176.

309 D. Fan, C. Shang, W. Gu, E. Wang and S. Dong, Introducing Ratiometric Fluorescence to MnO_2 Nanosheet-Based Biosensing: A Simple, Label-Free Ratiometric Fluorescent Sensor Programmed by Cascade Logic Circuit for Ultrasensitive GSH Detection, *ACS Appl. Mater. Interfaces*, 2017, **9**, 25870–25877.

310 T. Yao, A. Liu, Y. Liu, M. Wei, W. Wei and S. Liu, Ratiometric fluorescence sensor for organophosphorus pesticide detection based on opposite responses of two fluorescence reagents to MnO_2 nanosheets, *Biosens. Bioelectron.*, 2019, **145**, 111705.

311 Q. Fu, X. Zhou, M. Wang and X. Su, Nanozyme-based sensitive ratiometric fluorescence detection platform for glucose, *Anal. Chim. Acta*, 2022, **1216**, 339993.

312 X. P. Zhang Wang Xu Yang Shu and J. H. Wang, CoOOH nanosheets ensure ratiometric fluorescence assay of acetylcholinesterase, *Talanta*, 2022, **249**, 123664.

313 C. Yao, G. Zhang, Y. Guan, T. Yang, R. Hu and Y. Yang, Modulation of inner filter effect between persistent luminescent particles and 2, 3-diaminophenazine for ratiometric fluorescent assay of ascorbic acid and ascorbate oxidase activity, *Spectrochim. Acta, Part A*, 2022, **280**, 121564.

314 C. X. Liao, B. Z. Jia, H. Wang, Y. M. Sun, X. Y. Xu, X. Q. Wei, Y. D. Shen, H. T. Lei, Z. L. Xu and L. Luo, Prussian blue nanoparticles-enabled sensitive and accurate ratiometric fluorescence immunoassay for histamine, *Food Chem.*, 2021, **376**, 131907.

315 Y. Tang, C. Huang, H. Tang and M. Guo, Nitrogen-doped carbonized polymer dots activated by alkalinity of arginine for multicolor multi-platform sensor, *Colloids Surf., B*, 2022, **216**, 112517.

316 C. F. Miao, X. Z. Guo, X. T. Zhang, Y. N. Lin, W. D. Han, Z. J. Huang and S. H. Weng, Ratiometric fluorescence assay based on carbon dots and Cu^{2+}-catalyzed oxidation of O-phenylenediamine for the effective detection of deferasirox, *RSC Adv.*, 2021, **11**, 34525–34532.

317 X. Xu, Y. Cen, G. Xu, F. Wei, M. Shi and Q. Hu, A ratiometric fluorescence probe based on carbon dots for discriminative and highly sensitive detection of acetylcholin-

esterase and butyrylcholinesterase in human whole blood, *Biosens. Bioelectron.*, 2019, **131**, 232–236.

318 Y. Zhu, X. Tong, Q. Wei, G. Cai, Y. Cao, C. Tong, S. Shi and F. Wang, 3D origami paper-based ratiometric fluorescent microfluidic device for visual point-of-care detection of alkaline phosphatase and butyrylcholinesterase, *Biosens. Bioelectron.*, 2022, **196**, 113691.

319 H. Wang, J. Rui, W. Xiao, Y. Peng, Z. Peng and P. Qiu, Enzyme-free ratiometric fluorescence and colorimetric dual read-out assay for glyphosate with ultrathin g-C_3N_4 nanosheets, *Microchem. J.*, 2022, **180**, 107587.

320 T. Liu, S. Chen, K. Ruan, S. Zhang, K. He, J. Li, M. Chen, J. Yin, M. Sun, X. Wang, Y. Wang, Z. Lu and H. Rao, A handheld multifunctional smartphone platform integrated with 3D printing portable device: On-site evaluation for glutathione and azodicarbonamide with machine learning, *J. Hazard. Mater.*, 2022, **426**, 128091.

321 L. Guo, S. Chen, Y. L. Yu and J. H. Wang, A Smartphone Optical Device for Point-of-Care Testing of Glucose and Cholesterol Using Ag NPs/UiO-66-NH_2-Based Ratiometric Fluorescent Probe, *Anal. Chem.*, 2021, **93**, 16240–16247.

322 Y. Shi, Q. Wu, W. Li, L. Lin, F. Qu, C. Shen, Y. Wei, P. Nie, Y. He and X. Feng, Ultra-sensitive detection of hydrogen peroxide and levofloxacin using a dual-functional fluorescent probe, *J. Hazard. Mater.*, 2022, **432**, 128605.

323 S. Chen, T. Li, D. Deng, Y. Ji and R. Li, Bifunctional Fe@PCN-222 nanozyme-based cascade reaction system: Application in ratiometric fluorescence and colorimetric dual-mode sensing of glucose, *Spectrochim. Acta, Part A*, 2022, **279**, 121427.

324 Y. Xia, K. Sun, Y.-N. Zuo, S. Zhu and X.-E. Zhao, Fluorescent MOF-based nanozymes for discrimination of phenylenediamine isomers and ratiometric sensing of o-phenylenediamine, *Chin. Chem. Lett.*, 2022, **33**, 2081–2085.

325 W. Jing, F. Kong, S. Tian, M. Yu, Y. Li, L. Fan and X. Li, Glucose oxidase decorated fluorescent metal-organic frameworks as biomimetic cascade nanozymes for glucose detection through the inner filter effect, *Analyst*, 2021, **146**, 4188–4194.

326 H. Sun, J. Zhang, M. Wang and X. Su, Ratiometric fluorometric and colorimetric dual-mode sensing of glucose based on gold-platinum bimetallic nanoclusters, *Microchem. J.*, 2022, **179**, 107574.

327 Y. Zhai, Y. Li, X. Huang, J. Hou, H. Li and S. Ai, Colorimetric and ratiometric fluorescent dual-mode sensitive detection of Hg^{2+} based on UiO-66-NH_2@Au composite, *Spectrochim. Acta, Part A*, 2022, **275**, 121187.

328 C. Zhang, P. Ni, B. Wang, W. Liu, Y. Jiang, C. Chen, J. Sun and Y. Lu, Enhanced oxidase-like activity of g-C_3N_4 nanosheets supported Pd nanosheets for ratiometric fluorescence detection of acetylcholinesterase activity and its inhibitor, *Chin. Chem. Lett.*, 2022, **33**, 757–761.

329 M. X. Liu, H. Zhang, X. W. Zhang, S. Chen, Y. L. Yu and J. H. Wang, Nanozyme Sensor Array Plus Solvent-Mediated Signal Amplification Strategy for Ultrasensitive

Ratiometric Fluorescence Detection of Exosomal Proteins and Cancer Identification, *Anal. Chem.*, 2021, **93**, 9002–9010.

330 D. Zhao, Y. Huang, H. Ouyang, B. Shi, S. Li, S. Chen and S. Zhao, Facile preparation of Cu-doped carbon dots for naked-eye discrimination of phenylenediamine isomers and highly sensitive ratiometric fluorescent detection of H_2O_2, *Talanta*, 2022, **239**, 123110.

331 W. Zhang, Y. Wu, X. Liu, Y. Liu, Y. Zhang, W. Wang, X. Mu, R. Su, Y. Sun, D. Song and X. Wang, A universal sensing platform based on iron and nitrogen co-doped carbon dots for detecting hydrogen peroxide and related metabolites in human fluid by ratiometric fluorometry and colorimetry, *Spectrochim. Acta, Part A*, 2022, **272**, 121003.

332 F. Li, J. Chen, J. Wen, Y. Peng, X. Tang and P. Qiu, Ratiometric fluorescence and colorimetric detection for uric acid using bifunctional carbon dots, *Sens. Actuators, B*, 2022, **369**, 132381.

333 L. Su, S. Qin, Y. Cai, L. Wang, W. Dong, G. Mao, S. Feng, Z. Xie and H. Zhang, Co, N-doped carbon dot nanozymes with acid pH-independence and substrate selectivity for biosensing and bioimaging, *Sens. Actuators, B*, 2022, **353**, 131150.

334 L. Hou, Y. Huang, T. Lin, F. Ye and S. Zhao, A FRET ratiometric fluorescence biosensor for the selective determination of pyrophosphate ion and pyrophosphatase activity based on difunctional Cu-MOF nanozyme, *Biosens. Bioelectron.: X*, 2022, **10**, 100101.

335 Y. Zhang, Y. S. Feng, X. H. Ren, X. W. He, W. Y. Li and Y. K. Zhang, Bimetallic molecularly imprinted nanozyme: Dual-mode detection platform, *Biosens. Bioelectron.*, 2022, **196**, 113718.

336 Q. Zuo, Y. Chen, Z. P. Chen and R. Q. Yu, A novel ratiometric fluorescent sensing method based on MnO_2 nanosheet for sensitive detection of alkaline phosphatase in serum, *Talanta*, 2020, **209**, 120528.

337 R. Wang, Z. Wang, H. Rao, X. Xue, M. Luo, Z. Xue and X. Lu, A two fluorescent signal indicator-based ratio fluorometric alkaline phosphatase assay based on one signal precursor, *Chem. Commun.*, 2021, **57**, 4444–4447.

338 F. Liu, Z. Li, G. Kang, Z. Liu, S. Zhu, R. He, C. Zhang, C. Chen and Y. Lu, Ratiometric sensing of α-glucosidase and its inhibitor based on MnO_2 nanosheets promoted *in situ* fluorescent reactions, *Microchem. J.*, 2023, **186**, 108352.

339 K. Wang, J. Liu, X. Wang, X. Liu, J. Hu, E. Li, Y. Zhao, R. Zhao and S. Yang, Ratiometric fluorescent detection system based on dual-driving catalysis of CuO nanozyme with a classical univariate calibration for the determination of ascorbic acid in serum and fruits, *Microchem. J.*, 2022, **172**, 106921.

340 F. Guo, M. Xia, J. Sun and S. Zhu, A ratiometric fluorescence assay for bleomycin based on Cu^{2+}-triggered cascade reactions and nanoparticle-mediated autocatalytic reactions, *New J. Chem.*, 2021, **45**, 13620–13625.

341 H. Lu, C. Yu and S. Xu, A dual reference ion-imprinted ratiometric fluorescence probe for simultaneous detection of silver(I) and lead(II), *Sens. Actuators, B*, 2019, **288**, 691–698.

342 R. Ying, H. Lu and S. Xu, Ion imprinted dual reference ratiometric fluorescence probe for respective and simultaneous detection of Fe^{3+} and Cu^{2+}, *New J. Chem.*, 2019, **43**, 6404–6410.

343 H. Lu and S. Xu, Dual channel ion imprinted fluorescent polymers for dual mode simultaneous chromium speciation analysis, *Analyst*, 2020, **145**, 2661–2668.